Single and Multi-Hop Vehicular Visible and Infrared Light Communications

Elizabeth Tinuke Eso

A thesis submitted in partial fulfilment of the requirements of the University of Northumbria at Newcastle for the degree of Doctor of Philosophy

Research undertaken at the Faculty of Engineering and Environment

July 2021

ABSTRACT

Visible light communications (VLC) have been proposed as a complementary technology in vehicular networks due to its several merits including high security, high scalability than RF technology. Notably, the RF technology established for vehicular networks best known as the dedicated short-range communications, supports many applications but doubts still exist on the capability of this technology to meet the low latency (where not more than 20 ms is required for pre-crash sensing and cooperative collision mitigation) and high reliability requirements in intelligent transport systems (ITS), when considering issues such as network outages as well as security issues. Of interest is the wide increase in the use of light emitting diode (LED)-based vehicle and traffic lights, and cameras in vehicles (rear and dashcams), traffic and security cameras, hence opening more opportunities for the VLC technology as part of ITS. Remarkably, camera-based VLC (i.e., optical camera communications) offers even further capabilities such as vehicle localization, motion and scene detection and pattern recognition.

However, the VLC system has few challenges that needs addressing for the practical implementation of this technology as part of ITS. Consequently, this thesis focuses on addressing the key challenges and proposing novel technical analytical and experimental solutions. Firstly, increasing the robustness to sunlight induced noise is one of the major challenges in vehicular VLC, hence this thesis proposes an infrared (IR) transmission, as the amount of solar irradiance is lesser in the IR band than in the visible band. Performance of the proposed scheme is validated through numerical simulations with realistic emulated sunlight noise from empirical measurement.

Investigations on the effects of turbulence with aperture averaging and fog on vehicular VLC is also carried out via experiments. Secondly, increasing the communication range is another major challenge, consequently the feasibility of using different vehicle taillights (TLs) as the VLC transmitter are evaluated via simulations based on empirical measurements of the radiation characteristics and transmit powers of the TLs. Results obtained indicate that, only a very low link span of < 10 m are achievable at data rates of 2-10 Mbps due to their low transmit power. Thus, the inclusion of IR-LEDs in headlights and TLs to provide the needed transmit power levels (within eye safety limits) required for longer transmission spans is proposed. Notably for the proposed IR-vehicular link, a link span of up to 63, 72, and > 89 m at the forward error correction (FEC) bit error rate (BER) limit of 3.8×10^{-3}, compared to 4.5, 5.4, and 6.3 m for the BMW vehicle-based TL at data rates of 10, 6, and 2 Mbps are achieved under realistic sunlight conditions. While, to increase the communication distance of camera-based VLC links, reducing the spatial bandwidth of the camera in its out of focus regions is proposed, mathematically analysed, and experimentally demonstrated where up to a 400 m link span at a 100 % success reception rate is achieved at a data rate of 800 bps, which is the longest so far reported.

Relay-assisted links are also investigated using amplify-and-forward (AF) and decode-and-forward (DF) relaying schemes under the emulated sunlight noise. A mathematical and simulation-based system model is developed, where different transmitter/receiver geometries are considered and AF and DF schemes. Results obtained via simulations shows that the DF scheme is a suitable candidate for vehicular VLC connectivity under emulated sunlight noise, offering at the FEC BER limit of 3.8×10^{-3} up to 150 % increase in the link distance by the end of the 2nd hop. Proof of concept experimental demonstration of AF and DF schemes for vehicular VLC are also carried out showing that DF is the preferred option. Moreover, insights are provided into the impact of various system parameters on the relay-assisted links. Finally, increasing the mobility of the vehicular VLC system is another major challenge, hence analysis on the required angular field of view (AFOV) for vehicular links considering necessary geometry parameters is investigated. Mathematical expressions to determine the required AFOV based on key system parameters are also derived. Furthermore, the relevance of the choice of the receiver parameters for an enhanced AFOV is also analysed, consequently a means to mitigate the effects of beam spot offset induced power losses at the photodiode caused by the misalignment of the transmitter and imaging receiver is proposed.

TABLE OF CONTENTS

LIST OF FIGURES

LIST OF TABLES

DEDICATION

To the Almighty God, the giver of life.

ACKNOWLEDGMENTS

I am thankful to the Almighty God for sustaining me through the rigours of this PhD research work.

My sincere appreciation goes to my principal supervisor Prof. Zabih Ghassemlooy for the excellent supervision, guidance and the invaluable time invested into my work, which all made this work possible. I am also very grateful to by co-supervisor, Prof. Stanislav Zvanovec for the wealth of knowledge shared with me and resources while at the Czech Technical University (CTU) in Prague for my secondment. I will also like to thank Dr. Juna Sathian my second co-supervisor for all the guidance during my PhD programme.

I am indeed very grateful to the European Union H2020, under the Marie Sklodowska Curie Actions for sponsoring my PhD programme through the **Vis**ible light-based **I**nter**o**perability and **N**etworking (VISION) project, which was a joint doctoral and innovative training programme.

My appreciation goes to past and present members of the optical communications research group and the Department of Mathematics, Physics and Electrical Engineering, Northumbria University namely, Dr Mojtaba M. Abadi, Dr Navid Bani Hassan, Dr. Andrew Burton and Dr. David Johnson for all their assistance and insightful discussions. I will also like to thank the team from CTU in Prague, namely Dr. Petr Pesek, Dr. Petr Chvojka and Shivani Teli for all their help, while I was at CTU for my secondment. I am also thankful to Dr. Luis Alves and his team for the support and guidance during my virtual secondment with the Instituto de Telecomunicações, Aveiro, Portugal.

I am indebted to my husband Mr Andrew Eso for all his efforts, love, support and care during this PhD programme and my son Samuel Eso for coping in very demanding times.

I want to greatly appreciate my parents; Prof J. P. Fabiyi and Late Dr. Mrs E.F Fabiyi (who departed to Glory few weeks ago). Your great impact on my educational journey will not be forgotten.

To my siblings, Dr. Mrs K. Akande for all your efforts and encouragement, Mrs F. Arowolo, Engr. O. Fabiyi and Mr S. Fabiyi, thank you all for being there. I will also like to thank my family friends namely, Dr. and Mrs Sam Ohiomokhare, Dr and Mrs T. Alaje, Mrs A. Chukwu-Etu, Pastor. M. and Mrs. M. Eje, Dr D. Ikah, Dr. Mrs Elnaz Alizadeh Jarchlo, and all the VISION project members for all their kind gestures and encouragement.

To all those who have contributed in one way or the other, whose names are not mentioned here, you are very much important. Thanks for all your immeasurable contributions and advice.

DECLARATION

I declare that the work contained in this thesis has not been submitted for any other award and that it is all my own work. I also confirm that this work fully acknowledges opinions, ideas and contributions from the work of others.

Any ethical clearance for the research presented in this thesis has been approved. Approval has been sought and granted by the Faculty Ethics Committee / University Ethics Committee / external committee.

I declare that the word count of this Thesis is 31,618.

Signature:

Name: Elizabeth Tinuke Eso

Date: 8th July 2021

ABBREVIATIONS

2D	Two-dimensional
5G	Fifth Generation
6G	Sixth Generation
AF	Amplify and forward
AFOV	Angular field of view
AWG	Arbitrary waveform generator
BER	Bit error rate
BSO	Beam spot offset
BSZ	Beam spot size
CoC	Cirle of confusion
CMOS	Complementary metal-oxide-semiconductor
DF	Decode and forward
DSO	Digital signal oscilloscope
DSRC	Dedicated short range Communications
DYRP	Dynamic routing protocol
FEC	Forward error correction
FOV	Field of view
fps	Frames per second
GG	Gamma-Gamma
GS	Global shutter
HLs	Headlights
HS-AFOVs	Horizontal semi- angular field of view
I2V	Infrastructure-to-vehicle
IoT	Internet of things
IoV	Internet of vehicles
IS	Image sensor
IR	Infrared
ITS	Intelligent transport systems

IM/DD	Intensity modulation direct detection
LED	Light emitting diode
LOS	Line of sight
MF	Matched filter
MI	Modulation index
MIMO	Multiple-input multiple-output
MSE	Pixel luminance mean squared error
NIOC	Non-imaging optical concentrator
NLOS	Non line of sight
NRZ	Non return to zero
OCC	Optical camera communications
OC	Optical concentrator
OF	Optical filter
OIoT	Optical internet of things
OOK	On off keying
OWC	Optical Wireless Technology
PD	Photodiode
PDF	Probability density function
PSNR	Peak signal to noise ratio
QoS	Quality of service
RF	Radio frequency
RGB	Red, green, and blue
RS	Rolling shutter
Rx	Receiver
SNR	Signal to noise ratio
TLs	Taillights
Tx	Transmitter
V2D	Vehicle-to-device
V2I	Vehicle-to-infrastructure
V2R	Vehicle-to-road
V2V	Vehicle-to-vehicle

V2X	Vehicle-to-everything
VLC	Visible light communications
VANETs	Vehicular ad hoc networks
VL-ROUTE	Cross layer optimized routing protocol
VS-AFOV	Vertical semi-angular field of view

GLOSSARY OF SYMBOLS

A_{coll}	Collection area of the non-imaging OC
A_{fg}	Fog attenuation
A_{img}	Area of the projected focused image of the light source
A_{PD}	Active area of the PD
A_{TL}	Surface area of the light source
B	Bandwidth
$b_{\text{hor}-\text{of}}$	Horizontal beam spot offset
b_{of}	Beam spot offset
$b_{\text{ver}-\text{of}}$	Vertical beam spot offset
C_{PD}	Equivalent capacitance
C_T^2	Temperature structure parameter
C_n^2	Refractive index structure parameter
d_{BSZ}	Beam spot size
$D_T(L_T)$	Structure function of temperature
d_c	Distance between the centre of the lens and the image
d_{IS}	Distance between the centre of the lens to the image sensor
d_L	Distance from the light source to the centre of the lens
d_{Tx}	Diagonal widths
D_{CoC}	Diameter of the circle of confusion
D_{lens}	Lens aperture diameter
f	Focal length
f_{stop}	Focal stop number of the lens aperture
f_{Tx}	Switching frequency
$fI_\alpha(I_\alpha)$	PDF of Malaga distribution
g	Gains of optical concentrator

$G_{\mathrm{i}}(x,y)$	Focused image intensity function
$G_{\mathrm{o}}(x,y)$	Defocused image intensity function
G_{PD}	Gain of the PD
H_{fg}	Channel coefficient for fog
H_{LOS}	Channel DC gain
$h(t)$	Channel impulse response
h_{PD}	Height of PD
H_{RX}	Vertical height of receiver
H_{TX}	Vertical height of transmitter
I	Intensity of the optical beam
I_{dk}	Dark current
I_{mx}	Maximum possible pixel value
I_{Rx}	Average pixel value for the received symbols
I_{solar}	Photocurrent generated at the PD due to solar irradiance
I_{Tx}	Pixel values of the transmitted symbols
j	Pixel's row index number
k_b	Boltzmann's constant
k	Wave number
$K_{\alpha-\beta}(.)$	Modified Bessel function of the 2nd kind of order
L_1	Horizontal distance from the Tx1 and Tx2
L_2	Beam length of a single Tx
L_{FOV}	Coverage length of Tx1 and Tx2 beyond L_1
l_o	Inner scale of the small temperature fluctuation
L_o	Outer scale of the small temperature fluctuation
$L_{\mathrm{s-hor}}$	Horizontal link span between the Tx and the Rx
L_{sm}	Link safety margin
L_T	Separation span between two points with temperatures of T_1 and T_2
L_s	Link span
l_{Tx}	Length of the Tx
m	Lambertian order of emission of the Tx

N_{rows}	Number of data rows
$n(t)$	Additive white Gaussian noise
P	Pressure in millibar
$p(I)$	PDF of the GG distribution
P_r	Average received optical power
$P_{\text{r\_fog}}$	Average received optical power under fog
$P_{\text{solar}}(\lambda)$	Solar irradiance
P_T	Transmit power
q	Distribution size of scattering particles
$Q(x)$	Q-function used for the computation of the tail probability of the standard Gaussian distribution
$\mathcal{R}$	Responsivity of the PD
$R(\phi)$	Lambertian radiant intensity
R_L	Load resistance
R_b	Data rate
$R_{\text{Tx}}(\theta_{\text{hor}},\theta_{\text{ver}})$	Normalized beam profile of the Tx at vertical and horizontal irradiance angles θ_{ver} and θ_{hor}
$s(t)$	Data stream
T	Temperature in Kelvin
T_{exp}	Exposure time
$T_{\text{filt}}(\varphi)$	Transmittance of the OF
T_{fr}	Frame duration
T_{lens}	Transmittance of the OC
T_K	Absolute temperature in Kelvin
T_r	Read out time
T_f	Transmittance of the optical band pass filter
T_{rest}	Reset time
T_s	Gains of the optical filter
V	Meteorological visibility
$V_R(t)$	Voltage at a pixel
w_{PD}	Width of the PD

w_{RL}	Width of the road lane
w_{Rx}	Distance between Rx1 and Rx2
w_{Tx}	Distance between Tx1 and Tx2
$w_{\mathrm{v-Rx}}$	Width of Rx vehicle
$w_{\mathrm{v-Tx}}$	Width of the Tx vehicle
x	Deviation outside the lane edge
x_{Rx}	Distance of receiving vehicle from the lane edge
x_{Tx}	Distance of transmitting vehicle from the lane edge
$y(t)$	Line of sight received signal
$x(t)$	Transmit signal
$U(.)$	Heaviside step function
ΔH	Offset between the receiver's and transmitter's vertical heights
$\sigma^2_{\mathrm{shot-rs}}$	Signal dependent shot noise
$\langle . \rangle$	Ensemble average
$\emptyset_{\mathrm{diag}}$	Diagonal semi-AFOV of the Rx
$\emptyset_{\mathrm{hor}}$	Horizontal AFOV
$\emptyset_{\mathrm{S-AFOV}}$	Semi-AFOV
$\emptyset_{\mathrm{ver}}$	Vertical AFOV
α'	Effective number of large-scale cells of the scattering process
β'	Natural number representing the amount of turbulence
$\theta_{1/2}$	Half power angle
$\theta_{1/2-\mathrm{in}}$	Inner half power angle of the transmitter
$\theta_{1/2-\mathrm{out}}$	Outer half power angle of the transmitter
λ	Wavelength
σ^2_{amb}	Sunlight -induced shot noise variance
σ^2_{dk}	PD's dark current noise variance
$\sigma^2_{\mathrm{shot-rs}}$	Signal-dependent shot noise variance
$\sigma^2_{\mathrm{thermal}}$	Thermal noise variance
σ_I^2	The scintillation index

$\sigma_I^2(0)$	Scintillation index without the use of an optical concentrator at the receiver
$\sigma_I^2(D)$	Variance of the intensity fluctuation with an optical concentrator of diameter *D* at the receiver
$\sigma_R^2,$	Rytov variance
σ_T^2	Total noise variance
φ_{hor}	Horizontal incidence angles
φ_{sun}	Difference between the orientation angle between that of the photodiode and the measured $P_{\text{solar}}(\lambda)$
φ_{ver}	Vertical incidence angle
φ_A, φ_B	Line of sight phases
$2b_0$	Average power of the total scatter components
α	Effective number of large-scale eddies of the scattering process
β	Effective number of small-scale eddies of the scattering process
Ω	Average power of the line-of-sight component
$\Gamma(.)$	Gamma function
θ	Irradiance angle
$\otimes\otimes$	2-dimensional convolution operator
ρ	Amount of scattering power that is coupled to the LOS component
φ	Incidence angle

CHAPTER 1

INTRODUCTION

1.1 Background

The core driving force of the fifth generation (5G) and the emerging sixth generation (6G) and beyond wireless networks is the enlarging multi-media services, aided through an extensive increase in the number of Internet of things (IoT) devices. Interestingly, these IoT devices will realize sophisticated services such as environmental monitoring, smart traffic, including autonomous driving, digital sensing, virtual reality, surveillance, home monitoring and automation, full high-definition video transmission in connected robots and drones [1-2]. It is predicted that IoT devices will reach 75 billion by the year 2025 [3], hence the importance of the establishment of 5G/6G on multiple technologies to ensure a high quality of service [4-5]. The optical wireless communications (OWC) technology is envisioned to be part of 5G/6G and beyond wireless networks for deployment in applications areas where radio frequency (RF)-based technologies cannot be used or are limited due to security issues, insufficient bandwidth and electromagnetic interference. In [6], several novel concepts have been identified on the use of OWC in 6G, including hybrid radio-optical wireless networks, where wireless devices or nodes are equipped with both optical and RF interfaces. Notably, the distinctive features of OWC that makes it an attractive technology for 5G/6G include high security, large unlicensed spectrum, high safety, low cost, simplicity in implementation, interference free network achievable under a dense network, lower power consumption and non-susceptibility to RF-induced interference. Thus, the

coexistence of the RF and OWC technologies can effectively solve the major challenges of the individual RF and OWC links [7].

The wireless exchange of traffic information between vehicles and roadside infrastructure, which is part of the emerging intelligent transport systems (ITS), can considerably improve the efficiency and road safety of transportation networks [8-11]. Notably, ITS involves the provision of safe driving information, which includes warning messages on the driving speed limits, road terrains, pedestrian crossing the road, etc. Thus, the provision of safe traffic information and alerts to the drivers will give additional capabilities for improving traffics on the roads and the quality of life. Presently, RF-based wireless communications technology is the established option in ITS [12-13], which is best known as the dedicated short-range communications (DSRC). DSRC supports many applications for instance, intersection collision and emergency braking warnings [12]. Nevertheless, some doubts remain about DSRC's ability to meet the low latency and high reliability requirements in ITS (see Table 1.1 showing maximum required latencies), putting into consideration issues relating to network outages as well as security [14-17]. Note that, past research has shown that communications in the vehicular environment using the RF technology often experience low packet reception rate and long delays on dense roads (where the number of vehicles is high) [17]. For example, in [18] for the IEEE 802.11 medium access control layer for DSRC broadcast, the packet reception rate decreased from 1 to 0.38 and the delay increased from 20 to 335 ms as the vehicle density doubled to 200 vehicles/km. The system parameters for the latter were a data rate of 24 Mbps, bit-error-rate (BER) of 10^{-4}, packet rate of 10 per second and 10 packet repetitions. Also, for the RF-based vehicular communications within tunnels, there is the challenge of a high link degradation [19] where the data rate can deteriorate up to 52.4 % [20]. Notably, energy

efficiency is regarded as one of the most significant performance metrics for beyond 5G wireless communications to support enormous mobile data traffic from massive IoT devices and thus the green techniques are highly desirable; hence there has been several works in this direction [21-27] to reduce the overall power consumption of wireless communication system. As a result of these challenges, visible light communications (VLC), which is a green technology, and part of the OWC technology, using luminance as a medium for data transmission via light emitting diodes (LEDs), laser diodes and liquid crystal displays naturally emerges as an interesting and promising complementary technology option in 5G and beyond wireless networks and specifically in vehicular communications [28-32], which is the focus here.

Table 1.1: High priority safety applications [33]

Application	Max. Range [m]	Rate [/s]	Max. Latency [ms]	Message Length [bits]	Type
Traffic Signal Violation Warning	250	10	100	528	I2V
Curve Speed Warning	200	1	1000	235	I2V
Emergency Electronic Brake Light	300	10	100	288	V2V
Pre-Crash Sensing for Cooperative Collision Mitigation	50	-	20	435	V2V
Cooperative Forward Collision Warning	150	10	100	419	V2V
Left Turn Assistant	300	10	100	904 208	I2V and V2I
Lane Change Warning	150	10	100	288	V2V
Stop Sign Movement Assistant	300	10	100	208 416	V2V and I2V

Of interest is also the widespread increase in the use of LED and laser-based light sources in traffic infrastructures, roadside lamp posts, vehicle headlights (HLs) and taillights (TLs) [34-36], which offers lower dissipation of heat, longer life spans, brighter

illumination and switching capabilities higher than halogen bulbs adopted in the past [37-38], thus making the realisation of VLC possible and an attractive option in ITS. It is worthy of note that, the OWC technology employing LEDs produces a smaller collision domain [14-15], and consequently results in decreased packet losses due to interference, compared with the RF wireless system. Also, in cases of high vehicle density, VLC provides improved scalability than RF, whereby RF suffers from long packet delays due to channel congestion [39-40]. Fundamentally, the directionality of OWC is an advantage in vehicular VLC as it increases the security of the communication networks, reduces the possibility of eavesdropping significantly, and naturally filtering out surrounding nodes that are outside the field of view of the Rx or that are distant without the need of any protocol considerations [17]. Importantly, VLC can be used in a vehicular network environment for vehicle-to-vehicle (V2V), vehicle-to-infrastructure (V2I), vehicle-to-device (V2D) and vehicle to road (V2R) communications, which are generally referred to as vehicle-to-everything (V2X) communications and further discussed in Chapter 2. Notably, vehicular VLC systems make use of vehicle and road light infrastructures as the optical transmitters (Txs) with a driver. The intensity modulated light beam from the vehicle/road light infrastructure propagate through the free space and is captured at the receiver (Rx) side using a photodiode (PD) or an image sensor (camera). Note, field programmable gate arrays can be used as modulation and demodulation drivers for the Tx and Rx, respectively. Interestingly, the vehicular VLC systems with the camera-based Rx provides further capabilities to the communication networks, such as the reception of information from multiple Txs at the same time [41], cooperative vehicle positioning alongside communications [41], motion and scene detection [42-43], range estimation [43], object and people detection [44], pattern recognition [45], etc. It is noteworthy that, the

vehicular VLC technology also has some challenges that needs investigating as highlighted in the next subsection and are discussed in detail in Chapter 2.

1.2 Problem Statements

1.2.1 Ambient light and weather effects on the vehicular VLC communication systems

Indoor VLC applications have been intensely investigated over the last decade [39,46,47]. However, outdoor applications bring added challenges and therefore need further investigations [48-51]. In this emerging field of vehicular communications, determining the performance boundaries forced by the model and size of vehicles, infrastructure facilities, and the real outdoor conditions such as sunlight, fog, atmospheric turbulence, and snow/rain, which have a significant impact on the performance of the link, is of paramount importance to the practical implementation of this technology as part of ITS.

Sunlight-induced noise is a major issue in vehicular VLC systems during the day, when the illumination levels can reach 10 mW/cm^2 compared to $\mu W/cm^2$ for intensity-modulated HL and TL [50,52]. This high-level of ambient light can lead to saturation of the optical Rx. It is worth noting that most of the studies on vehicular VLC have not considered the impact of sunlight noise. Also, the presence of fog, depending on the density can cause significant optical distortions. In [53] up to 60% reduction in the achievable link span at a meteorological visibility of 10 m and target BER of 10^{-6} was reported. Moreover, the atmospheric turbulence, which causes random fluctuations in both the phase and amplitude of the propagating optical beam, can lead to fading and consequently reduced signal-to-noise ratio (SNR) [54-56]. Hence, channel modelling for

vehicular VLC is very crucial. Notably, little has been reported in the literature on the impact of atmospheric weather conditions on the performance of vehicular VLC systems.

1.2.2 Communication range

The use of relay nodes have been suggested and studied in [57-60] to expand the communications range in OWC. The VLC technology has previously been applied to indoor communications with relatively short link spans of few metres and needs to be extended to satisfy vehicular communications with relatively longer link spans in the range of tens of metres to few hundreds, depending on the driving speed and weather conditions [61]. The relay-based systems have been demonstrated to be a viable tool for reducing channel fading over short transmission ranges in [57]. However, very little have also been reported on relay-assisted vehicular VLC systems. Notably, there is also the need to investigate the rolling shutter (RS)-based optical camera communications (OCC) links, which offer flicker-free transmissions and data rates higher than the camera's frame rate (required for vehicular networks) but at the cost of reduced coverage distance.

1.3 Aims and Objectives

The aim of this research is to carry out comprehensive mathematical analysis, model development and experimental investigations with respect to the system design and performance evaluation of vehicular VLC. The desired system should be adequate to mitigate the channel conditions and system limitations, consequently providing improved system performance.

Therefore, the main objectives are as follows:

1. To conduct in-depth literature review on the vehicular VLC system.

2. To carry out detailed mathematical analysis of vehicular VLC and evaluate its performance considering the sunlight induced noise. Furthermore, to develop a novel method to mitigate the effects of this induced sunlight noise.
3. To develop a simulation model of the vehicular VLC system to investigate different vehicular VLC deployment scenarios.
4. To develop novel schemes to enable transmission over longer distances for vehicular VLC/OCC.
5. To investigate the performance of the vehicular VLC system under weather conditions (i.e., turbulence and fog)
6. To investigate amplify and forward (AF) and decode and forward (DF) relaying schemes in a vehicular VLC system.

1.4 Thesis Contributions

The original contributions of this research are outlined as follows:

1. In Chapter 3, fundamental analysis of vehicular VLC is carried out, including optical characterisation and performance evaluation of different vehicle TLs as Txs for vehicular VLC systems. Insights into the (*i*) required Rx's angular field of view (AFOV) considering the key parameters such as the road lane and vehicle widths, as well as the positions of the Tx and the Rx etc.; and (*ii*) Tx's coverage field of view, and demonstration of the AFOV of the Rx-based on varying optical detector sizes with varying focal lengths of lenses are provided. Based on the results of the performance evaluation of the TLs, a novel robust infrared (IR)-based light communications system considering practical and realistic parameters is proposed to mitigate the sunlight induced noise and also increase

the communication distance, which are major issues in vehicular VLC. Finally, performance analysis of the proposed system under realistic sunlight induced noise from empirical measurements is carried out (see research output J5).

2. In Chapter 4, a new technique to increase the link span of a RS-based OCC system is proposed. Using the proposed scheme, a long-distance OCC link of up to a 400 m link span at a data rate of 800 bps is demonstrated experimentally and the developed image processing and detection method to extract the information out of the received image frames is also presented (see research output J1).

3. In Chapter 5, the performance of vehicular VLC under atmospheric turbulence and fog is investigated by means of experiments. Experimental investigations of the vehicular VLC link using a non-collimated and an incoherent light source (i.e., a LED) as the Tx and two different optical Rx types, i.e., a camera and a PD, under turbulence with aperture averaging to mitigate the effects of turbulence are carried out. Also, the effects of fog on camera-based vehicular links are experimentally investigated (see research outputs C4, C5, and J4).

4. In Chapter 6, performance analysis of relay-assisted vehicular VLC system with AF and DF schemes under realistic sunlight induced noise is investigated. For the first time, the effect of beam spot offsets (BSO) (the offset of the projected image of the light source from the lens) at the PD due to the misalignment of the Tx and the Rx are investigated. A novel method to mitigate the effects of BSO induced signal losses is also proposed (see C6 and J6).

The summary of the contributions of this thesis is graphically illustrated in Figure 1.1 where the coloured blocks show the research works carried out (with brief descriptions below) and their respective Chapter locations.

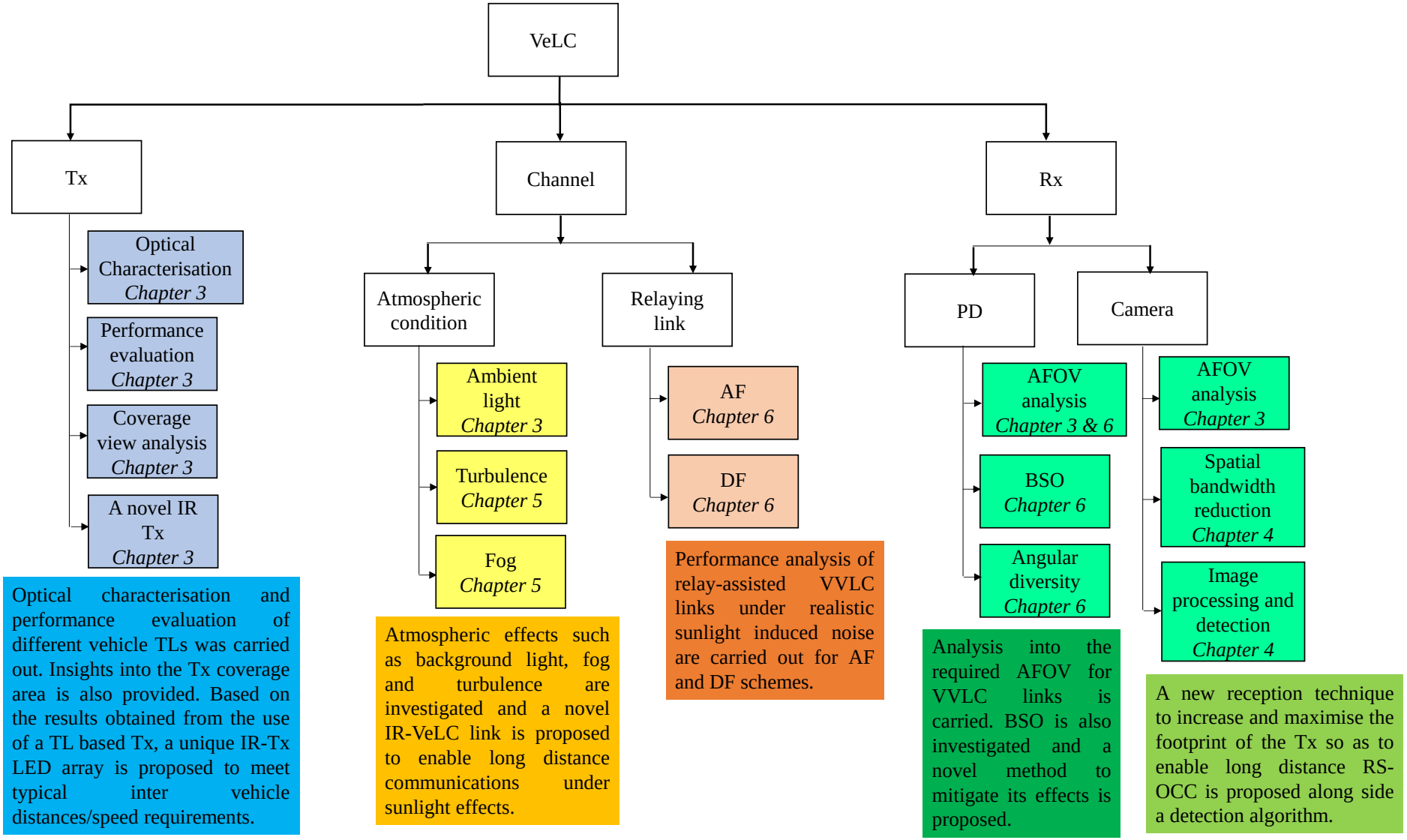

Figure 1.1: Summary of original contributions

1.5 Thesis Structure

This thesis is organized into seven chapters. Chapter 1 introduces vehicular VLC, its merits and challenges. The aims, objectives and the original contributions of this research are also presented. Chapter 2 presents a detailed review of key aspects of vehicular VLC in terms of the current challenges in this system, such as increasing the robustness to noise under sunlight noise, fog, and atmospheric turbulence. Other challenges discussed also include increasing the communication range to meet up with typical inter vehicle distances and increasing the mobility of the system. This chapter also outlines possible solutions that have been proposed from past research works. Chapter 3 presents the fundamental analysis of vehicular VLC, including optical characterization of different vehicle TLs from popular brands. Insights are also provided into the required AFOV for IR/VLC considering key parameters such as the lane widths, the positioning of the Tx and Rx on vehicles, the size of the Tx and the vehicle widths, etc. Moreover, mathematical expressions to calculate the required AFOV and coverage field of view of vehicle lights are derived. Furthermore, solar irradiance measurements to obtain realistic values of sunlight induced noise is carried out, which is the major noise source for vehicular VLC systems during daytime and needs to be modelled accurately. Also, other noises impairing the vehicular IR/VLC system are outlined and taken into consideration in the performance analysis of vehicular IR/VLC systems carried out. The characterised TLs all fell short of typical communication distances in vehicular environments, consequently a novel vehicular IR light link is proposed to allow for long distance communications at high data rates. It was shown that, the proposed IR light system outperforms the visible light-based TLs, particularly in the presence of sunlight. Chapter 4 presents the proposed a new technique for extending the communication distance and

data rates of an OCC system. A 400 m experimental link is demonstrated with 100 % success rate in the reception of the transmitted signal. In Chapter 5, investigations on turbulence and fog effects are presented. Mitigation of the effects of turbulence with the aperture averaging method is experimentally demonstrated for both the camera and PD based Rxs for vehicular VLC systems. In Chapter 6, relay assisted vehicular VLC links is investigated with AF and DF schemes under realistic sunlight noise. Results for different Tx-Rx orientations and system parameters are presented, where importantly, real road driving conditions are modelled, taking into consideration misalignment between the transmitting and receiving vehicles and their impact on the performance of the vehicular VLC is evaluated. A method to mitigate the degrading effect of misalignment conditions on vehicular VLC systems is also proposed. Finally, in Chapter 7, conclusions are given and recommendations for future work.

1.6 Publications

1.6.1 Journals

[J1] **E. Eso**, S. Teli, N. B. Hassan, S. Vitek, Z. Ghassemlooy, and S. Zvanovec '400 m Rolling Shutter based Optical Camera Communications Link,' *Optics Letters*, vol. 45, no. 5, pp. 1059-1062, 2020, doi.org/10.1364/OL.385423.

[J2] V. Matus, **E. Eso**, S.R. Teli, R. Perez-Jimenez and S. Zvanovec 'Experimentally Derived Feasibility of Optical Camera Communications under Turbulence and Fog Conditions' *Sensors*, vol. 20, no. 3, p. 757, Jan. 2020, doi.org/10.3390/s20030757.

[J3] H. B. Eldeeb, **E. Eso**, E.A. Jarchlo, M. Uysal, Z. Ghassemlooy, S. Zvanovec and J. Sathian 'Vehicular VLC – A Ray Tracing Study Based on

Measured Radiation Patterns of Commercial Taillights' *IEEE Photonics Letters*, vol. 33, no. 16, pp. 904-907, Aug. 2021, doi: 10.1109/LPT.2021.3065233.

[J4] **E. Eso**, Z. Ghassemlooy, S. Zvanovec, J. Sathian, M. Mansour Abadi and O.I. Younus. Performance of Vehicular Visible Light Communications under the Effects of Atmospheric Turbulence with Aperture Averaging. *Sensors*, vol. 21, no. 8, p. 2751, Apr. 2021, doi.org/10.3390/s21082751.

[J5] **E. Eso**, Z. Ghassemlooy, S. Zvanovec, J. Sathian, and A. Gholami 'Fundamental Analysis of Vehicular Light Communications and the Mitigation of Sunlight Noise' *IEEE transactions on Vehicular Technology*, vol. 70, no. 6, pp. 5932-5943, June 2021, doi: 10.1109/TVT.2021.3078576.

[J6] **E. Eso**, Z. Ghassemlooy, S. Zvanovec, P. Pesek and J. Sathian, "Vehicle-to-Vehicle Relay-Assisted VLC with Misalignment Induced Azimuth or Elevation Offset Angles," IEEE Photonics Technology Letters, vol. 33, no. 16, pp. 908-911, Aug. 2021, doi: 10.1109/LPT.2021.3086836.

[J7] E. A. Jarchlo, **E. Eso**, H. Doroud, A. Zubow, F. Dressler, Z. Ghassemlooy, B. Siessegger, G. Caire 'FDLA: A Novel Frequency Diversity and Link Aggregation Solution for Handover in an Indoor Vehicular VLC Network' *IEEE transactions on Network and Service Management*, vol. 18, no. 3, pp. 3556-3566, Sept. 2021, doi: 10.1109/TNSM.2021.3075476.

[J8] E. A. Jarchlo, **E. Eso**, H. Doroud, B. Siessegger, Z. Ghassemlooy, G. Caire and F. Dressler 'Li-Wi: An Upper Layer Hybrid VLC-Wifi Network Handover Solution. *Elsevier Ad Hoc Networks*, Oct. 2021, early access copy

available:

https://www.sciencedirect.com/science/article/pii/S157087052100202X

1.6.2 Conferences

[C1] **E. Eso**, Z. Ghassemlooy, S. Zvanovec, A. Gholami, A. Burton, N. B. Hassan, and O. I. Younus. Experimental demonstration of vehicle to roadside infrastructure visible light communications. *IEEE West Asian Conference on Optical Wireless Communication*, Tehran, Iran, 2019, pp. 85-89, doi: 10.1109/WACOWC.2019.8770186.

[C2] E. A. Jarchlo, S. M. Kouhini, H. Doroud, **E. Eso**, P. Gawłowicz, M. Zhang, B. Siessegger, M. Jung, Z. Ghassemlooy, G. Caire and A. Zubow, "Analyzing interface bonding schemes for VLC with mobility and shadowing," *12th IEEE/IET International Symposium on Communication Systems, Networks and Digital Signal Processing (CSNDSP)*, 2020, pp. 1-5, doi: 10.1109/CSNDSP49049.2020.9249515.

[C3] M. R. Soares, N. Chaudhary, **E. Eso**, O. I. Younus, L. Nero Alves and Z. Ghassemlooy, "Optical camera communications with convolutional neural network for vehicle-to vehicle links," *12th International Symposium on Communication Systems, Networks and Digital Signal Processing (CSNDSP)*, 2020, pp. 1-6, doi: 10.1109/CSNDSP49049.2020.9249499.

[C4] **E. Eso**, O. I. Younus, Z. Ghassemlooy, S. Zvanovec and M. Mansour Abadi 'Performances of optical camera-based vehicular communications under turbulence conditions' *12th IEEE/IET International Symposium on Communication Systems, Networks, and Digital Signal Processing*, 2020, pp. 1-5, doi: 10.1109/CSNDSP49049.2020.9249598.

[C5] **E. Eso**, A. Burton, N. B. Hassan, M. Mansour Abadi, Z. Ghassemlooy, and S. Zvanovec 'Experimental investigation of the effects of fog on optical camera-based VLC for a vehicular environment. *15th International Conference on Telecommunications, Graz, Austria*, (*ConTEL*), 2019, pp. 1-5, doi: 10.1109/ConTEL.2019.8848552.

[C6] **E. Eso**, P. Pesek, P. Chvokja, Z. Ghassemlooy, S. Zvanovec, and J. Sathian. 'A relay-assisted vehicular visible light communications network'. *IEEE Photonics Conference (IPC)*, 2020, pp. 1-2, doi: 10.1109/IPC47351.2020.9252388

[C7] R. Yin; Z. Ghassemlooy; N. Zhao; H. Yuan; M. Raza; **E. Eso**; S. Zvanovec "A Multi-hop relay based routing algorithm for vehicular visible light communication networks," *12th International Symposium on Communication Systems, Networks and Digital Signal Processing (CSNDSP)*, 2020, pp. 1-6, doi: 10.1109/CSNDSP49049.2020.9249630.

[C8] H. B. Eldeeb, **E. Eso**, M. Uysal, Z. Ghassemlooy, S. Zvanovec and J. Sathian 'Vehicular visible light communications - ray-tracing and experimental validation', *IEEE Photonics Conference (IPC)*, 2020, pp. 1-2, doi: 10.1109/IPC47351.2020.9252554.

[C9] K. Lega; S. N. H Sammeta; D. Bollepally; G. K. Mallavarapu; **E. Eso**; Z. Ghassemlooy; S. Zvanovec "A real-time vehicular visible light communications for smart transportation,"*12th International Symposium on Communication Systems, Networks and Digital Signal Processing (CSNDSP)*, 2020, pp. 1-5, doi: 10.1109/CSNDSP49049.2020.9249443.

[C10] N. Devulapalli, V. Matus, **E. Eso**, Z. Ghassemlooy and R. Perez-Jimenez, "Lane-cross detection using optical camera-based road-to-vehicle communications," *17th International Symposium on Wireless Communication Systems (ISWCS)*, Sept. 2021, pp. 1-5, doi: 10.1109/ISWCS49558.2021.9562196.

[C11] **E Eso**, E.A. Jarchlo, Z. Ghassemlooy, S. Zvanovec, F. Dressler and J. Sathian "Performance analysis of indoor vehicular VLC links for autonomous driving," *IEEE International Symposium on Personal, Indoor and Mobile Radio Communications (PIMRC)*, Sept. 2021, pp. 1-5.

CHAPTER 2
OVERVIEW OF VEHICULAR VLC

2.1 Introduction

This chapter follows on the discussion in Chapter 1 on the challenges of DSRC (also referred to as the wireless access in vehicular environment (WAVE)) despite its several advantages and VLC proposed as a complementary technology for vehicular communications. Notably, VLC has been proposed to address the limitations of DSRC owing to its several advantages which were also outlined in the previous chapter. Importantly, this chapter discusses the current challenges of the VLC technology and the possible solutions proposed in past research works. Consequently, research gaps are identified, and the work carried out are highlighted in the context of the major challenges facing VLC for vehicular communications. The use cases of DSRC for ITS are also outlined.

2.2 Vehicular Communications

Accidents due to vehicles have been reported as one of the leading causes of death globally with up to an annual mortality rate of 1.35 million [62]. However, the wireless exchange of traffic information between vehicles, the road side infrastructure, etc., (i.e., ITS) can significantly improve road safety and the efficiency of transportation networks.

Use cases have been specified in the standards for DSRC for ITS, which are as follows [63]:

- **Traffic signal control management:** This involves the collection of traffic information by road-side units such as along traffic junction routes, for management of traffic for applications like adaptive phasing of traffic lights at junctions. Also, road-side units can give priority to emergency vehicles such as fire engines and ambulances, etc.
- **Traffic information applications:** This involves the dissemination of traffic information such as warning messages (of road obstructions, conditions, etc.), parking availability, road curve speed and stop light assistance.
- **Safety applications:** This involves services such as intersection collision warning avoidance, cooperative adaptive cruise control, cooperative vehicle system-platooning and cooperative collision warning.
- **Emergency applications:** Captured live videos from DSRC devices can be sent to control centres as supporting evidence when required.
- **Kiosk related services:** Diagnostic data such as firmware/software updates, automotive repair records can be made available through a service kiosk. Other services such as fuel payments, etc. may also be enabled through a kiosk service.
- **Localisation:** Location information can be provided by one or multiple road-side units to vehicles.
- **Electronic packing management:** This can be used for parking payment transactions and also vehicle access controls for private premises, etc.
- **Other ITS application and service:** Vehicle drivers can be alerted by pedestrians and cyclist to slow down/drive with caution at pedestrian/cyclist road crossings.

As discussed in Chapter 1, despite the several promising and potential applications of DSRC, some doubts remain about its ability to meet the low latency and high reliability requirements in ITS. DSRC is the established RF technology option for vehicular communications, which uses the 5.9 GHz spectral region [50] with channels of 10 MHz bandwidth as specified by the IEEE 802.11p standard for wireless access in vehicular environments [64] to enable communication spans up to 1000 m. Consequently, long distance communications with RF technology will also involve long distance interferences, as vehicles create interferences on areas outside the target communication area [50], which can lead to low packet reception rates on dense roads [17]. Consequently, this brings concerns regarding reliability [65-70] since low latency and high link reliability are the key aspects in vehicular communications to provide drivers the needed time to react to the received information. This is especially important for safety applications, such as cooperative collision warning and road terrain information, which are time critical.

Notably, the inter-vehicle distance is very important as shorter link spans between vehicles are more safety critical than link spans up to 1000 m, where the possibility of accidents is low. A two-second inter-vehicle distance rule is generally used to determine the inter-vehicle distance required, which specifies that in perfect, average and bad weather conditions, vehicles should be 2, 3, and 4 seconds apart [61], respectively. Consequently, applying this rule in [61] to a driving speed of 20 (minimum) and 80 mph (maximum) in perfect weather and bad weather conditions (worst case scenario), the inter-vehicle distance will range from 18 to 143 m. Note that, considering the latter, VLC links have been experimentally demonstrated within this range; for PD based links up to 50 m at a data rate of 11.67 kb/s [71], while camera-based links have higher link spans of up to 160 m [72] although at much lower data rate (50 b/s, although can be

significantly enhanced using the multiple input multiple output and artificial neural network schemes as highlighted in Chapter 4). Notably, VLC has been proposed for vehicular networks for V2V, V2I, V2D, V2R communications, which are commonly referred to as V2X communications and depicted in Figure 2.1. It is worth noting that, vehicles can achieve V2V communications with vehicles in their vicinity. Also, V2I communications can be realised with LED-based road infrastructure units such as road-side signage, traffic lights and streetlights, while V2R communications can be established with vehicles and road stud lights fitted on road lanes. Another subset of V2X is V2D, which allows the exchange of information between vehicles and smart devices such as mobile phones and tablets [73]. Also, there are different applications/possible use cases for V2X communications, which are as follows [73]:

- **Cooperative Awareness**: This includes applications such as emergency warning or forward collision warning, requiring communication with the direct neighbours, hence VLC can be used to exchange the messages between vehicles.
- **Cooperative Sensing/Perception**: VLC can be used for cooperative sensing applications, which includes sharing of the sensory data or collective collection of sensor data to perceive a bigger picture of the driving situation.
- **Emergency Brake Lights**: This notifies the drivers in case of sudden brakes by the vehicles ahead.
- **Intersection Assistance**: This involves cases like intersection collision avoidance, which is used to improve the safety in intersections by providing the means of coordination and warning between vehicles.

- **Information Query**: This involves query and dissemination of information. In addition to V2V communications, LED/laser-based traffic signs, traffic lights and road lightings can be used to disseminate information.
- **Platooning**: A major application for VLC in vehicular networks is platooning, which has been successfully demonstrated recently by a Japanese mobile communications infrastructure provider [74]. Usually in platooning, members are required to exchange information within regular intervals. Communication between vehicles can be established via VLC, while DSRC can be used for a broadcast message from the leader vehicle to the other vehicles in the platoon. This offers significantly reduced load on the RF channel and improved overall performance.

As highlighted in Chapter 1, despite the several merits of the VLC technology for vehicular communications, some challenges also exist, hence in the subsequent sections the major challenges in the usage of VLC in vehicular applications are discussed.

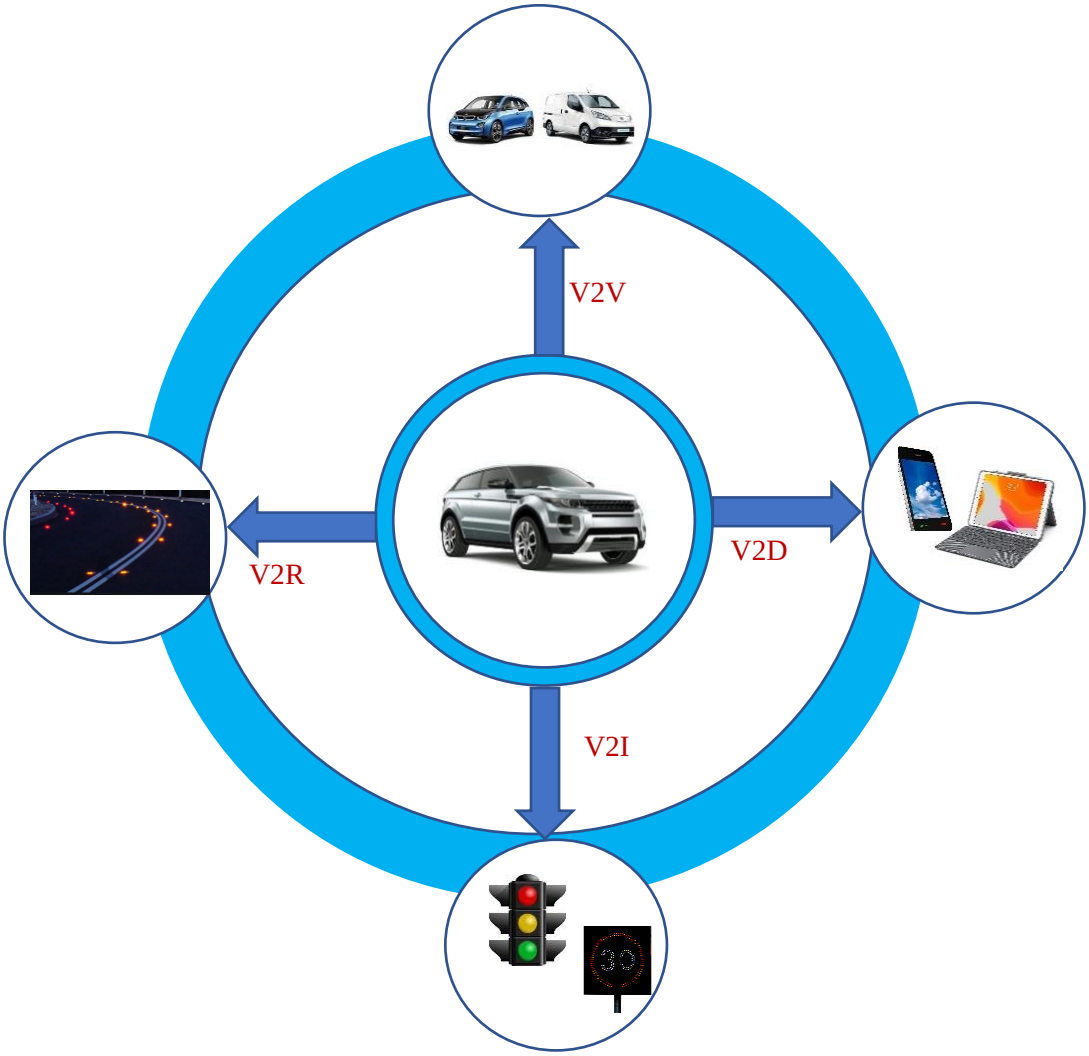

Figure 2.1: Illustration of VLC applications in ITS

2.3 Robustness to the Noise

2.3.1 Sunlight

Sunlight-induced noise is a major issue in vehicular VLC systems during the day, when illumination levels can reach 10 mW/cm^2 compared to µW/cm^2 for intensity-modulated HLs and TLs [50]. Saturation of the optical Rx can also result from high level of ambient light. Figure 2.2 illustrates a typical vehicular VLC link during daytime. It is worth noting that, most of the studies on vehicular VLC have not considered the impact of sunlight noise, hence this was investigated, and empirical solar irradiance measurements were carried out, which are part of this thesis contribution. Among the few works on solar irradiance is [75], where the solar irradiance's effect on VLC systems was evaluated in terms of BER, SNR degradation, and data rates. The link's efficiency was greatly improved over a short transmission span of 3 m while using an optical bandpass blue filter.

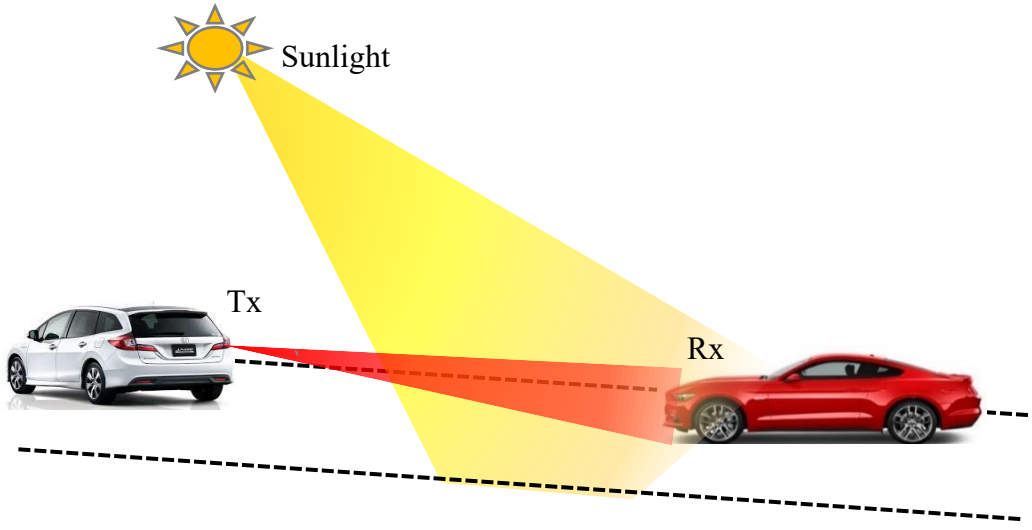

Figure 2.2: A vehicular VLC link during daytime

The effects of sunlight irradiance and other external light sources on vehicular VLC systems were investigated in [76] in terms of BER, data rates, and SNR across various months of the year, with and without an optical blue filter. The results showed a considerable improvement in the achievable data rates and average BER, for example, using an optical blue filter, the average BER improved from 2×10^{-3} to 3×10^{-5} in January. Different noise cancellation methods were also proposed, like wavelet-based signal processing for indoor VLC and differential Rx-based hardware. However, no real-time denoising has been successfully demonstrated yet experimentally owing to complexity as highlighted by [77], particularly for outdoor VLC with high sunlight noise. Moreover, a possible solution to improve the robustness to noise is to use a narrow AFOV Rx as experimentally verified in [71], where the SNR is significantly enhanced but at the expense of the mobility. Note, mobility is also a critical issue for vehicular VLC if the propagating beam is outside the AFOV, therefore resulting in the link loss. Moreover, the effect of sunlight noise on the performance of a vehicular VLC system at a relatively low speed of 30 km/h was examined in [77]. Note that, since the obtained power levels decrease with increasing transmission distance, the impact of sunlight noise becomes more critical as the communication distance increases, hence a wider range of driving speeds/communication distance needs to be investigated. Thus, this was considered and investigated as part of this research work with results presented in Chapter 3.

2.3.2 Fog

Weather effects such as fog and rain/snow also affect the VLC link, through a combination of absorption and scattering [78], impairing the communication link of which have been sparsely reported in literature. In [79], a point-to-point outdoor hybrid link, combining LED based OWC and 60 GHz technologies was demonstrated and the

effect of visibility limiting condition was demonstrated in terms of its effect on the achieved data rates over a 4.5 months period for visibility ranges of 94-20000 m based on an infrared LED only with a centre wavelength of 850 nm. Results obtained for the aggregate minimal, average and maximal data rates of the hybrid link were 230, 750 and 880 Mbps over a 100 m link span. In [80], two fog conditions, namely light and heavy fog were experimentally demonstrated. However, the fog conditions considered did not relate to any specific visibility figures, as the density of the fog scenarios were not quantified. Moreover, in [53] comprehensive simulation-based investigation was carried out to study the effect of rain and fog on vehicle-to-vehicle links using an advanced ray tracing software and considering a high-beam HL and PD as the Tx and Rx, respectively. A path loss model in terms of transmission range was developed, with the link span falling from 72 to 26 m in the presence of heavy fog with a visibility of 10 m at a target BER of 10^{-6} for the link employing 2-pulse amplitude modulation scheme.

The channel coefficient for fog H_{fg} can be obtained by applying Beer's law [81] describing light absorption and scattering in a medium as:

$$H_{\mathrm{fg}} = e^{-A_{\mathrm{fg}} L_s}, \tag{2.1}$$

where L_s is the link span and A_{fg} is the fog attenuation. Beer's law describes the attenuation of a light beam in the atmosphere as in [81] and visibility is usually used to quantify fog attenuation in optical systems. Utilizing Mie scattering model to reflect the attenuation, the link visibility is obtained from the fog attenuation A_{fg} as [82]:

$$A_{\mathrm{fg}} = \frac{3.91}{V}\left(\frac{\lambda}{550}\right)^{-q}, \tag{2.2}$$

where λ, V, and q represent the wavelength in nm, meteorological visibility in km, and the distribution size of scattering particles, respectively. The latter is given by Kim's model as [83]:

$$q = \begin{cases} 1.6 & V > 50 \text{ km} \\ 1.3 & 6 \text{ km} < V < 50 \text{ km} \\ 0.16V + 34 & 1 \text{ km} < \text{V} < 6 \text{ km}. \\ V - 0.5 & 0.5 \text{ km} < V < 1 \text{ km} \\ 0 & V < 0.5 \text{ km} \end{cases} \tag{2.3}$$

The average received optical power for the line of sight (LOS) link at the Rx under clear weather is given by [84]:

$$P_r = P_T \, H_{\text{LOS}} + n(t), \tag{2.4}$$

where P_T is the transmit power, H_{LOS} is the free space channel DC gain, and $n(t)$ is the additive white Gaussian noise including the ambient light induced shot noise, the signal and dark current related shot noise sources and the thermal noise. Consequently, applying the channel coefficient for fog to (2.4), the average received optical power for the LOS link at the Rx under fog is expressed as:

$$P_{\text{r\_fog}} = P_T \, H_{\text{LOS}} \, H_{\text{fg}} + n(t). \tag{2.5}$$

Figure 2.3 shows captured images of a vehicle TL with and without visibility limiting conditions.

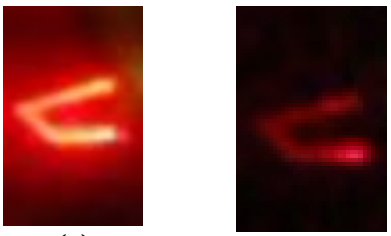

(a) (b)

Figure 2.3: Captured images of a vehicle TL at a distance of 7.5 m under: (a) clear weather, and (b) 10 m meteorological visibility

2.3.3 Turbulence

Turbulence is another atmospheric effect caused by the irregularities in temperature and pressure along the path of propagation. This, therefore, results to refractive index variations, leading to phase and amplitude fluctuation of the propagating beam, thereby causing fading of the optical signal and consequently a reduction in the average SNR [54]. Figure 2.4 illustrates a wavefront before and after passing through a turbulent channel. In this case, the input wavefront is planar, which passes through a turbulent channel with different sizes of turbulent eddies [85]. Consequently, this leads to a distorted output wavefront resulting from the random changes in the refractive index along the propagation path (modelled as turbulent eddies).

The refractive index structure parameter C_n^2 (in $m^{-2/3}$) is most commonly used to describe the strength of turbulence, which is given by [86, 87]:

$$C_n^2 = (79 \times 10^{-6} \frac{P}{T^2})^2 C_T^2, \tag{2.6}$$

where P denotes the pressure in millibar, T the temperature in Kelvin, and C_T^2 the temperature structure parameter, which is linked to the universal 2/3 power law of temperature fluctuations given as [87]:

$$D_T(L_T) = \langle (T_1 - T_2)^2 \rangle = \begin{cases} C_T^2 L_T^{\frac{2}{3}}, & l_o \ll L_T \ll L_o \\ C_T^2 l_o^{-\frac{4}{3}} L_T^2, & 0 \ll L_T \ll l_o \end{cases}, \tag{2.7}$$

where $D_T(L_T)$ is the structure function of temperature, L_T is the separation span between two points with temperatures of T_1 and T_2, while the inner and outer scales of the small temperature fluctuations are denoted by l_o and L_o, respectively.

Another important parameter, which is adopted to reflect the turbulence regime, is the Rytov variance σ_R^2, which indicates the irradiance fluctuations of the optical signal resulting from turbulence and is given for a plane wave as [87]:

$$\sigma_R^2 = 1.23 C_n^2 k^{\frac{7}{6}} L_s^{\frac{11}{6}}, \tag{2.8}$$

where the wave number $k = \frac{2\pi}{\lambda}$ (λ is the wavelength), L_s is the link span. The turbulence conditions are categorized as follows based on σ_R^2 [87]:

i. Weak regime, $\sigma_R^2 < 1$
ii. Moderate regime, $\sigma_R^2 \sim 1$
iii. Strong regime, $\sigma_R^2 > 1$
iv. Saturation regime, $\sigma_R^2 \to \infty$.

The scintillation index σ_I^2 is also used to quantify the normalized intensity variance generated by turbulence and it is given by [88]:

$$\sigma_I^2 = \frac{\langle I^2 \rangle}{\langle I \rangle^2} - 1, \tag{2.9}$$

where $\langle . \rangle$ represents the ensemble average, and I denotes the intensity of the optical beam at the Rx.

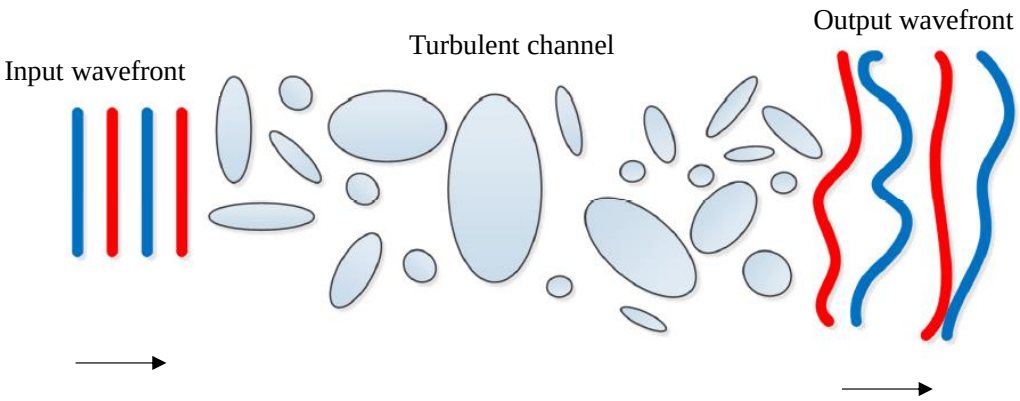

Figure 2.4: Illustration of turbulence effects on the wavefront [85]

Among the very few reports on the studies of atmospheric turbulence in VLC is [89], where the effects of turbulence by means of simulations were investigated. In [89] the signal quality under the effects of turbulence was evaluated in terms of the SNR, BER and channel capacity metrics of the VLC system, and the results presented showed that, there was a considerable variation in the BER as a function of the turbulence strengths. For example, the BER at a link span of 100 m (modulation type and the data rate were not specified), for C_n^2 of 1×10^{-12} and 1×10^{-13} $m^{-2/3}$ were 4×10^{-4} and 3×10^{-8}, respectively. In [90], the performance of a VLC system under the effects of turbulence was investigated experimentally under a controlled laboratory environment, but the strength of turbulence studied was not specified or characterised. Results presented showed a slight increase in the BER in case of turbulence, for example the BER for a 128-quadrature amplitude modulation format rose from 3×10^{-5} to ~2×10^{-4}. Consequently, as earlier mentioned, very little has been reported generally on the effect of weather conditions on VLC systems; hence this thesis also presents experimental based investigations carried out on turbulence and fog effects in Chapter 5.

Different turbulence models have been proposed to describe the probability density function (PDF) of the randomly fluctuating signal irradiance due to turbulence, however, because of the simplicity of the lognormal turbulence model, it is commonly used for weak to moderate turbulence regimes. Nevertheless, this model understates the behaviour of the irradiance fluctuations as turbulence intensity increases [87]. As a result, a modified Rytov theory was proposed in [87] to address large-and small-scale scintillations in moderate to strong turbulence conditions, in which the optical channel was described as a function of disturbances that result from small-and large-scale atmospheric effects in relation to factors that act like a modulation mechanism. This

model presumes that Gamma distributions direct large-and small-scale irradiance variations to build a PDF model of irradiance that is related to atmospheric conditions while remaining consistent with scintillation theory [87]. A very appropriate model as seen in [91-92] is the Gamma-Gamma (GG) which covers weak to strong turbulence regime. The PDF of the GG distribution is given by [87]:

$$p(I) = \frac{2(\alpha\beta)^{\frac{\alpha+\beta}{2}}}{\Gamma(\alpha)\Gamma(\beta)} I^{\left(\frac{\alpha+\beta}{2}\right)-1} K_{\alpha-\beta}\left(2\sqrt{\alpha\beta I}\right), \qquad I > 0 \tag{2.10}$$

where α and β are the effective number of large- and small-scale eddies of the scattering process, respectively. $\Gamma(.)$ and $K_{\alpha-\beta}(.)$ denotes Gamma function and the modified Bessel function of the 2nd kind of order (α-β), respectively. For the plane wave radiation at the Rx, α and β are given respectively, as [87]:

$$\alpha = 1/(e^{0.49\sigma_I^2/a} - 1), \tag{2.11}$$

$$\beta = 1/(e^{0.49\sigma_I^2/b} - 1), \tag{2.12}$$

where $a = \left(1 + 1.11\sigma_I^{\frac{12}{5}}\right)^{\frac{7}{6}}$ and $b = \left(1 + 0.69\sigma_I^{\frac{12}{5}}\right)^{\frac{5}{6}}$.

Alternatively, a generalised statistical model of Malaga distribution can be used for modelling the irradiance fluctuations under all turbulence conditions [71]. The merit of this model includes a closed-form and a mathematically tractable expression for the fundamental channel statistics under all turbulence regimes as well as unifying most of the pre-existing statistical models for irradiance fluctuations [93-94]. The PDF of Malaga distribution is given as [94]:

$$fI_{\alpha}(I_{\alpha}) = A\sum_{k'=1}^{\beta'} a'_{k'} I_{\alpha}^{\frac{\alpha'+k'}{2}-1} K_{\alpha-k'}\left(2\sqrt{\frac{\alpha'\beta' I_{\alpha}}{\gamma'\beta'+\Omega'}}\right),\ I_{\alpha} > 0 \quad (2.13)$$

where

$$A \triangleq \frac{2\propto'^{\frac{\propto'}{2}}}{\gamma^{\lambda+\frac{\propto'}{2}}\Gamma(\propto')}\left(\frac{\gamma'\beta'}{\gamma'\beta'+\Omega'}\right)^{\beta'+\frac{\propto'}{2}}, \quad (2.14)$$

$$a'_{k'} \triangleq \binom{\beta'-1}{k'-1}\frac{(\gamma'\beta'+\Omega')^{1-\frac{k'}{2}}}{(k'-1)!}\left(\frac{\Omega'}{\gamma'}\right)^{k'-1}\left(\frac{\alpha'}{\beta'}\right)^{\frac{k'}{2}}, \quad (2.15)$$

$$\Omega' \triangleq \Omega + 2\rho b_0 + 2\sqrt{2\rho b_0 \Omega}\cos(\varphi_A - \varphi_B), \quad (2.16)$$

where $2b_0$ is the average power of the total scatter components, β' is a natural number representing the amount of turbulence, $\rho(0 < \rho < 1)$ is the amount of scattering power that is coupled to the LOS component, α' is related to the effective number of large scale cells of the scattering process, Ω is the average power of the LOS component, γ'= $2b_0(\rho - 1)$, and φ_A, φ_B are the LOS phases and coupled to LOS components.

2.4 Communication Range for Automotive Applications

The next challenge is to achieve long distance VLC links for automotive applications, i.e., increase the communication distance to meet the demands of the vehicular environment.

2.4.1 Vehicular VLC Rx configuration/type

The communication range of PD based vehicular VLC links is usually lower than the camera-based links, although with higher data rates. One of the longest reported communication range with PD-based Rxs was in [14] achieving a 120 m span, which was obtained via numerical simulations considering empirical transmit power measurements of vehicle HL's but without considering the effect of ambient noise, (which is the major noise source and challenge for vehicular VLC links) and a PD with relatively high sensitivity was employed. Another reported relatively long-distance PD-based link was up to a 70 m link span at a data rate of 50 Mb/s with a vehicle's HL as Tx [95], but only a low background radiation was taken into consideration. Under high ambient light conditions, these link spans achieved in the former and latter works above will drastically reduce. One simple way to extend the communication range will be to increase the transmit power. However, since the light wave carrier is perceptible by the human eyes, there are regulations that govern the beam pattern and the range of luminous flux of particularly HLs so as not to cause glare for other road users. Moreover, optical concentrators (OCs) are usually used to increase the optical power density at the Rx to achieve long ranges. Notably, the AFOV of the Rx reduces with increasing lens focal length f used at the Rx, consequently decreasing the mobility capability of the system as discussed in the next subsection. Hence this thesis also presents a comprehensive mathematically analysis on the required AFOV for vehicular VLC links, which is presented in Chapter 3. Note that, for camera-based links, relatively longer transmission ranges are obtainable, but this is limited to the frame rate of the camera as the size of the image of the light source projected on the image sensor (IS) drastically reduces as the link span increases (see Figure 2.5 for the focused image), thus not enabling RS based capturing, which offers higher data rates than the camera's

frame rate. Notably, Figure 2.5 illustrates the drop in the diameter of the captured focused Tx image as the link distance increases, while that of the defocused image after some distance remains constant, which is obtained from empirical measurements. Consequently, we investigate and present original contributions in Chapter 4 to extend the link span and data rates of an RS-based OCC link.

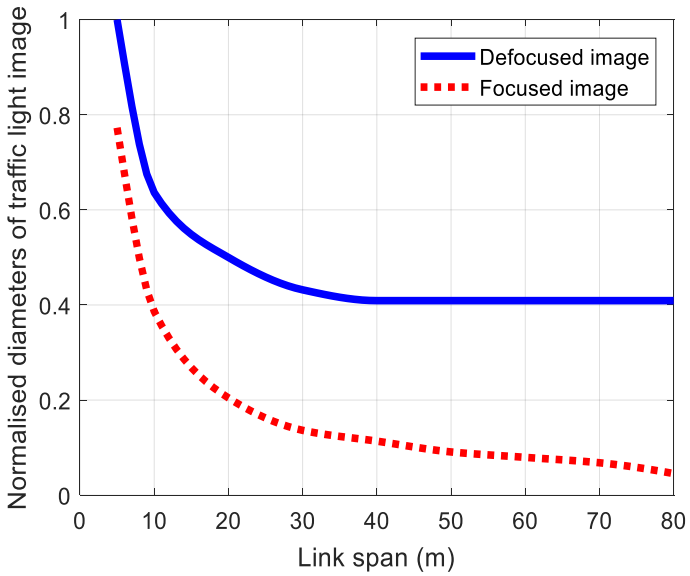

Figure 2.5. The normalised diameter of traffic light image with reference to the defocused mode versus link span

2.4.2 The vehicle's light characteristics

In [93], an analytical model for BER performance as a function of communication span for vehicular VLC was reported using a HL beam pattern model and different communication geometries. It was discovered that (*i*) due to the asymmetric beam pattern of the low beam HL, there were sharp degradations in the BER performance distribution to the left-hand side in the vertical plane; and (*ii*) the achievable transmission link span increased when the PD and HLs heights were around 0-0.2 and 0.66 m, respectively.

It is worth noting that, most vehicular VLC studies, including the aforementioned references, have focused on high- or low-beam HLs, which are commonly used at night or in low-visibility situations (i.e., rain or fog). As compared to the high- and low-beam lights used for road illumination, the transmit power levels for HLs used during daytime under clear weather conditions are relatively low, usually referred to as the 'always on' HLs/TLs.

The optical radiation pattern of a single HL and TL was evaluated extensively in [96], and several vehicle mobility traces with two-dimensional positions were also collected. Both sets of data were combined to conduct an empirical analysis and obtain experimental distributions of received power for HL- and TL-based Txs. As a result of the large variations in radiation characteristics and transmit power levels between the HL and the TL, the problem of link asymmetry was discovered. It was revealed that in 80% of the instances, the received power for the HL-based Tx was at least 22 dB higher than that for the TL-based Tx. The paper proposed that a new system (or protocol) structure be implemented to resolve the link asymmetry problem in vehicular VLC systems to increase data throughout. In [15], the effect of vehicle's HL and TL illumination patterns on communication performances between vehicles travelling on the same and different lanes was investigated and a novel vehicular VLC simulation model based on empirical data measurements was developed. The impact of the angle of incidence was analysed based on the received signal power, SNR, and packet delivery ratio metrics, and the performance of vehicular VLC was evaluated using the established model. The authors indicated that using the TL, it was only possible to communicate with vehicles on adjacent lanes over a transmission range of up to 10 m. From the foregoing, a robust Tx design is needed that meets the requirements of the

vehicular environment in terms of communications range and coverage area, which this research work investigates and presents original contributions in Chapter 3.

2.4.3 Multi-hop transmission

Furthermore, the use of relay nodes has been proposed in [97-98] to extend the communication range in OWC systems. In [98], relay-based systems were proven to be viable in mitigating channel fading over short transmission ranges using AF and DF relaying schemes. With a single relay at a target outage likelihood of 10^{-6}, results showed an enhanced power margin of up to 12.2 dB and 18.5 dB, for the AF and DF schemes respectively. Moreover, in [99], a multi-user VLC system where other users acted as relays was introduced. For inter-vehicle communication systems, a similar approach using vehicles as relay nodes, where each vehicle forwards the transmission was proposed in [100] (see Figure 2.6, which illustrates a relay-assisted vehicular VLC link). In [101] a multi-hop relay maritime VLC system was proposed and in [102] a relay-assisted VLC system was proposed where the improvements in transmission gain with cooperative VLC system in comparison to direct links was presented. Consequently, it was shown that the link with spatial multiplexing, multi-hop transmission offered reduced average signal power of -59 dBm for a single hop (for a 16 m link span) compared with -27 dBm for direct transmission (for a 12 m link span). In [103], the authors investigated a scenario where terminals can play a relay node role to extend the coverage of a VLC downlink for a single hop and multi-hop coverage range of 2 and 4 m, respectively. However, not much has been reported in the literature on relay-assisted VLC for vehicular links, thus, this thesis presents results of investigations carried out for relay-assisted vehicular VLC as part of its contributions in Chapter 6.

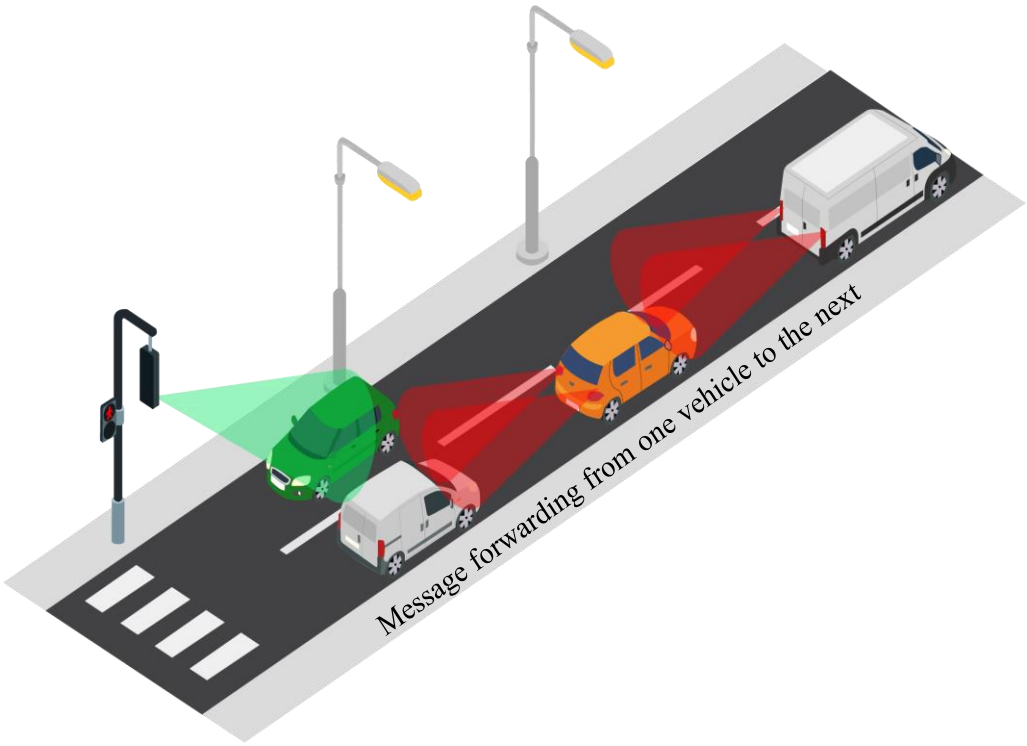

Figure 2.6: Illustration of relay-assisted vehicular VLC link

2.5 Mobility Enhancement

Another key challenge is to enhance the mobility of the vehicular VLC system, since vehicles are constantly in motion and are non-stationary, it is important that the vehicular VLC system's AFOV is able to accommodate misalignment conditions. Importantly, the orientation of the Tx and Rx determines the system's performance. To address this, in [104-105], a tracking mechanism was proposed. The system consisted of a narrow AFOV PD-based Rx (only 5^{o}), a low-cost camera with a wider AFOV (20^{o}) used for the detection of the emitter and motors to align the PD to the Tx [104]. This solution proved to be quite effective in addressing the mobility and even robustness to noise, however the complexity of the design limited the acceptability of this technique

[50]. Moreover, a similar method was proposed in [106], where instead of a camera, two light sensors are used to measure the ambient light power and decision was made by the Rx on the direction of the larger power, and to keep track of that direction. Note that, under intense sunlight, the signal power of the modulated light may be lower than the incident sunlight depending on the distance, and this may cause wrong decision in alignment as the system was tested in isolation without considering the effect of sunlight and other vehicle lights. A different approach is proposed in [107], which addresses the vehicular VLC mobility issue by proposing the use of a relay vehicle, where LOS link to a desired vehicle is not possible but could be achieved through a relay vehicle [107]. Furthermore, in [108], different positions for installment of PD-based Rxs such as at the back and sides of the vehicle were studied and the results presented, which depended on the geometry of the communicating cars. In [109-112], the angle diversity Rxs were used to create a relatively larger AFOV for the system. Notably, the camera-based Rxs offer higher AFOV up to 130-160 ^{o} for vehicle dashboard cameras [113] due to a relatively larger sensor size in combination with the use of lower f of lens values. Importantly, there is the need to carry out accurate channel and geometrical modelling and analysis to determine the optimum positioning/geometrical design for vehicular Rxs and the required AFOV for vehicular applications. This is to allow full mobility of the system, which this research work analyses and provides insights into in Chapter 3.

2.6 Summary

This chapter discussed in detail the major challenges of the vehicular VLC system, which are (*i*) increasing the robustness to noise, where the sunlight noise is the greatest noise source during daytime of which further details are presented in Chapter 3. Atmospheric effects such as fog and turbulence were also discussed in detail; (*ii*)

increasing the communication link span; and (*iii*) improving the mobility. Related literatures were reviewed based on the outlined major vehicular VLC challenges including techniques that have been proposed to mitigate the challenges and what this thesis contributes in relation to the challenges of the vehicular VLC system. The used cases specified in the standards of the RF based technology for vehicular communications (DSRC) was also highlighted.

CHAPTER 3
ANALYSIS OF VEHICULAR VLC AND IR WITH SUNLIGHT NOISE

3.1 Introduction

ITS depend on connectivity, cooperation, and automation of vehicles to enhance the transportation system's safety and performance. Achieving robust V2X connectivity (links) is key for the practical implementation of vehicular VLC systems in ITS that needs detailed investigation. In this chapter, insights into the required Rx's AFOV considering key parameters such as the road lane widths, vehicle widths, as well as the positions of the Tx and the Rx are provided. Insights into the Tx's coverage profile, and demonstration of the obtainable AFOV of the Rx based on varying optical detector sizes with varying *f* of lenses are also provided. Notably, a V2V scenario is considered here as it presents the greatest challenge in terms of the achievable link distance than other application scenarios. It is noteworthy that, most works reported on vehicular VLC are based on using a single light module type (i.e., one vehicle model), which may narrow down the conclusions drawn from the results. Moreover, most previous works have concentrated more on the use of HLs, which have higher transmit power than TLs. Therefore, in this work, four TLs from different vehicles are characterized by measuring their radiation patterns and P_T. In addition, a link power budget analysis is preformed

to determine the feasibility of vehicular VLC links using these TLs as the Txs for a range of TL irradiance angles with respect to the vehicle's speeds. Consequently, due to the very short link spans (translating to driving speeds) achievable using the TLs, the inclusion of IR LEDs (a unique IR-LED array) in HLs and TLs-based Txs is proposed, which facilitates long transmission spans at high data rates. It is shown that, the proposed system is highly robust under the sunlight environment, which is the main noise in vehicular VLC systems. In addition, the proposed scheme deals with the link asymmetry issue reported in [96], since both the front and rear vehicle's Txs will have the same P_T and radiation characteristics. This Chapter is organised as follows: vehicular VLC configuration analysis is presented, followed by the performance analysis of vehicular VLC with the characterised TLs as Txs and a PD based Rx. Noise analysis and the performance evaluation of the proposed IR light communication system are also presented and finally a summary of the Chapter is given.

3.2 The V2V VLC Configuration Analysis

The composition of a typical V2V VLC system is shown in Figure 3.1(a)-(c), which comprises of the TL-based Tx (Vehicle 1) and a PD-based Rx (Vehicle 2). For the purpose of illustration, only a single TL is used. Notably, the orientation of the Txs in relation to the Rx and their beam profiles as well as the AFOV of the Rx are very crucial in vehicular VLC and will determine the performance of the link. Note that, when an imaging lens is used at the Rx, the beam profile of the Tx does not matter much as since only the image of the Tx is projected onto the PD as in a camera. The channel DC gain of a LOS non-imaging vehicular VLC link with a non-symmetrical Tx radiation pattern can be expressed as:

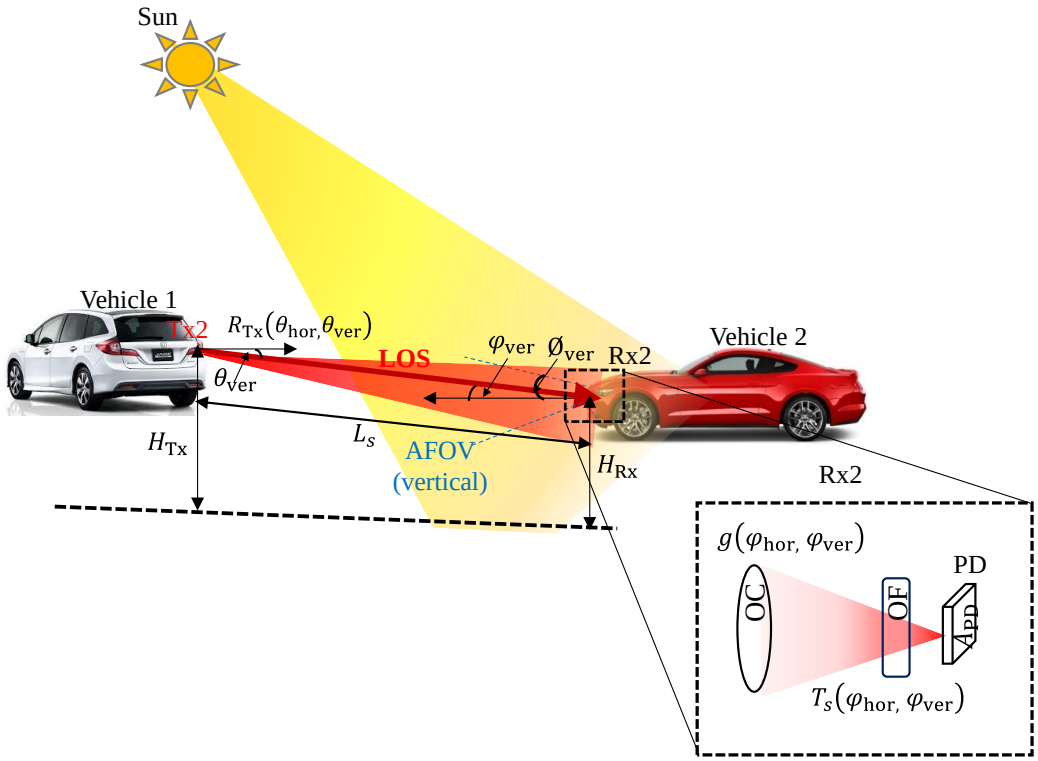

(a)

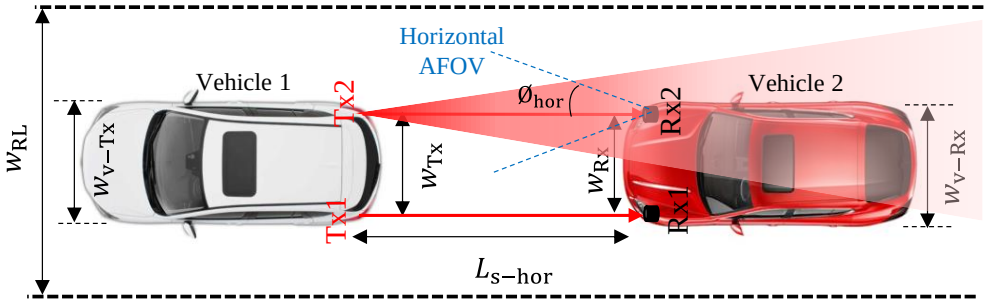

(b)

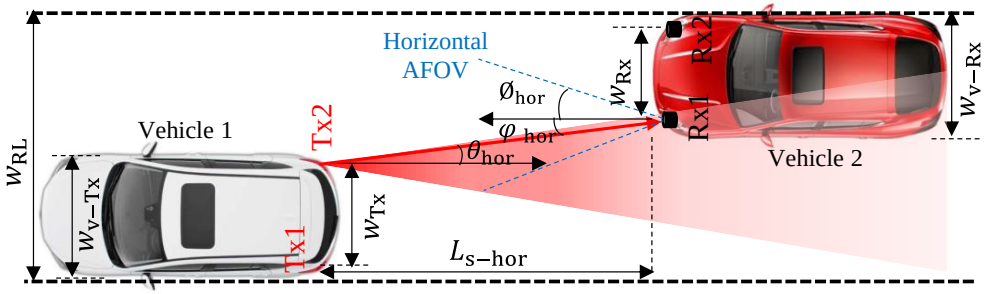

(c)

Figure 3.1: Vehicular VLC configuration: (a) side view, (b) top view for perfect alignment scenario, and (c) top view with horizontal Tx and Rx misalignment (offset)

$$H_{\mathrm{LOS}} = \begin{cases} \dfrac{A_{\mathrm{PD}}\, T_s(\varphi_{\mathrm{hor},}\, \varphi_{\mathrm{ver}})\, g(\varphi_{\mathrm{hor},}\, \varphi_{\mathrm{ver}})\, R_{\mathrm{Tx}}(\theta_{\mathrm{hor},}\theta_{\mathrm{ver}})}{{L_S}^2}, \\ \quad 0 \le \varphi_{\mathrm{hor}} \le \emptyset_{\mathrm{hor}} \ \text{and} \ 0 \le \varphi_{\mathrm{ver}} \le \emptyset_{\mathrm{ver}} \\ \\ 0, \qquad \varphi_{\mathrm{hor}} > \emptyset_{\mathrm{hor}} \ \text{ or } \ \varphi_{\mathrm{ver}} > \emptyset_{\mathrm{ver}} \end{cases} \tag{3.1}$$

where φ_{ver} and φ_{hor} are the vertical and horizontal incidence angles, respectively, A_{PD} is the active area of the PD, $R_{\mathrm{Tx}}(\theta_{\mathrm{hor},}\theta_{\mathrm{ver}})$ denotes the radiation pattern (normalized beam profile) of the Tx at vertical and horizontal irradiance angles θ_{ver} and θ_{hor}, respectively, $\emptyset_{\mathrm{ver}}$ and $\emptyset_{\mathrm{hor}}$ represents the vertical and horizontal AFOV semi angle of the Rx, L_S is the link span, $g(\varphi_{\mathrm{hor},}\, \varphi_{\mathrm{ver}})$ and $T_s(\varphi_{\mathrm{hor},}\, \varphi_{\mathrm{ver}})$ are the gains of the optical concentrator (OC) and optical filter (OF), respectively. Note, using (3.1) the specific radiation pattern of the Tx can be incorporated, which may not be symmetrical as in Lambertian radiant intensity model. The gain of a non-imaging OC (NIOC) can be expressed as $A_{\mathrm{coll}}/A_{\mathrm{PD}}$ [114], where A_{coll} is the collection area of the NIOC.

3.2.1 Analysis of horizontal/vertical semi-AFOV for V2V VLC with imaging OC (IOC)

When a convergent lens (i.e., IOC) is used at the Rx side (i.e., with a PD), as in a camera, an image of the Tx is captured on the PD-based sensor provided the Tx is within the Rx's AFOV. It worthy of note that, NIOCs do not produce an image of the Tx as do IOCs. First, we analyse the required horizontal (azimuth) semi-AFOVs (HS-AFOVs) for the Rxs 1 and 2 for the worst-case scenario, where vehicles are positioned at the opposite sides of the lane, see Figure 3.2. Note, for the Rxs 1 and 2 to capture a single Tx and or two Txs, the required HS-AFOV are φ_{12}, φ_{22}, φ_{11}, φ_{21}, respectively.

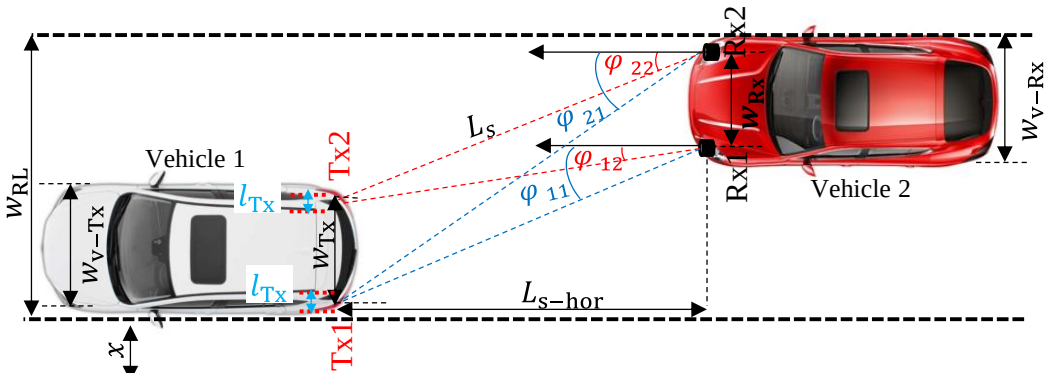

Figure 3.2: V2V VLC configuration showing required horizontal AFOV

Thus, to obtain the required HS-AFOV for two vehicles travelling on the same lane, it is necessary to consider both the lane and vehicles' widths as well as the locations of the Rx and the Tx. Therefore, the required HS-AFOV for the Rx can be expressed as:

$$\varphi_{12} = \arctan\left(\frac{w_{RL} - \left(\frac{w_{v-Tx} - w_{Tx}}{2}\right) - \left(w_{Tx} - \frac{l_{Tx}}{2}\right) - \left(\frac{w_{v-Rx} - w_{Rx}}{2}\right) - w_{Rx}}{L_{s-hor}}\right), \quad (3.2)$$

$$\varphi_{22} = \arctan\left(\frac{w_{RL} - \left(\frac{w_{v-Tx} - w_{Tx}}{2}\right) - \left(w_{Tx} - \frac{l_{Tx}}{2}\right) - \left(\frac{w_{v-Rx} - w_{Rx}}{2}\right)}{L_{s-hor}}\right), \quad (3.3)$$

$$\varphi_{11} = \arctan\left(\frac{w_{RL} - \left(\frac{w_{v-Tx} - w_{Tx}}{2}\right) + \frac{l_{Tx}}{2} - \left(\frac{w_{v-Rx} - w_{Rx}}{2}\right) - w_{Rx}}{L_{s-hor}}\right), \quad (3.4)$$

$$\varphi_{21} = \arctan\left(\frac{w_{RL} - \left(\frac{w_{v-Tx} - w_{Tx}}{2}\right) + \frac{l_{Tx}}{2} - \left(\frac{w_{v-Rx} - w_{Rx}}{2}\right)}{L_{s-hor}}\right). \quad (3.5)$$

where w_{RL} denotes the width of the road lane, L_{s-hor} is the horizontal link span between the Tx and the Rx, w_{Tx}, and w_{Rx}, are the spacing between the Txs and the Rxs and, w_{v-Tx} and w_{v-Rx} represents the width of the transmitting and receiving vehicles, respectively and l_{Tx} is the length of the Txs (Figures 3.1 and 3.2). Note that, for the cases where one of the vehicles may move outside the lane, we replace w_{RL} by $w_{RL} + x$ in (3.2) - (3.5), where x denotes the deviation outside the lane edge. Furthermore, (3.2)

- (3.5) can be applied to vehicles on separate lanes where w_{RL} becomes $2w_{\mathrm{RL}}$ or $3w_{\mathrm{RL}}$ for situations where one of the vehicles is on the next or the next two lanes, respectively.

The required vertical semi-AFOV (VS-AFOV) for the scenario depicted in Figure 3.1(a) can be expressed as:

$$\varphi_{\mathrm{ver}} = \arctan\left(\frac{\Delta H}{L_{\mathrm{s-hor}}}\right), \tag{3.6}$$

where the offset between the Rx's and Tx's vertical heights is $\Delta H = |H_{\mathrm{Tx}} - H_{\mathrm{Rx}}|$ with H_{Tx} and H_{Rx} denoting the vertical Tx and Rx heights, respectively. The required VS-AFOV and HS-AFOV as a function of the link distance for vehicular VLC are depicted in Figure 3.3, which is generated using (3.2) - (3.6) and the key parameters are listed in Table 3.1. Typical vehicle widths (such as saloons, hatchbacks, superminis, sport utility vehicles and city cars) are within the range of 1.4 - 2 m [115]. Hence a median value of 1.7 m was selected, and assuming a realistic distance of 0.25 m from the centre of each Tx/Rx to the car edge, the distance between the Txs and Rxs are obtained to be 1.2 m. Also, a realistic lens with a low value of *f* (assuming same value of *f* for the lens diameter in order to maximise the optical gain) was considered in order to avoid using large optics with a low AFOV at the Rx side. The length of the Tx considered falls within the range obtained from empirical measurements for the vehicle TLs.

From Figure 3.3, it can be seen that, HS-AFOV exponentially decays with the link distance (i.e., drops sharply at the beginning and continues slowly). For example, for the Rx2 the required HS-AFOV rises ~ 5 times as the link distance reduced from 10 to 2 m. For the Rx1, the required HS-AFOV is lower than the Rx2 since it is closer to the Txs. Moreover, for VS-AFOV an exponential profile is also exhibited with higher values for larger ΔH below the link distance of 20 m.

Table 3.1: Key geometry parameters and simulation values

Parameter	**Symbol**	**Value**
Lane width	w_{RL}	2.5 m
Width of Rx vehicle	$w_{\mathrm{v-Rx}}$	1.7 m
Width of Tx vehicle	$w_{\mathrm{v-Tx}}$	1.7 m
Distance between Tx1 & Tx2	w_{Tx}	1.2 m
Distance between Rx1 & Rx2	w_{Rx}	1.2 m
Length of Txs	l_{Tx}	0.1 m
Horizontal link span	$L_{s-\mathrm{hor}}$	1-50 m
Vertical Rx and Tx offset	ΔH	0.25- 0.75 m
Focal lengths of lens	f	25.4–50.0 mm
PD's surface area	A_{PD}	0.2 – ~2 cm^2

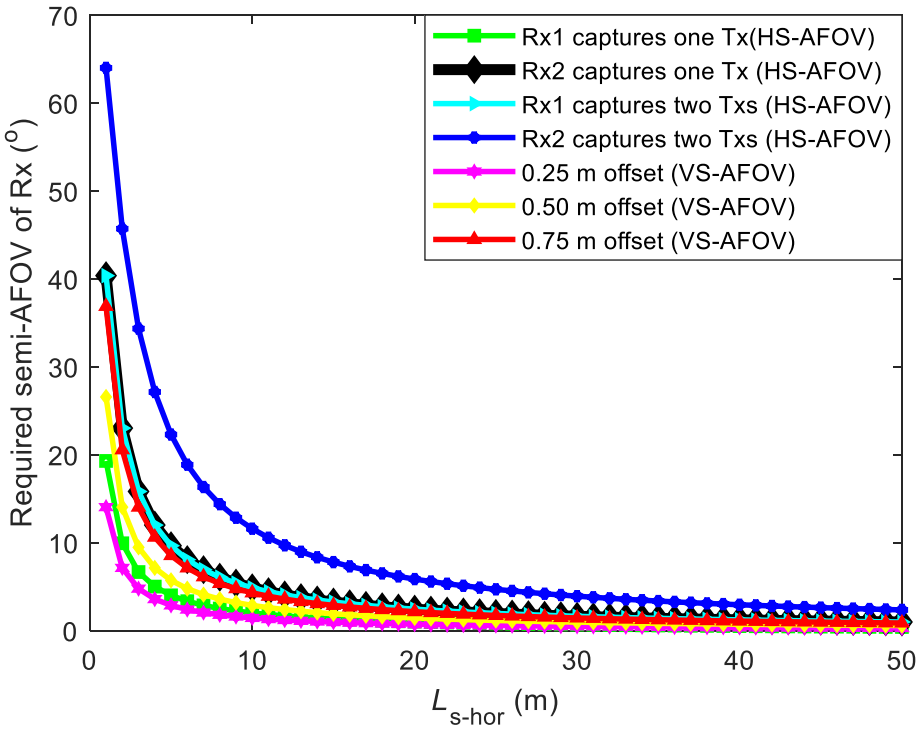

Figure 3.3: The required VS-AFOV and HS-AFOV of Rx as a function of the $L_{\mathrm{s-hor}}$ for two vehicles on the same lane

Note that, increasing the vertical offset between the Rx and the Tx beyond the vertical AFOV of the Rx will require increasing the vertical AFOV to capture the Tx while the horizontal AFOV needs no adjustment and vice versa.

3.2.2 Semi-AFOV based on the lens focal length and the PD's size

When an imaging convergent lens (i.e., an IOC) is used to focus light onto the PD's surface to increase the received optical power density, the Rx's semi-AFOV reduces, which needs investigating to meet the required semi-AFOV for vehicular communications, see Figure 3.4. Notably, the obtainable semi-AFOV of a Rx depends on f of the lens and the PD's dimensions D_{PD}, which, for a circular rectilinear lens can be expressed as:

$$\emptyset_{\mathrm{S-AFOV}} = \arctan\left(\frac{D_{\mathrm{PD}}}{2f}\right), \tag{3.7}$$

$$\emptyset_{\mathrm{S-AFOV}} = \begin{cases} \emptyset_{\mathrm{hor}}, & D_{\mathrm{PD}} = w_{\mathrm{PD}}, \\ \emptyset_{\mathrm{ver}}, & D_{\mathrm{PD}} = h_{\mathrm{PD}}, \\ \emptyset_{\mathrm{diag}}, & D_{\mathrm{PD}} = \sqrt{{h_{\mathrm{PD}}}^2 + {w_{\mathrm{PD}}}^2}, \end{cases} \tag{3.8}$$

where w_{PD} and h_{PD} denotes the width and height of the PD and $\emptyset_{\mathrm{ver}}$, $\emptyset_{\mathrm{hor}}$, and $\emptyset_{\mathrm{diag}}$ is the vertical, horizontal, and diagonal semi-AFOVs of the Rx, respectively.

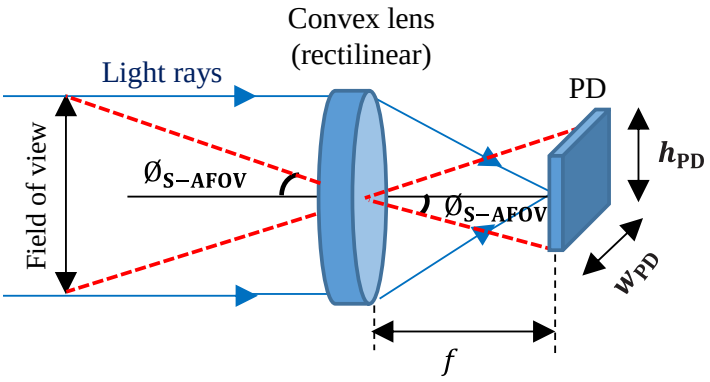

Figure 3.4: Relationship between semi-AFOV, lens focal length and the PD size

Figure 3.5 shows $\emptyset_{\text{ver}}$ or $\emptyset_{\text{hor}}$ as a function of the PD's surface area (where $h_{\text{PD}} = w_{\text{PD}}$) for a range of f. It can be observed that with an imaging convergent lens at the PD, $\emptyset_{\text{hor}}$ or $\emptyset_{\text{ver}}$ decreases with (increase in) f while it increases (logarithmic) with the PD's surface area.

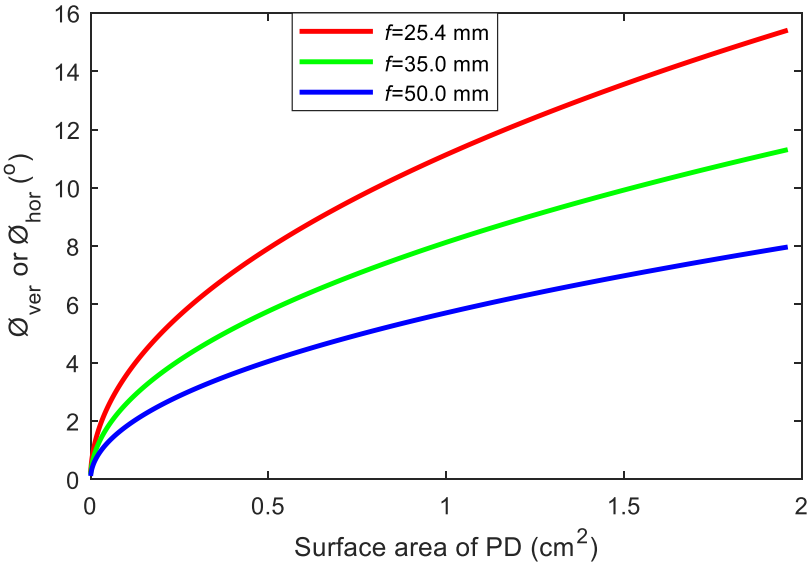

Figure 3.5: $\emptyset_{\text{hor}}$ or $\emptyset_{\text{ver}}$ versus the PD surface area for a range of f

3.2.3 Analysis of Tx's field of view (coverage profile)

Figure 3.6 depicts the beam coverage profile of the Tx, where L_1 represents the horizontal distance from the Txs to the beginning of the overlapping light area between Txs 1 and 2, which can be expressed as:

$$L_1 = w_{\text{Tx}}/(\tan\theta_{1/2-\text{in}} + \tan\theta_{1/2-\text{out}}), \qquad (3.9)$$

where $\theta_{1/2-\text{out}}$ and $\theta_{1/2-\text{in}}$ are the outer and inner half power angles of the Tx's beam, respectively, see Figure 3.6. Note that, $\theta_{1/2-\text{out}}$ and $\theta_{1/2-\text{in}}$ of each Tx is the angle

between the peak and the point on one side of the beam axis (right or left) where the received power is 50 % of the maximum. L_2 denotes the beam length of a single Tx and

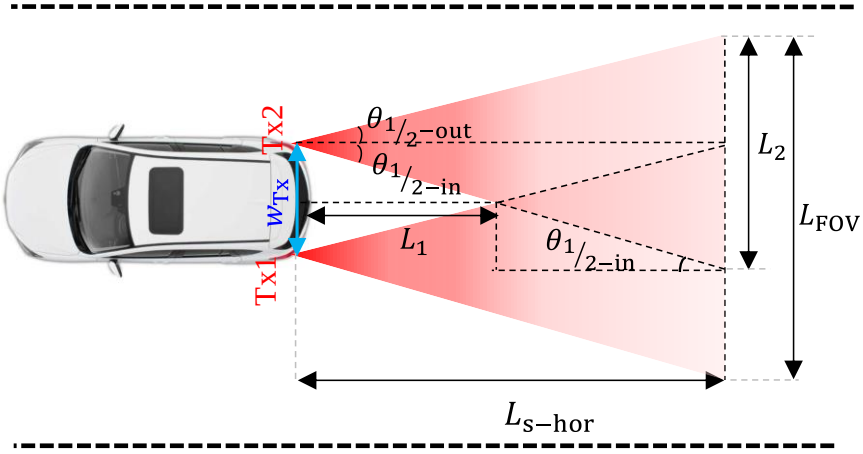

Figure 3.6: Tx's field of view coverage

L_{FOV} is the coverage length of both Txs beyond L_1, which can be expressed as:

$$L_2 = L_{s-hor}\left(\tan\theta_{1/2-in} + \tan\theta_{1/2-out}\right), \tag{3.10}$$

$$L_{FOV} = w_{Tx} + L_{s-hor}\left(\tan\theta_{1/2-in} + \tan\theta_{1/2-out}\right). \tag{3.11}$$

Note that, depending on $\theta_{1/2-out}$ and $\theta_{1/2-in}$ the emitted beams from Txs 1 and 2 may not overlap, which in that case the coverage length is $2L_2 = 2L_{s-hor}\left(\tan\theta_{1/2-in} + \tan\theta_{1/2-out}\right)$. Using (3.11), the half power angle (assuming $\theta_{1/2-out} = \theta_{1/2-in}$) as a function of the field of view (FOV) for a range of link spans is shown in Figure 3.7, which displays a logarithmic increase of the Tx's half power angle with L_{FOV} reaching saturation points at ~220 and ~370 m for L_{s-hor} of 30 and 50 m, respectively.

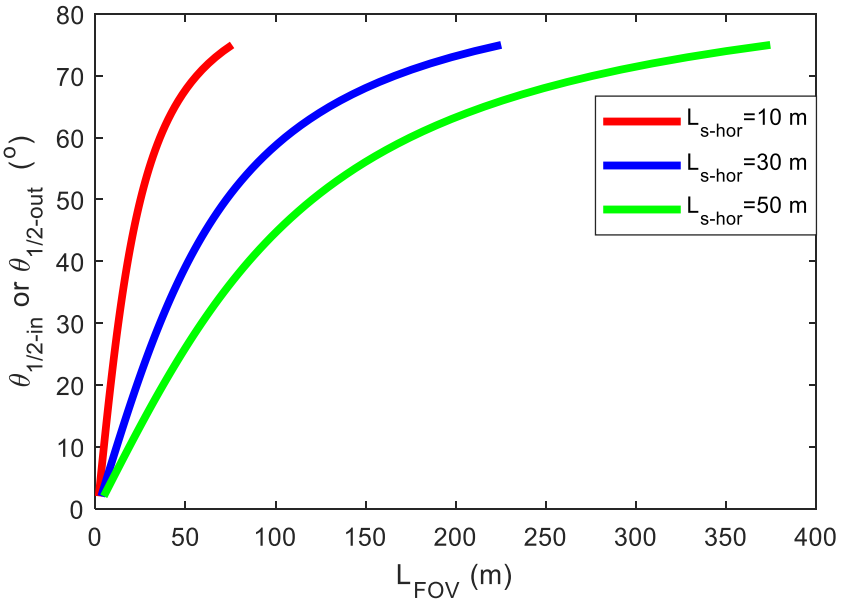

Figure 3.7: Half power angle of Tx versus L_{FOV} for a range of $L_{\mathrm{s-hor}}$

3.3 Performance Evaluation of Vehicular VLC with TLs-based Txs

Comprehensive performance evaluation of the use of HLs as Txs for data transmission with the given real beam patterns of different vehicle brands was reported in [95]. The results revealed that, the received power level improved with the decreasing Rx's heights from the ground. This is because, HLs are being designed for road illumination and therefore points down-ward on the road surface as shown in Figure 3.8. Therefore, this imposes the upper bound on the maximum transmission distance due to the angular inclination of the light beams on the road surface and its asymmetrical beam pattern. Notably, most works reported on the use of TLs as the Txs, are based on investigations with the use of a single TL, which only defines half the story, therefore, narrowing the conclusions drawn from the results obtained for the

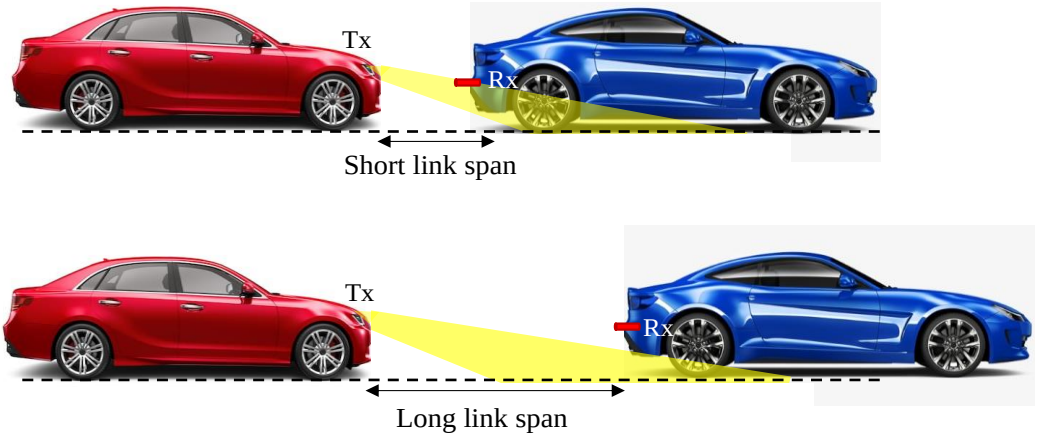

Figure 3.8: Vehicular VLC links using HLs as the Txs

specific vehicle type/light model. No works have been reported on vehicular VLC with different TL units at the time of this investigation. Therefore, to carry out performance evaluation of vehicular VLC using TLs for data transmission, we characterise four LED-based vehicle TLs of different vehicle modules.

3.3.1 Radiation patterns of the TLs

First, the radiation patterns of the TLs are measured, which defines the spatial intensity distribution of the emitted light from the TLs, which is important for the analysis of signal distribution and the coverage area is carried out. For this, a digital optical power meter (Thorlabs PM100D with a PD power sensor S120VC) is used to measure the received power levels over a reasonable fixed transmission distance of 1 m for a range of irradiance angle (i.e., -90^{o} (left) to +90^{o} (right)) of the TLs. For comparison, TLs from four popular vehicle brands namely: Audi A5 S5 N/S LED left outer TL facelift (Audi TL), BMW F30 right side outer LED O/S TL (BMW TL), Nissan Qashqai right side tailgate boot lid TL 26550 4EA0A model (Nissan TL) and Truck-DACA08712AM TL (Truck TL) are employed. Note that, for radiation pattern measurements, two broad measurement zones are possible: the far field and near field zones. The far-field zone corresponds to a distance from the light source of at least five

times (or more) of the largest dimension of the light source, while the near field zone corresponds to that below the far field zone [116]. Note, in the far field region the measured radiant/luminous intensity is practically independent on the measuring distance from the light source. The illuminated surface, radiation patterns (half power angle) and the estimated P_T of the TLs characterised are outlined in Table 3.2. As shown in Table 3.2, the half power angle ($\theta_{1/2-\text{out}}$ and $\theta_{1/2-\text{in}}$ i.e., the outer and inner half power angles, respectively as illustrated in Figure 3.6) varies within the range of 10^o to 75^o, with the highest and lowest number for the BMW and Truck, respectively, which corresponds to the wide and narrow radiation pattern as depicted in two-dimensional (2D) polar plots in Figure 3.9.

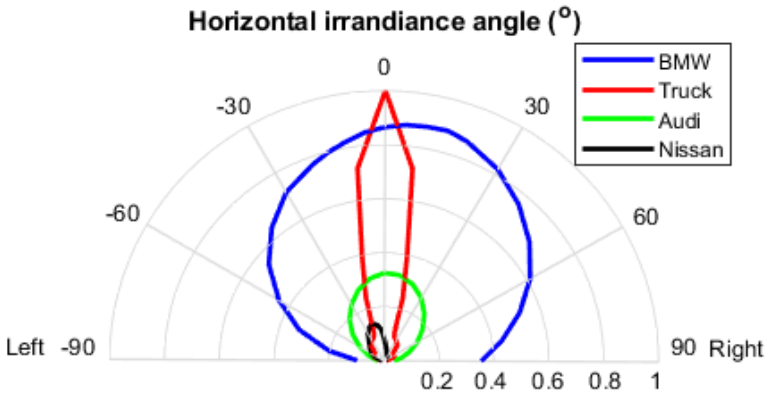

Figure 3.9: 2D polar plots of the normalized radiation pattern of TLs from experimental measurements

Table 3.2: TL parameters from empirical measurements

TL	$\theta_{1/2-\text{in}}$ **(°)**	$\theta_{1/2-\text{out}}$ **(°)**	**Illuminated area (cm^2)**	P_T **(mW)**
BMW	75	65	124.7	110.5
Audi	55	47	46.2	39.7
Truck	10	10	80.0	32.4
Nissan	27	22	38.2	9.4

3.3.2 Link power budget analysis

As part of the system design and implementation, a link power budget analysis for vehicular VLC using the four TLs units is carried out. For this, it is necessary to know the allowed inter-vehicle distances D_v for safe driving. Typically, a "two seconds" rule is recommended for D_v, whereby a driver maintains a minimum of two seconds behind the vehicle in front under the good weather condition, which is doubled to four seconds in bad weather conditions [61] as depicted in Figure 3.10.

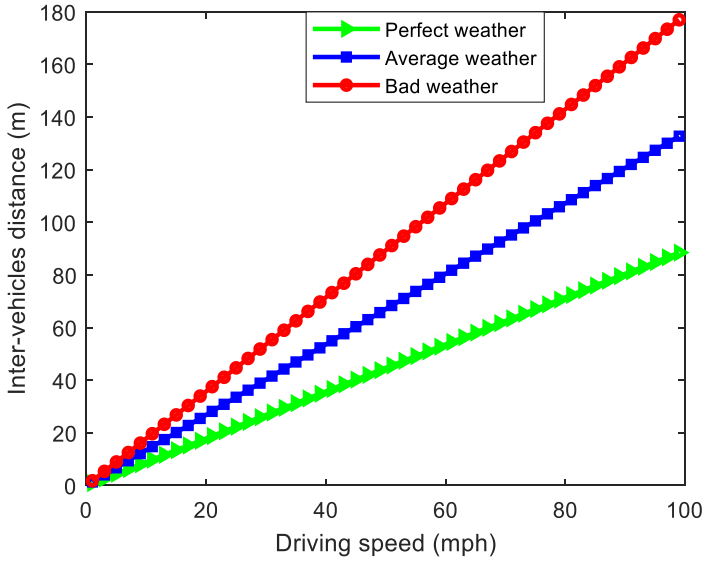

Figure 3.10: The inter-vehicle distance as a function of driving speeds using the 2 seconds driving rule

For a given P_T, the receiver power is given as:

$$P_r(\text{dBm}) = H_{\text{LOS}}(\text{dB}) + P_T(\text{dBm}) - L_{\text{sm}}(\text{dB}), \qquad (3.12)$$

where L_{sm} is the link safety margin, and H_{LOS} is the channel DC gain for the LOS, which is given by:

$$H_{\text{LOS}}(\text{dB}) = 10\log_{10}(A_{\text{PD}}g(\varphi_{\text{hor}},\varphi_{\text{ver}})T_s(\varphi_{\text{hor}},\varphi_{\text{ver}})R_{\text{Tx}}(\theta_{\text{hor}},\theta_{\text{ver}})/{D_v}^2), \qquad (3.13)$$

The key parameters used for the link power budget analysis are shown in Table 3.3. The received power (in dBm) per Tx as a function of the vehicles' speed for a range of irradiance angle $[\theta_{\text{hor}}, \theta_{\text{ver}}]$ of $[0^{\text{o}}, 0^{\text{o}}]$ to $[20^{\text{o}}, 0^{\text{o}}]$ (left of the TL's beam axis), for the case with no OC at the Rx is shown in Figure 3.11. It is revealed in Figure 3.11 that for the BMW TL, the maximum driving speed is 6.4 mph (i.e., D_v = 5.7 m) for $[\theta_{\text{hor}}, \theta_{\text{ver}}]$= $[0^{\text{o}}, 0^{\text{o}}]$ and P_r of -36 dBm (i.e., for a Rx sensitivity of -36 dBm), while for the Truck TL there is a steep decrease in the achievable driving speeds from 3.6 to 1.2 mph as $[\theta_{\text{hor}}, \theta_{\text{ver}}]$ increases from $[0^{\text{o}}, 0^{\text{o}}]$ to $[20^{\text{o}}, 0^{\text{o}}]$ due to its narrower radiation pattern. Note that, the Rx sensitivity of -36 dBm is a typical value chosen, which satisfies high speed links up to data rates of 10 Gbps at a BER <10^{-6} considering a PIN PD [117]. A summary of the achievable D_v and driving speeds for the TLs under investigation are given in Table 3.4. Note, these attainable speeds are far below the typical recommended

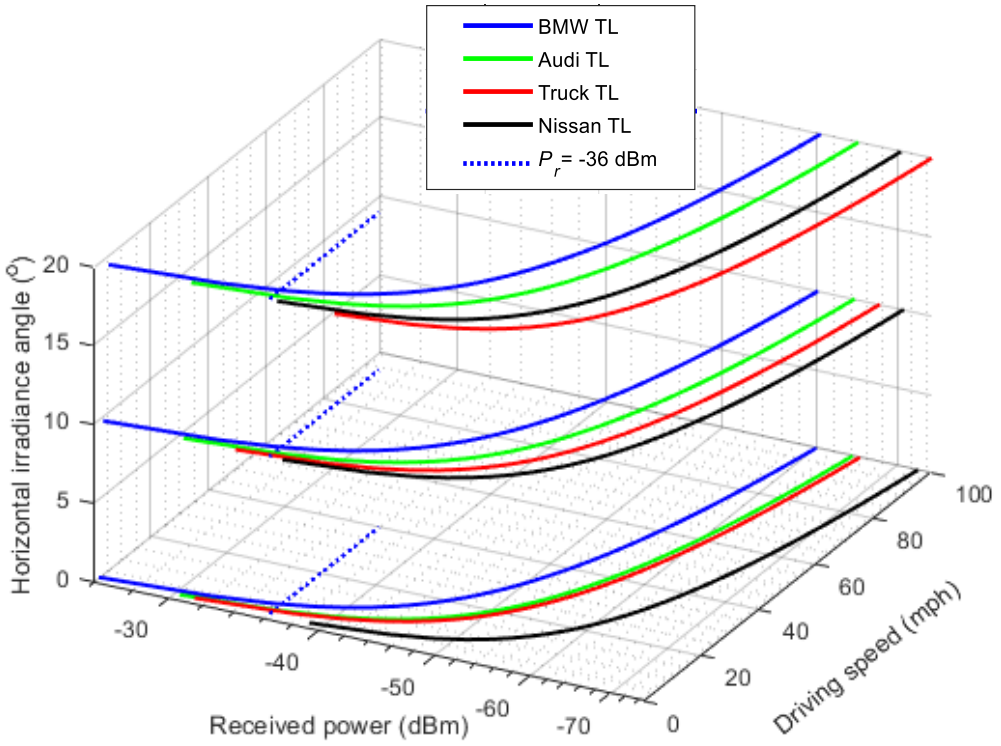

Figure 3.11: The horizontal irradiance angle as a function of the received power and driving speed for different TLs

vehicle's speed limits, e.g., for cars, vans, motorcycle or buses a driving speed of 30, 60, 70, and 70 mph is approved in built-up areas, single carriage ways, motorways and dual carriage way, respectively [118].

Figure 3.12 shows the predicted required P_T as a function of the driving speed for cases without and with an OC at the Rx. Note, the predicted required P_T over the driving speeds decreases by 5.3, 8.1, and 11.2 dBm when a NIOC with the diameter D of 25.4, 35, and 50 mm are utilized at the PD, respectively.

Table 3.3: Key parameters of the link power budget analysis

Parameter	**Symbol**	**Value**
Link safety margin	L_{sm}	3 dB
Surface area of PD	A_{PD}	1.5 cm^2
TL transmit power	P_T	9.4-110.5 mW
Irradiance angle	$[\theta_{\mathrm{hor}}, \theta_{\mathrm{ver}}]$	$[0^{\mathrm{o}}, 0^{\mathrm{o}}]$- $[20^{\mathrm{o}}, 0^{\mathrm{o}}]$
Inter-vehicle distance	D_v	1- ~90 m
Diameter of NIOC	D	25.4 -50.0 mm
Vehicle speed	S	~1-100 mph
Gain of optical filter	$T_s(\varphi_{\mathrm{hor},}\, \varphi_{\mathrm{ver}})$	1

Table 3.4: Summary of achievable inter-vehicle distances and driving speeds as $[\theta_{\mathrm{hor}}, \theta_{\mathrm{ver}}]$ increases from $[0^{\mathrm{o}}, 0^{\mathrm{o}}]$ to $[20^{\mathrm{o}}, 0^{\mathrm{o}}]$

TL type	$[\boldsymbol{\theta_{\mathrm{hor}}, \theta_{\mathrm{ver}}}] = [\mathbf{0^{o}, 0^{o}}]$		$[\boldsymbol{\theta_{\mathrm{hor}}, \theta_{\mathrm{ver}}}] = [\mathbf{20^{o}, 0^{o}}]$	
	Speed (mph)	$\boldsymbol{D_v}$ **(m)**	**Speed (mph)**	$\boldsymbol{D_v}$ **(m)**
BMW	6.4	5.7	6.2	5.5
Audi	4.0	3.6	3.7	3.3
Truck	3.6	3.2	1.2	1.1
Nissan	1.7	1.5	2.2	2.0

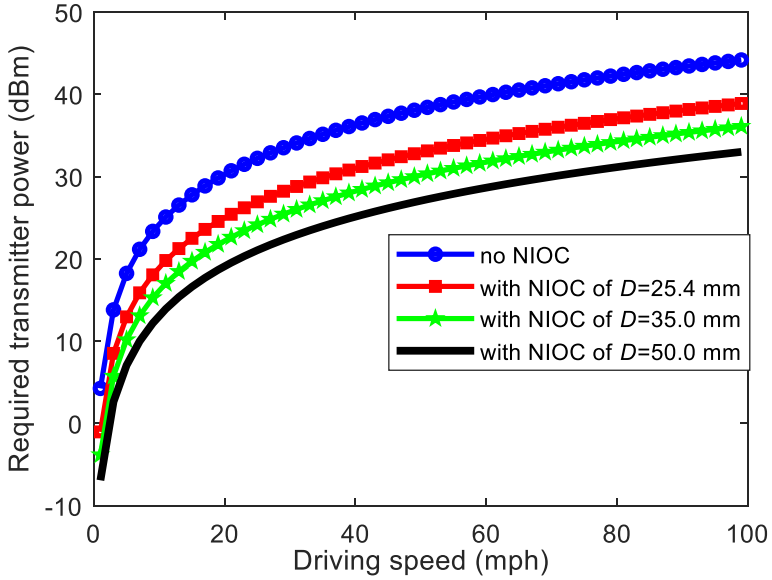

Figure 3.12: The predicted required transmit power as a function of the driving speed with and without a NIOC

3.4 Noise Analysis for Vehicular IR/VLC Systems with PD-based Rxs

3.4.1 Ambient noise

In vehicular VLC, there are two major ambient light induced noise sources of (*i*) streetlights mostly at night, other vehicle lights and advertising boards; and (*ii*) the background solar radiation (sunlight), which is the main noise source during daytime. It is noteworthy that, the solar irradiance $P_{\text{solar}}(\lambda)$ varies by the time of the day and latitude, i.e., the position of the Sun. Moreover, its effect on the performance of vehicular IR/VLC system will also depend on the orientation and cardinal direction of the Rx. The photocurrent generated at the PD due to $P_{\text{solar}}(\lambda)$ is given as:

$$I_{\text{solar}} = A_{\text{PD}} g(\varphi_{\text{sun}}) \cos(\varphi_{\text{sun}}) G_{\text{PD}} \int_{\lambda_1}^{\lambda_n} P_{\text{solar}}(\lambda)\, T_f(\lambda)) \mathcal{R}(\lambda) d\lambda, \qquad (3.14)$$

where G_{PD} is the gain of the PD, φ_{sun} is the difference in the orientation angle between that of the measured $P_{\text{solar}}(\lambda)$ and the PD, λ_1 and λ_n are the integration limits, i.e., the wavelength band, where 810-890 nm and 405-690 nm are considered in this work for the IR and visible-based systems, respectively. The OC's gain is represented as $g(\varphi_{\text{sun}})$, $\mathcal{R}(\lambda)$ is the responsivity of the PD and $T_f(\lambda)$ is the transmittance of the optical band pass filter. Note that, the daytime background radiation-induced shot noise is the dominant source in vehicular VLC, which can be expressed as [119-120]:

$$\sigma_{\text{amb}}^2 = 2 q_e I_{\text{solar}} B, \qquad (3.15)$$

where q_e is the electron charge, and B is the system bandwidth.

3.4.2 Thermal and shot noise sources

Thermal noise is generated due to the random motion of charge carriers [77] and its variance is given as [120,121]:

$$\sigma_{\text{thermal}}^2 = \frac{4 k_b T_K B}{R_L}, \qquad (3.16)$$

where k_b is Boltzmann's constant, T_K is the absolute temperature in Kelvin, and R_L is the load resistance.

Notably, the photodetection process is discrete in nature and results in the signal-dependent shot noise at the PD [117,122], with the variance given as [117]:

$$\sigma_{\text{shot-rs}}^2 = 2 q_e \mathcal{R}(\lambda) P_r B. \qquad (3.17)$$

In addition, the PD's dark current noise variance is given as [120]:

$$\sigma_{\mathrm{dk}}^2 = 2q_e I_{\mathrm{dk}} B, \tag{3.18}$$

where I_{dk} is the dark current.

The total noise variance is then given as:

$$\sigma_T^2 = \sigma_{\mathrm{amb}}^2 + \sigma_{\mathrm{thermal}}^2 + \sigma_{\mathrm{shot-rs}}^2 + \sigma_{\mathrm{dk}}^2. \tag{3.19}$$

3.4.3 Performance evaluation metrics

Intensity modulation direct detection (IM/DD) is a widely adopted cost-effective scheme in optical fibre and OWC systems, where the intensity of the emitted light from the Tx is used to convey the information bits. Consequently, in the direct detection scheme, no local oscillator is required [123]. Note, in this thesis, IM/DD scheme with on off keying (OOK) (because of its simplicity) and a PD based Rx (Hamamatsu S6968) was adopted. The received optical power is calculated (i.e., considering a single Tx) and the noise variances ambient, thermal, signal, and dark current shot noises are obtained using (3.12), (3.14) - (3.18). Notably, the system's bandwidth is determined primarily by the low pass filter characteristic of the Rx, which can be expressed as $B = R_b/2$, where R_b is the data rate [121]. Thus, for the additive white Gaussian noise channel, the SNR at the Rx is given by [84]:

$$\mathrm{SNR} = \frac{(\mathcal{R}(\lambda)P_r)^2}{\sigma_T^2}. \tag{3.20}$$

Thus, the BER is then given as [84]:

$$\mathrm{BER} = Q\left(\sqrt{\mathrm{SNR}}\right), \tag{3.21}$$

where $Q(x)$ is the Q-function used for the computation of the tail probability of the standard Gaussian distribution given by [84]:

$$Q(x) = \frac{1}{\sqrt{2\pi}} \int_{x}^{\infty} e^{\frac{-y^2}{2}} dy. \quad (3.22)$$

3.5 Performance Analysis of the Proposed IR Light Communications System

An array of IR-LED (Osram SFH 4715AS) is used with a symmetrical beam pattern and no angular inclination towards the road surface as the vehicle IR-light Txs in order to meet the driving speed (i.e., typical inter-vehicle distances) requirements. First, the received power per Tx over driving speeds for a range of D by numerical simulations using (3.12) and (3.13) is shown. Note, (*i*) only LOS is considered since the Tx is a symmetrical light source with no angular inclination towards the road, thus with no significant reflections from the road surface; and (*ii*) the transmit optical power level must meet the IEC 62471/2006 emission limits for eye safety, which specifies emission limit of 100 W/m^2 [124], whereas the proposed system in this work has a maximum of 5.92 W/m^2 (for the two front/rear Txs) at a 1 m distance from the Txs (considering that D_v would not be less than 1 m). Table 3.5 outlines the key system parameters employed.

Table 3.5: Key system parameters

Parameter	**Symbol**	**Value**
Active area of PD (Rx)	A_{PD}	1.5 cm^2
Peak wavelength of LED	λ	860 nm
Inter-vehicle distance	D_v	1- ~90 m
Absolute temperature	T_K	298 K
System bandwidth	B	1-5 MHz
Responsivity of PD at 850nm & 640 nm (i.e., for IR-LED & BMW TL, respectively)	$\mathcal{R}(\lambda)$	0.63 & 0.44 A/W
Solar irradiance	$P_{\mathrm{solar}}(\lambda)$	413.77 $\mathrm{W/m}^2$
Load resistance	R_L	50 Ohms
Maximum PD dark current	I_{dk}	5 nA
Transmission coefficient of filter	$T_f(\lambda)$	1
Vehicle speed		2- 100 mph
Half power angle of IR-LED		$\pm 45^{\mathrm{o}}$
Transmit power per IR-LED		1.34 W
Number of LEDs per Tx		7
PD model (Hamamatsu (Si PIN))		S6968
LED model (Osram)		SFH 4715AS
IR bandpass filter model (Thorlabs)		FB850-40
Visible bandpass filter (MidOpt)		BP550

Importantly, ensuring link robustness under strong ambient light is the greatest challenge in vehicular VLC systems. Therefore, an IR based light communications link is proposed to mitigate this challenge for the following reasons: (*i*) Solar irradiance in the IR band is much lower than the visible band, which results in the improved SNR performance. For example, from Figure 3.13 (data source from [125]), in the IR region at the wavelength of 850 nm, the solar irradiance is 50 % less in comparison to the

wavelength of 480 nm in the visible light region; and (*ii*) the integration of IR-LEDs will help to meet the required transmit power level (within safety limits) needed for longer distance transmissions, where the TLs would not be able to offer, as demonstrated in Section 3.3. It is worth noting that, the high or low beam HLs, which have higher transmit powers than TLs are only used at night or when the visibility is low due to heavy rain, fog, snow etc., thus imposing limitation in vehicular VLC systems. The proposed work overcomes these limitations and issues by introducing the utilization of IR-LEDs in addition to TLs and HLs, to always ensure link availability and be on when data is being transmitted unnoticeable to the human eyes. In addition, there are other merits of IR-LEDs such as (*i*) higher electrical-to-optical conversion efficiency than the visible blue LED-based white light sources [126]; and (*ii*) the 3 dB bandwidth of IR-LEDs are higher than the white LEDs, which is well known [126].

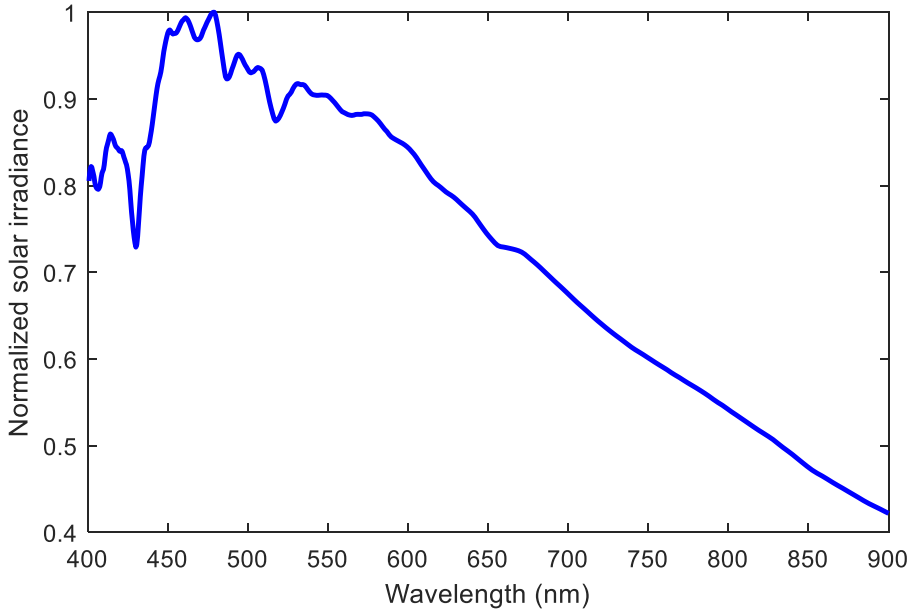

Figure 3.13: Normalized solar irradiance as a function of wavelength

Figure 3.14 shows the plots of the received power as a function of the driving speed for the case without and with an OC at the Rx. It can be noticed that the received

power decreases and increases with the driving speed and D, respectively. For example, the driving speeds are ~100 and 60 mph at P_r of -36 dBm with a NIOC of $D = 25.4$ mm and without, respectively. Notably, the received power increases by 5.3, 8.1, and 11.2 dBm with the utilization of a NIOC with D of 25.4, 35, and 50 mm, respectively.

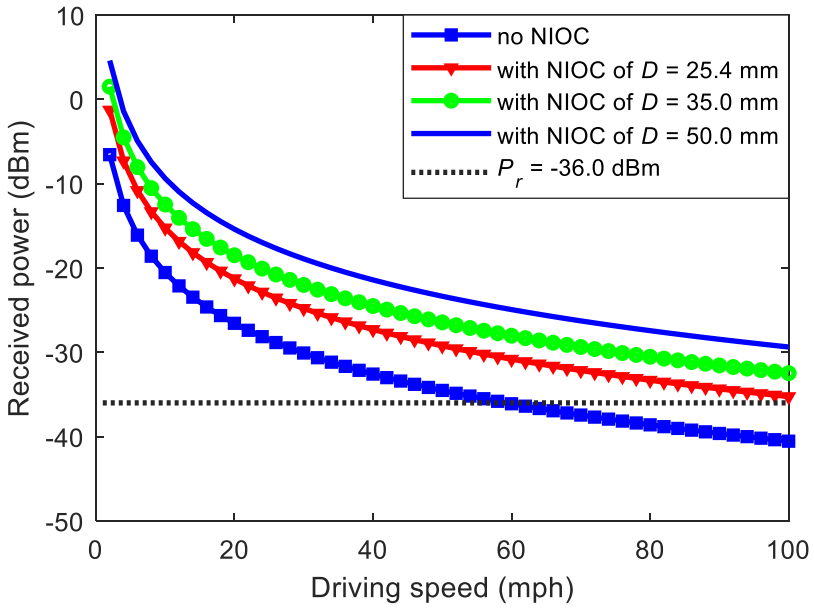

Figure 3.14: Received power as a function of the driving speeds with and without a NIOC at the Rx

Figure 3.15 depicts the predicted BER performance versus the driving speed for the proposed IR light communications system using IR-LEDs and the BMW TL (chosen because it has the highest P_T among the four TLs characterized) for a range of data rates via numerical simulations using (3.14) - (3.22). Here we have considered NIOC with D of 25.4 mm, P_{solar} of 413.77 W/m^2 and a narrow bandpass filter (Thorlabs FB850-40) at the Rx. A solar power meter (ISO-TECH ISM410) was used to measure the solar irradiances (wavelength range of 400-1100 nm) at the various positions with respect to the Sun. $P_{\text{solar}}(\lambda)$ for the direction with the highest average value (measured on a Sunny day at Blakelaw in the city of Newcastle, UK, N 54°59’44’’ W 1°39’52’’ in April 2020)

is utilised in the simulations. Note, the $P_{\text{solar}}(\lambda)$ value over the IR and visible wavelength ranges mentioned in Section 3.4.1 is obtained from the empirical measurement value using (3.14) with respect to the wavelength solar irradiance distribution data from [125]. Note, the Rx is located on the receiving vehicle, such that it points towards vehicles on the road with no vertical or horizontal tilting angle.

As can be seen from Figure 3.15, the BMW TL does not meet typical driving speeds limits (i.e., inter-vehicle link spans) due to low P_T. Note, only driving speeds of 5, ~6, and 7 mph (translating to a L_S of 4.5, 5.4, and 6.3 m, respectively) are attainable at R_b of 10, 6, and 2 Mbps, respectively, at the FEC BER limit of 3.8 $\times 10^{-3}$. Nevertheless, the proposed system with the IR-LEDs offers driving speeds of 70, 80, and >100 mph (translating to a L_S 63, 72 and >89 m) at R_b of 10, 6, and 2 Mbps, respectively under the same conditions and a high ambient light level. Note, a steep increase in the BER with respect to the driving speed up to ~ 90, ~70, and ~60 mph for the links with R_b of 2, 6 and 10 Mbps, respectively. For example, at R_b of 10 Mbps the BER values are 8.0×10^{-8} and 3.8×10^{-3} for the driving speed of 50 and ~70 mph, respectively. This is because, the received power level reduced by ~50 % (i.e., to 0.6 µW (-32.2 dBm) from 1.2 µW (-29.2 dBm) due to the increase in the driving speed, translating to the increased link span i.e., inter-vehicle distance).

Besides, to show the impact of the sunlight noise on the link performance, the BER for BMW TL and the proposed IR light communications system are investigated by considering all noise sources as in (3.19) without the (*i*) signal dependent shot noise $\sigma^2_{\text{shot}-\text{rs}}$; and (*ii*) sunlight noise σ^2_{amb}; as depicted in Figure 3.15. For example, for the proposed IR light communications system, the BER at a driving speed of 90 mph with and without σ^2_{amb} are 5.3 $\times 10^{-2}$ and 5.5 $\times$ 10^{-9}, respectively. For the link using BMW

TL, the BER at the speed of 8 mph with and without σ^2_{amb} are 1.7 $\times 10^{-1}$ and 1.3 $\times 10^{-9}$, respectively, showing the high degrading impact of the sunlight induced shot noise on the performance of the vehicular links. As illustrated in Figure 3.15, $\sigma^2_{\text{shot-rs}}$ has insignificant impact on the BER performance in comparison to σ^2_{amb}.

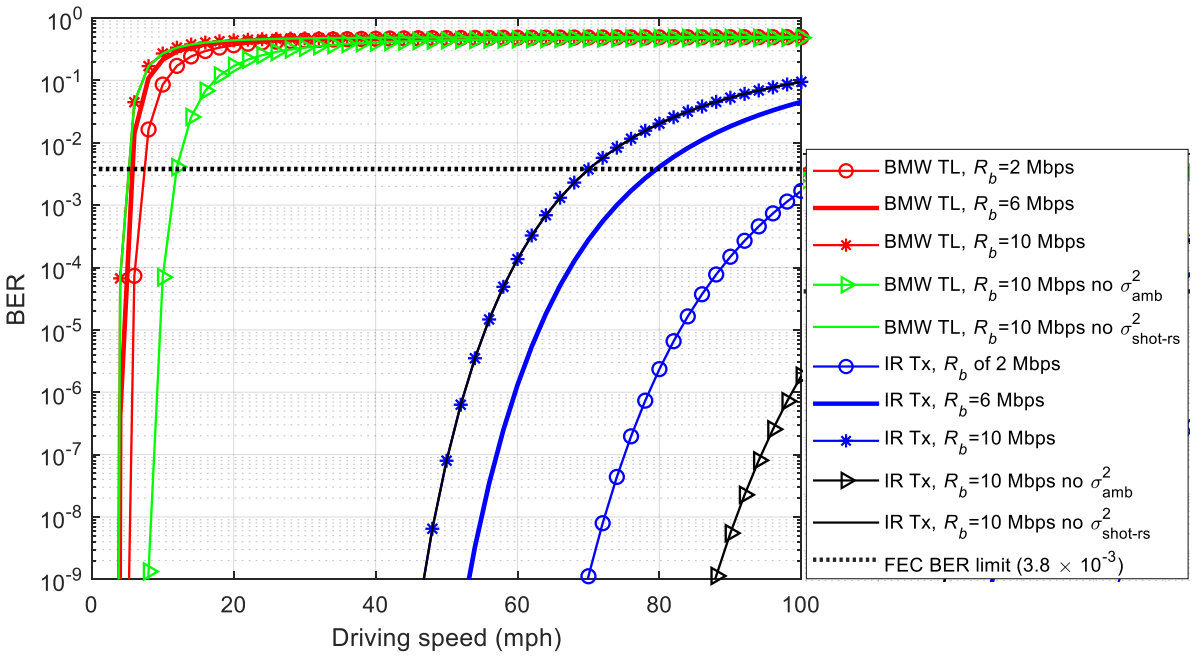

Figure 3.15: The BER performance against the driving speed for a range of R_b for the proposed vehicular IR light communications system

3.6 Summary

A performance evaluation study was conducted on the use of various vehicle TLs as Txs for vehicular VLC systems. The findings revealed that the radiation characteristics and P_T for different vehicle TLs are not the same, which impacts the coverage area, communication distance and signal distribution, which are important factors in the practical implementation of vehicular VLC as part of ITS. Furthermore,

the characterised TLs all fell short of typical communication distances in vehicular environments, consequently the incorporation of IR-LEDs in vehicle HLs and TLs to meet the typical communication link spans required in vehicular environments. It was shown that the proposed IR light communications system outperforms the visible light-based TLs, particularly in the presence of sunlight. It was demonstrated that the proposed IR light communications could achieve transmission distances of 63, 72, and >89 m at the target FEC BER limit of 3.8×10^{-3}, compared to 4.5, 5.4, and 6.3 m for the BMW vehicle-based TL at data rates of 10, 6, and 2 Mbps, respectively under realistic ambient light conditions. Furthermore, since both the front and rear vehicle's Txs will have the same P_T and radiation characteristics, the proposed scheme addresses the link asymmetry highlighted in literature and discussed in Section 2.4.2. Furthermore, based on the road lane width and the locations of the Txs and Rxs on vehicles, the maximum HS-AFOV and VS-AFOV needed for vehicles travelling on the same lane are analysed and insights were also provided for the required AFOV's for communication of vehicles on other lanes (with an imaging-based OC at the Rx).

CHAPTER 4
LONG DISTANCE ROLLING SHUTTER-BASED OCC FOR ITS

4.1 Introduction

While relaying is vital to extend the transmission range and to rebroadcast required messages to following vehicles, the link span i.e., the achievable range with a single hop must be maximized as much as possible. Thus, this chapter shows how a RS-based OCC link distance can be extended as Chapter 3 dealt with extending the communication link for the PD-based links only. Consequently, a new technique is developed to increase the link-span of the RS-based OCC that could be used in many IoT applications including vehicular communications. Firstly, in this chapter, an overview of the merits of long-range OCC and related works are discussed. The theory, system model, image processing and detection of the proposed scheme are given. Simulation results are also shown to illustrate the achievable number of data rows i.e., the data rate using this scheme. Moreover, the setup for the experimental demonstration of the proposed scheme and the results obtained are presented while a summary of the work done is given lastly.

4.2 Overview

A pragmatic form of VLC is OCC, which makes use of IS (i.e., cameras) as the Rx while LEDs, liquid crystal displays, and laser diodes can be employed as Txs [127-131]. In VLC-OCC, a two-dimensional data is captured in the form of image sequences, which enables transmission of multi-dimensional data over the free space channel. VLC-OCC offer data communications, localization, pattern and object recognition, motion detection, vision, etc. These can be used in several applications including all-optical IoT (OIoT) [132-137]. OIoT-based applications include V2X, device-to-device communications, mobile atto-cells [138-141], which uses the optical band rather than the congested RF spectrum that can be utilised in the most needed areas. The current high interest in the internet of vehicles (IoV) is as a result of the inspiration by IoT [142]. Moreover, the ubiquitous increase in both the use of cameras (such as dashcams, vehicle rear view cameras, speed cameras, security surveillance cameras and traffic cameras) and LEDs in roadside units and vehicles (e.g., TLs and HLs) opens potential opportunities for the implementation of VLC-OCC as part of ITS to aid traffic and therefore improve the quality of life.

One of the merits of a camera-based Rx over a single PD-based Rx is the higher SNR due to the camera's analogue gain feature, exposure times T_{exp} feature, and larger overall photosensitive area. Notably, optical wireless systems (infrared and visible bands) utilizing camera-based Rxs offer relatively lower data rates R_b compared with the high-speed PD-based Rxs, due to the limited capture frame rates of most commercial cameras. However, low R_b feature of VLC-OCC should not be seen as a problem considering that, there are many applications including vehicular communications [142-147], indoor IoT [148], localization [149-151], advertising [152], sensor network [153],

motion capturing [154-156], etc., where low R_b is sufficient. Importantly, in OCC, each camera pixel can detect signals at distinct wavelengths over the visible range, e.g., red, green, and blue (RGB), thus offering parallel detection capabilities (i.e., massive multiple-input multiple-output (MIMO) together with multi-array LEDs) [157-162], and an adaptive field of view feature. Recently, even an enhanced R_b using MIMO is demonstrated, where a linear increase in data throughput is achievable with the increase in the number of LEDs [162] and artificial neural network-based equalizers, e.g., providing an improved bandwidth of up to 2-9 times more, depending on the T_{exp} [163-165] were shown. Furthermore, the light beams carrying information emerging from different Txs and different directions via the LOS [166-168], non-LOS [169-170], and/or both paths can be captured using the camera-based Rxs.

In OCC, R_b can be increased to be higher than the frame rate R_f of the camera. This is made possible using the complementary metal-oxide-semiconductor (CMOS) RS-based cameras, which sequentially (i.e., row-by-row) integrates incoming light illuminating the camera pixels [171]. However, this technique offers reduced transmission range and is more critical in long range outdoor OCC links. Consequently, the focus of this research is to extend the communications distance of RS-based OCC links. Notably, several research works have been reported on long distance communications such as [172], where a 100 m link span was demonstrated using a RGB LED at a R_b of 25 bps for each colour channel. In [173], a 120 m link span was reported at a high BER of $>10^{-2}$ but the achieved R_b was not disclosed at this link span. However, an achieved maximum R_b of 200 bps at 4 m link span was reported. In [174], a 160 m OCC link was experimentally demonstrated at R_b of 50 bps with a BER of 1.7×10^{-3} for the distance critical applications. In [175], R_b of 15 bps over a link range of 328 m was presented using the global shutter (GS) capturing technique for smart city

applications such as environmental pollution monitoring with ~96 % reception success rate. Notably, to establish long link spans in OCC, generally large area light sources have been used such as 48 × 48 and 60 × 90 cm^2 in [175] and [172], respectively, which are impractical in vehicular communications where the HLs and TLs are not relatively large and differ from one vehicle brand, model and size to the other.

Notably, in this research work, a novel reception technique is proposed to increase the transmission link span of RS-based OCC. This is made possible by reducing the camera's spatial bandwidth in the out-of-focus areas, i.e., by means of defocusing the camera. This technique enables capturing of a larger footprint of the light source using the IS without utilising large area Txs and reducing the AFOV of the system. Moreover, a detection algorithm to efficiently extract the received information from captured video frames is proposed and developed. Cameras in the focused mode have mainly been utilized in previous reported works on OCC. However, cameras in the defocused mode can equally be used, depending on the applications, for example V2I [10], and indoor non-LOS (NLOS) VLC systems [176,177]. For experimental demonstration of the proposed scheme, in this work, the Tx employed has a very small surface area of 2.5 x 2.5 cm^2, which is 19 times smaller than the source used in [175]. Moreover, a communication link span of up to 400 m with a 100% success rate in data transmission is demonstrated as proof of concept with ~32 bits/frame translating to R_b of 800 and 1920 bps for the camera frame rates of 25 and 60 fps, respectively. Note that, this R_b is sufficient for transmission of short (traffic) messages [162]. The demonstrated system is the longest link-span achieved for a RS-based OCC link, which can be used in other distance critical applications with relatively low R_b requirements.

4.3 Theory, System Model and Detection

The Rx adopted in this research work is the CMOS camera, which uses the RS readout method in which each pixel row is exposed in a row-by-row sequential manner having a fixed time delay (i.e., a row readout time T_r) as depicted in Figure 4.1. Besides, the readout of each row takes place after the row's exposure in RS cameras (i.e., T_r comes after T_{exp}). Note, in cameras, the three main parameters that control the picture's brightness level are the T_{exp}, ISO or gain depending on the camera brand/type, and the aperture. ISO is defined as the ratio of the output signal of the IS to the exposure level, which is the product of illuminance and T_{exp}. The aperture controls the amount of light coming through the lens system of the IS, and the diameter of the aperture $D_{\text{lens}} = f/f_{\text{stop}}$, where f_{stop} represents the focal stop number of the lens aperture. Prior to exposing the IS to the light, each pixel must be reset within the resetting duration T_{rest}, which is mainly determined by the parasitic capacitance of the IS. Therefore, within the time interval between when the pixel is reset and when it is ready to be read-out (also known as T_{exp}), the IS is exposed to the light and the read-out circuit at time $t = aT_{\text{fr}} + T_{\text{rest}} + T_{\text{exp}}$ reads and samples the signal, where T_{fr} is the frame duration and a is an arbitrary constant [177].

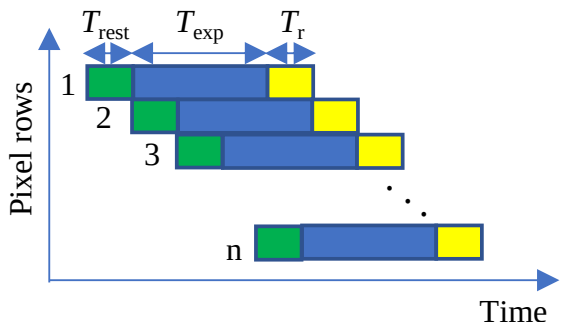

Figure 4.1: Row by row scanning of a CMOS RS camera

The advantages of using CMOS over charged coupled devices cameras are lower power consumption, faster readout, more programmability, and low cost. Note, in very fast movements, RS cameras present a distorted shape of the object in the image, which is unpleasant for photography purposes. Also, the exposure of each pixel's row does not commence at the same time in RS cameras i.e., it does not happen all together at once as in GS-based cameras, hence an advantage in OCC systems, i.e., $R_b > R_f$, can be achieved, but at the cost of reduced communications range. In addition, the RS-OCC technique offer a flicker free transmission.

For camera-based VLC systems, the standard IS-based Rxs are modelled as a linear shift-invariant system. Thus, the voltage at a pixel, corresponding to a single PD is given as [178]:

$$V_R(t) = \frac{g}{C_{\mathrm{PD}}} \int_{t-T_{\mathrm{exp}}}^{t} \mathcal{R}\, x(t)\mathrm{d}t, \tag{4.1}$$

where g is the gain, C_{PD}, $\mathcal{R}$, and $x(t)$ are the equivalent capacitance, PD's responsivity, and the received signal at a pixel at time *t*, respectively. The system response is given as [179]:

$$h(t) = \frac{g}{C_{\mathrm{PD}}}\left(u(t) - u\left(t - T_{\mathrm{exp}}\right)\right), \tag{4.2}$$

where $u(t)$ is the unit step function.

The integration of the input signal over T_{exp} leads to a finite impulse response low pass filter effect with the transfer function given as [179]:

$$H(f) = \mathcal{F}|h(t)| = \frac{gT_{\mathrm{exp}}}{C_{\mathrm{PD}}} \frac{\sin\left(\pi f T_{\mathrm{exp}}\right)}{\pi f T_{\mathrm{exp}}} e^{-j\pi f T_{\mathrm{exp}}}. \tag{4.3}$$

The DC gain is proportional to T_{exp}, and significantly affects the achievable maximum SNR [179].

Importantly, in OCC, the captured Tx's focused image size drops with the increase in link span as given by the relationship $d_{img} = d_{Tx}\, f / d_L$, where d_{Tx} and d_{img} are the diameters of the Tx and of the projected Tx's image on the IS at f, respectively. Here, RS-based OCC is poised with a limitation as there is decrease in obtainable received signal area on the IS of the camera as the link span increases. Note, the received signal area on the IS determines the number of rows N_{rows} (i.e., the ON and OFF states) achievable i.e., the R_b. Consequently, this limitation can be reduced by operating the camera in its out-of-focus (defocused) mode. A typical camera is composed of a complex lens system, optical low pass filters, an adjustable aperture, a micro lens array, an infrared cut filter, a colour filter-array and a sensor chip [177]. Figure 4.2 shows a lens, object and IS configuration. The IS can be moved from positions 1 to 2 where varying sizes of the projected object's image is obtainable. Essentially, a larger footprint of the Tx is obtained when the camera is defocused i.e., altering the distance between the lens and the IS, to allow the Tx's image to converge beyond the focal point thus creating a large footprint of the projected Tx image.

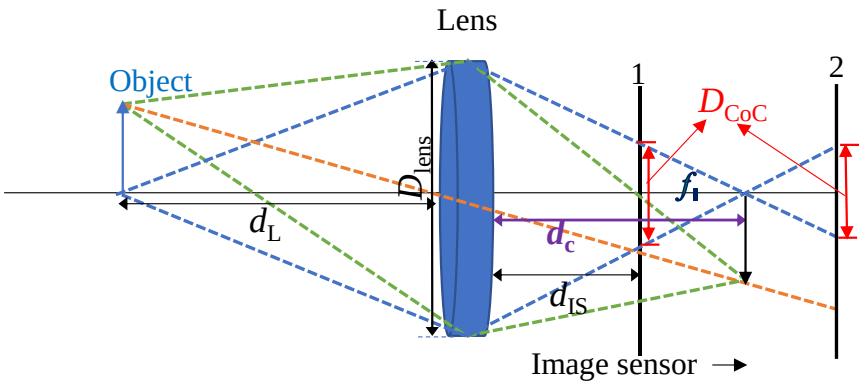

Figure 4.2: Example of lens, IS and object configuration

More number of data rows N_{rows} are visible i.e., detectable by the Rx (camera) as illustrated in Figure 4.3 for the defocused modes.

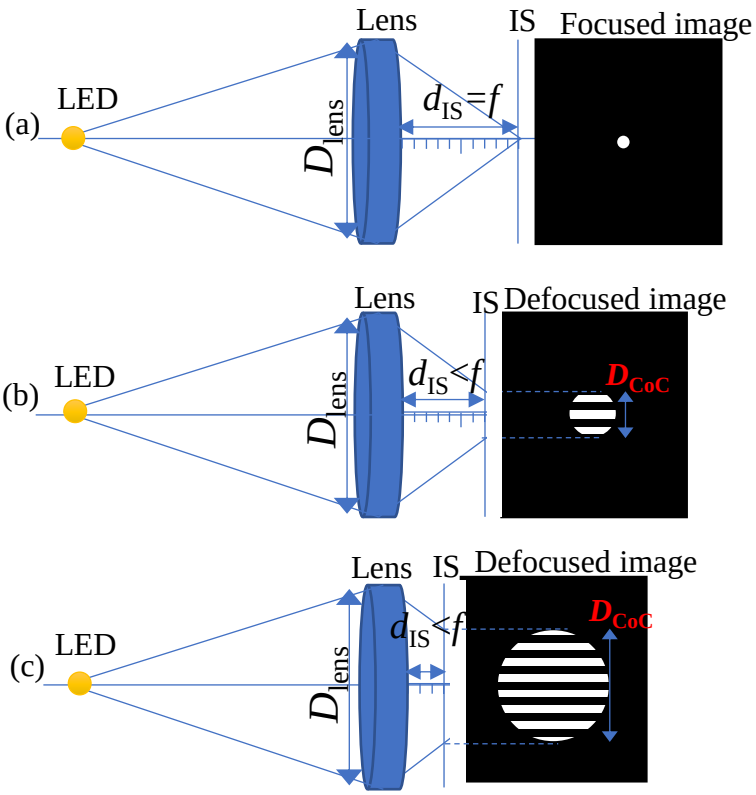

Figure 4.3: Illustration of the captured Tx images on the IS with different lens and IS configurations for the: (a) focused mode ($d_{IS} = f$), (b) defocused mode (for d_{IS} of 0.7), and (c) defocused mode (for d_{IS} of 0.3 f)

It is important to note that, defocusing of the camera results in a disc-shaped pattern known as the circle of confusion (CoC), which is convoluted with the image as given by [180]:

$$G_o(x,y) = G_i(x,y) \otimes\otimes G_{\mathrm{CoC}}(x,y), \qquad (4.5)$$

where $G_{\mathrm{i}}(x,y)$ and $G_{\mathrm{o}}(x,y)$ are the focused and defocused image intensity functions, respectively. $G_{\mathrm{CoC}}(x,y)$ is the CoC disc function, which is the same shape as the camera's lens aperture and $\otimes\otimes$ is the 2-dimensional convolution operator.

For a circular aperture, $G_{\mathrm{CoC}}(x,y)$ can be expressed as [180]:

$$G_{\mathrm{CoC}}(x,y) = U(\sqrt{x^2 + y^2}) - U(\sqrt{x^2 + y^2} - 0.5D_{\mathrm{CoC}}), \tag{4.6}$$

where $U(.)$ is Heaviside step function and D_{CoC} is the CoC's diameter, which is the same as the width of the defocused image of a point source and is expressed as [180]:

$$D_{\mathrm{CoC}} = \frac{D_{\mathrm{lens}}}{2d_c}|d_c - d_{\mathrm{IS}}|, \tag{4.7}$$

where the distance between the centre of the lens to the IS is denoted as d_{IS}, while d_c represents the distance between the centre of the lens and the image, which is given as [180]:

$$d_c = \frac{d_L f}{d_L - f}, \tag{4.8}$$

where d_L is the distance from the light source to the centre of the lens. It is worthy of note that, the size of CoC is dependent on the aperture diameter D_{lens} collecting light rays to be projected onto the IS. Therefore, to enhance the amount of defocusing achieved (i.e., D_{CoC}) to have the best signal area, $|d_c - d_{\mathrm{IS}}|$ must be maximised and lower values of f_{stop} should be used to obtain larger D_{lens}.

Illustrated in Figure 4.4 is N_{rows} (i.e., the number of data bits/symbols) as a function of the link distances for the focused and three different defocused capture modes for d_{IS} of f, 0.3 f, 0.5 f, and 0.7 f, $D_{\mathrm{lens}} = f/10$, f = 1 m, and the row widths of 0.05 cm. It can be observed that, N_{rows} increases with decreasing d_{IS}. For instance, at $d_L$of 30 m the number of bands increases from ~1 for the focused image mode to ~31, 50, and 70 for d_{IS} of 0.7 f, 0.5 f, and 0.3 f, respectively hence facilitating longer RS-OCC link spans. The width of one pixel row (representing one symbol or bit) w_b =

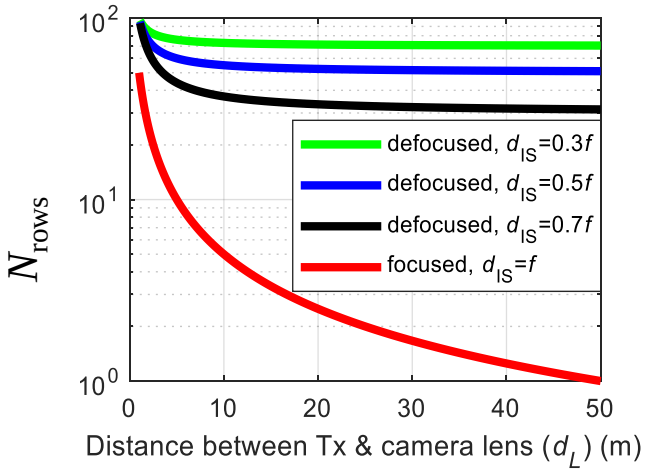

Figure 4.4: N_{rows} as a function of d_L for a range of d_{IS}

$1/(2f_{\text{Tx}}T_r)$, where f_{Tx} denotes the switching frequency of the Tx [181]. Note that, the increase in N_{rows} with defocusing is at the cost of reduced light intensity level per pixel (i.e., lower PSNR/pixel) because the received light spreads over higher numbers of pixels. Remarkably, the latter can be compensated for by increasing the analogue gain of the camera i.e., its sensitivity and T_{exp} (i.e., within the required bandwidth) to enable capturing more lights. However, this should only be to the extent that the rows remain distinctive and not mixed-up, i.e., not over exposed, or saturated. In addition, a robust image processing algorithm, see Figure 4.7, is proposed to enhance the success rate of received bits.

Note, the noise sources in ISs can be categorised as either temporal or spatial noise. The former includes thermal noise, photocurrent shot noise, and flicker noise [182]. The latter known as the fixed pattern noise, which depends on the T_{exp}, and is mainly due to the dark current non-uniformity in a CMOS IS under dark conditions, whereas under illumination, it is the result of the gain variation of the active transistors inside each pixel [182].

Next, the schematic block diagram of the proposed system is shown in Figure 4.5. It is composed of a 2.5 × 2.5 cm^2 small size chip on board matrix LED as the Tx and a CMOS RS-

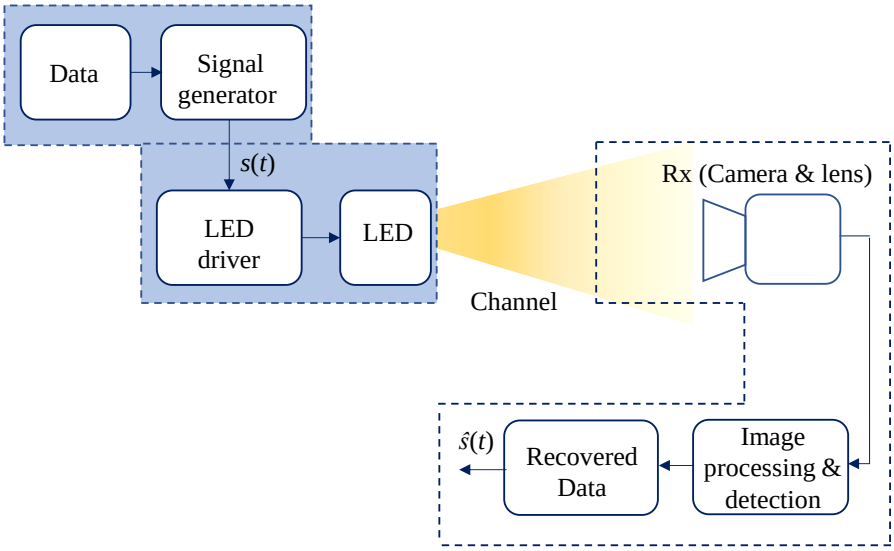

Figure 4.5: Block diagram of the long-distance OCC system

based camera mounted on a prime lens as the Rx. At the Tx, a non-return to zero (NRZ)-OOK data stream $s(t)$ is used for intensity modulation of the LED via the LED driver. The intensity-modulated light is then transmitted over the free space channel and captured at the Rx side. The current-voltage profile of the Tx is shown in Figure 4.6, showing the non-linear and linear regions of the LED. Note, the linearity of LEDs is important as it impacts the achievable transmission capacity (high linearity and dynamic range supports higher-order multi-level and multi-carrier modulation schemes) or the transmission distance.

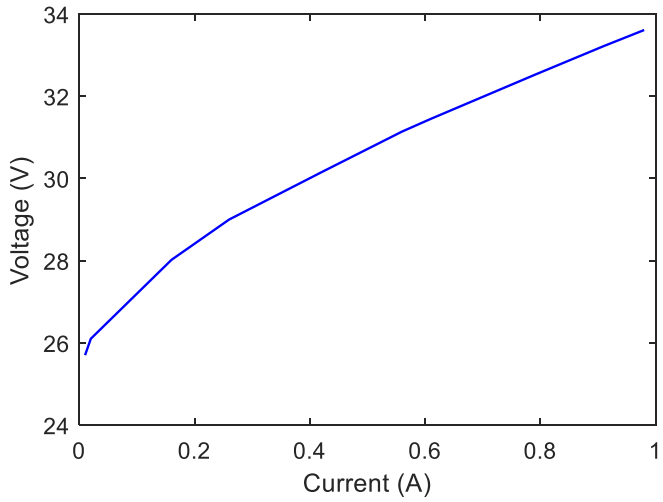

Figure 4.6: Current-voltage profile of the Tx

Consequently, the camera (IS) output at the Rx side is processed off-line in MATLAB. As shown in the image processing and detection flowchart in Figure 4.7, there is the conversion of both calibration and data video streams following pixelation from the RGB videoframe to the grayscale format. Note, the shape of Tx's template is used for equalisation or intensity compensation of the captured data video frames.

Next, the region of interest (ROI) is selected (representing the Tx's footprint on the IS) i.e., the CoC, which is averaged over the rows to form a column vector. To avoid noise amplification at the start and end of the pixel rows, at least 10-pixel rows are excluded from the bottom and top of the CoC. Moreover, the received signal is up sampled

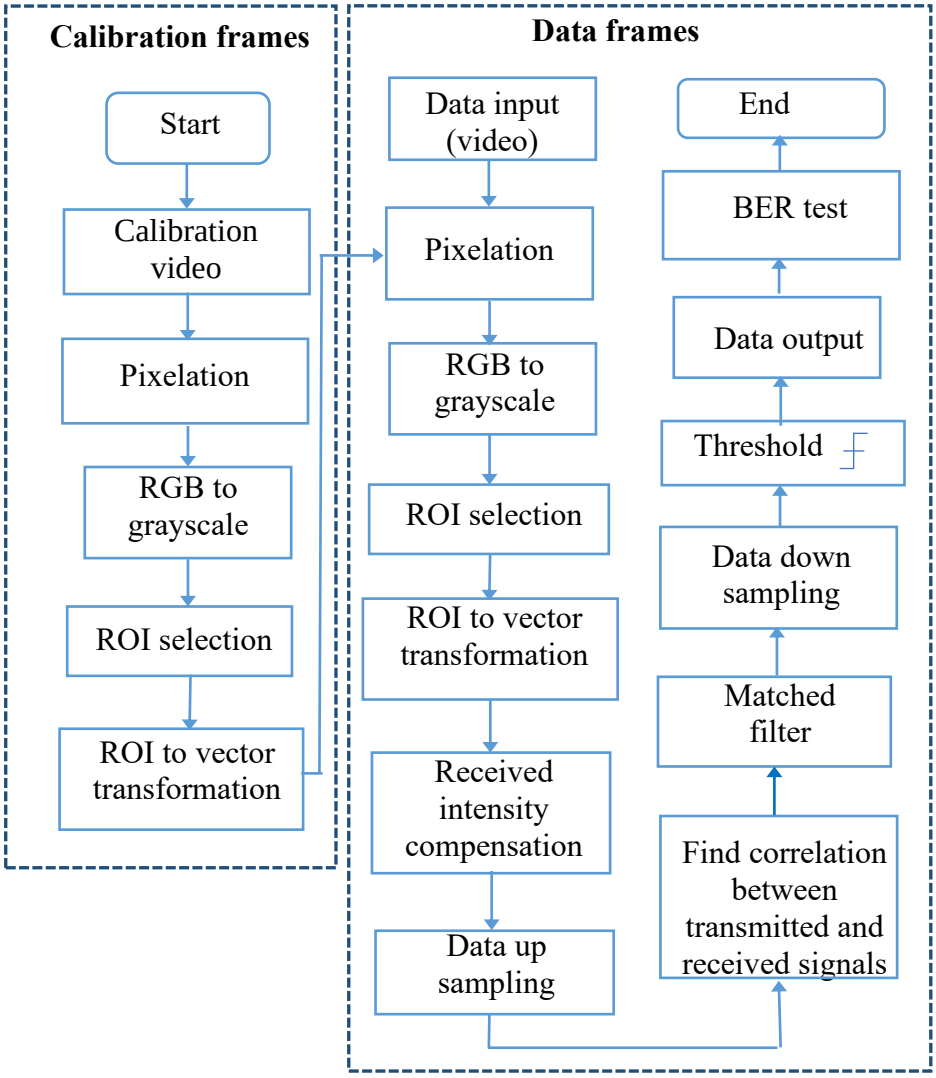

Figure 4.7: Image processing and detection flowchart

(number of samples per bit n_{sam} = 100), to increase the resolution, which enables more accurate decoding of the received data bits while down sampling with a whole integer number (in MATLAB®). To extract and recover the required data packet, correlation between the transmitted and received signal is carried out followed by a matched filter (MF) (via postprocessing in MATLAB®) applied to the received signal. The SNR is maximised using MF, and consequently improving the BER performance. The impulse response of the MF is the time-reversed of the Tx impulse shaping filter. The recovered data vector after down sampling and thresholding is then compared with the transmitted bit stream to obtain the transmission success rate i.e., by determining the ratio of bits wrongly decoded to the total number of bits transmitted i.e., the BER.

4.4 Experimental Setup and Results

The system configuration and experimental setup for the long-distance OCC link are presented in Figure 4.8. The Rx was located outdoor at a height of ~1.4 m above the ground level, while the Tx was placed on the 6th floor (i.e., a height of ~25 m). At the start of the measurement campaign, the weather was partly cloudy/sunny while by the end it was sunny, with a temperature range of 23-25°C while the humidity and wind speed were 51 - 65 % and 2 - 6 mph, respectively. The key experimental parameters adopted in this work are listed in Table 4.7.

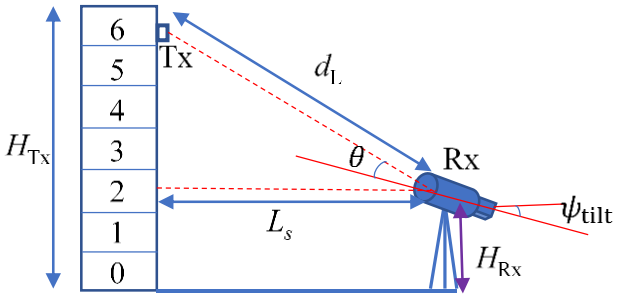

(a)

(b)

Figure 4.8. Proposed OCC link: (a) system configuration, and (b) experimental setup showing the Tx and the Rx

Table 4.1: Key experimental parameters

	Parameter	**Value**
Tx	Bias current	0.33 A
	Tx surface area	2.5×2.5 cm^2
	Lambertian order of emission m	0.96
	Half power angle	61^o
Camera and lens	Lens aperture	f/10
	Focal length	1 m
	Frame rate	25 fps
	Resolution	648 × 484 (RGB32)
	Pixel size	2.2×2.2 μm^2
	Extracted N_{rows} per frame	18
	Total number of N_{rows} per frame	~32
	Exposure time T_{exp}	100-800 μs
Packet generator	Data format	NRZ-OOK
	Packet generator sample rate	533.16 Hz
	Number of samples per bit	10
Channel	Horizontal link distance	150-400 m

Measurements were carried out for a range of T_{exp} and L_s of 100 to 800 μs and 150 to 400 m, respectively. Up to 100 % reception success rate were obtained for all link configurations investigated. To quantify the link performance for each L_s, we used the image quality metric known as the PSNR, which is given by [183]:

$$\mathrm{PSNR} = 10\log\frac{I_{\mathrm{mx}}^2}{\mathrm{MSE}}, \tag{4.10}$$

where I_{mx} = 255 for the grayscale image (i.e., the maximum possible pixel value), and MSE is the pixel luminance mean squared error, which is defined by:

$$\mathrm{MSE} = \frac{1}{N_{\mathrm{rows}}}\sum_{1=\mathrm{j}}^{N_{\mathrm{rows}}}(I_{\mathrm{Tx}}(j) - I_{\mathrm{Rx}}(j))^2, \tag{4.11}$$

where I_{Tx} is the difference between the pixel values for the transmitted symbols (symbols 1 and 0 here), while I_{Rx} is the difference between the average pixel value for the received symbols (symbols 1 and 0) and j is the pixel's row index number.

Figure 4.9 shows the PSNR as function of L_s for a range of T_{exp}. As illustrated, PSNR decreases with the increasing L_s but improves with T_{exp}. For example, for T_{exp} of 800 µs, PSNR drops by 2.1 dB when L_s increases from 200 to 400 m. Also, the maximum values of PSNR are 0.2 and 3.3 dB for T_{exp} of 100 and 800 µs at L_s of 150 m. This is so because as earlier highlighted, increasing T_{exp} allows more amount of light to be captured hence the improvement in the PSNR value at higher T_{exp}.

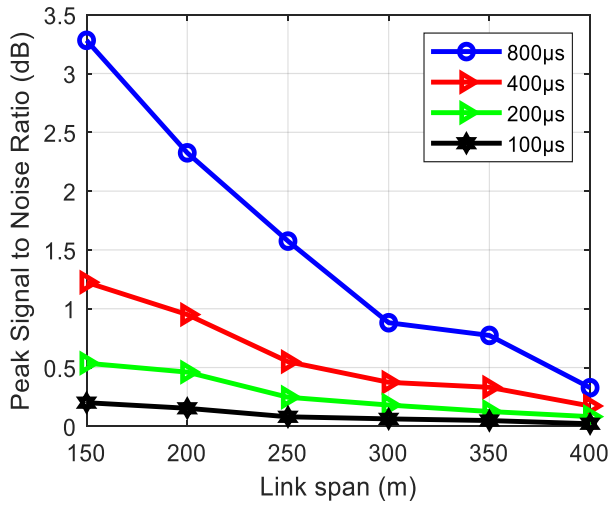

Figure 4.9: PSNR as a function of link span for a range of T_{exp}

Furthermore, examples of the received waveforms and captured images of the received signal for L_s of 150 and 400 m at T_{exp} of 400 µs and L_s of 400 m at T_{exp} of 100 µs are depicted in Figure 4.10 (a), (b) and (c), respectively. For L_s of 150 m (Figure 4.10 (a)), the captured image shows

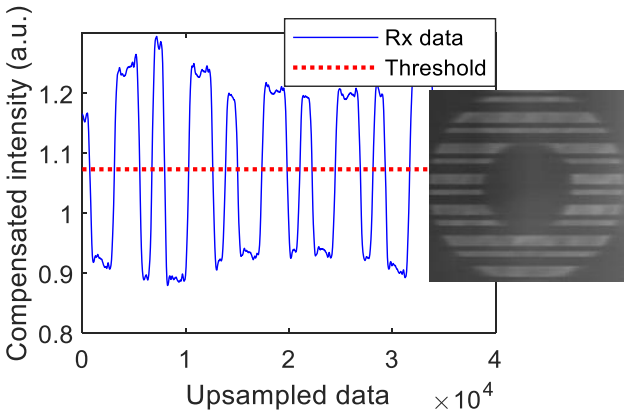

(a)

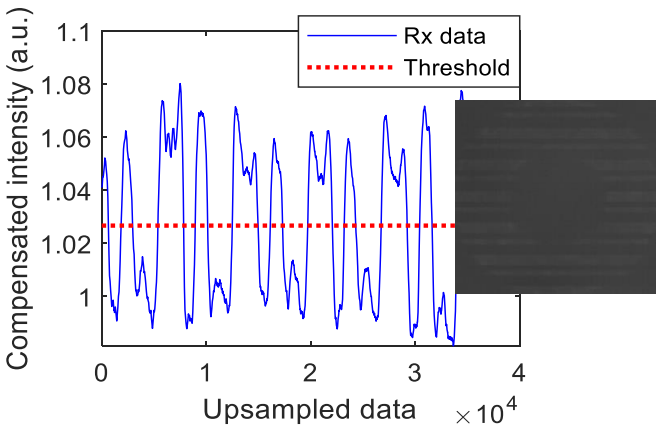

(b)

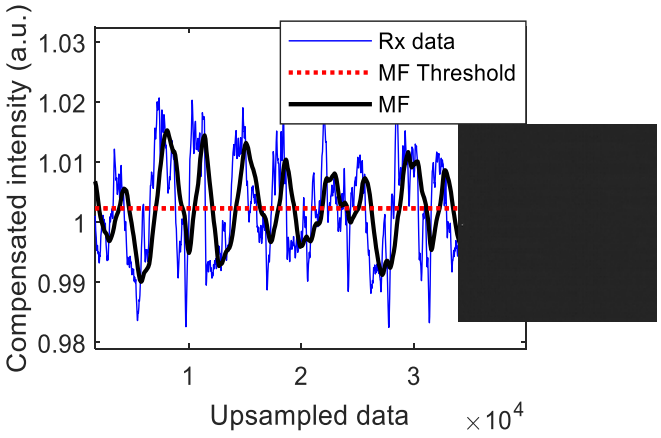

(c)

Figure 4.10: Examples of waveforms and the captured image frames of the received signal at: (a) L_s of 150 m, and T_{exp} of 400 µs, (b) L_s of 400 m, and T_{exp} of 400 µs, and (c) L_s of 400 m, T_{exp} of 100 µs

a clearer distinction between the received symbols 1 and 0 (i.e., on and off states of the Tx) than in Figure 4.10 (b) where the link span is longer with the same T_{exp} of 400 μs. While Figure 4.10 (c) demonstrate the worst-case scenario where the captured image appears totally black to the observer's eyes i.e., the on and off states of the Tx appear indistinguishable. This is so because in comparison with Figure 4.10 (b) where the same link distance is considered but a higher T_{exp} (allowing the capturing of more amount of light) there is an improved received signal waveform and captured data image than in Figure 4.10 (c) with a lower T_{exp}. For the waveform (in Figure 4.10 (c)), an improved recovered signal employing a MF is shown, enabling the decoding of the received data. Note that, in Figure 4.10 the raw received upsampled data is shown that does not directly correspond to the number of bits received.

4.5 Summary

A novel technique was developed for extending the transmission range of a RS-based OCC link by reducing the spatial bandwidth of the camera in the out of focus regions i.e., defocusing the camera. The experimental demonstration of the proposed scheme showed a 100 % reception success rate for a link span of up to 400 m, which is the longest reported till date. Moreover, the choice of T_{exp} played a key role in the PSNR performance of the link. An image processing algorithm was also developed and designed to extract the data out of the captured image frames. The proposed system relaxes the condition of using a very large surface area Tx light source, which is impractical for vehicular networks as there are limits to the sizes of the roadside traffic units and vehicle lightings but could be used in other VLC-OCC applications.

CHAPTER 5
TURBULENCE AND FOG EFFECTS ON VEHICULAR VLC

5.1 Introduction

This chapter presents the performance of vehicular VLC under atmospheric turbulence and fog, which is investigated by means of experiments, following up on the discussion of the challenge of increasing the robustness to noise of the vehicular VLC systems in Chapter 2. The chapter is organized as follows: turbulence effects and techniques proposed to combat it in laser based OWC systems are outlined. Experimental investigations of the vehicular VLC link using a non-collimated and an incoherent light source (i.e., a LED) as the Tx and two different optical Rx types, i.e., a camera and a photodiode (PD), under turbulence with aperture averaging are also carried out. Furthermore, the effects of fog on camera based vehicular links are experimentally investigated.

5.2 Turbulence Effects

Atmospheric turbulence, which causes random fluctuations in both the phase and amplitude of propagating optical beams, can lead to fading and consequently

reduced SNR [54-56]. Hence, channel modelling for vehicular VLC is very crucial. Notably in vehicular VLC systems two types of Rxs are used depending on the application: (*i*) a PD and a camera; and (*ii*) the effects of atmospheric turbulence have been extensively studied in OWC links based on a coherent and highly collimated light source, i.e., lasers and a PD as the Tx and the Rx, respectively. However, only few reports for OWC links where an incoherent and non-collimated light source i.e., LEDs are used as Txs as earlier highlighted in Chapter 2, where also related works on turbulence effects on vehicular VLC were discussed.

To reduce the degradation of the propagating signal due to turbulence effects, a number of options have been proposed for laser-based OWC links, including (*i*) spatial diversity with adequate Rx spacing [184-187], which is not suitable in vehicular VLC since the width of vehicles is relatively small, i.e., within the range ~1.4-2.0 m [115] and hence the acceptable Rx spacing to obtain significant performance improvements on the Rx vehicle is limited; (*ii*) beam width optimization [56, 188], where the radiation pattern of the beam is altered, which is also impractical in vehicular VLC since vehicles will have different HL and TL shapes, dimensions, and radiation patterns. In addition, using additional optics in HLs, TLs and road/traffic infrastructures to change the radiation properties may not be a viable option; (*iii*) complex modulation techniques [189-191]; (*iv*) error control coding techniques such as turbo coding, low density parity codes etc., which provide good resistance to burst errors in fading channels [192-195]. However, the latter often causes an increase in the latency, which is not desirable in vehicular communications i.e., pre-crash sensing requiring a maximum latency of 20 ms as shown in Table 1.1; and (*v*) aperture averaging [196-199], which is the simplest method and can be easily achieved in a vehicular VLC system at the Rx side. Aperture averaging involves using a lens in front of a small optical detector, thus increasing the

collection area, hence lowering the effects of turbulence, and spatially filtering the high fluctuations of the received optical beam. The aperture averaging factor is expressed as [196] $\frac{\sigma_I^2(D)}{\sigma_I^2(0)}$, where $\sigma_I^2(0)$ is the scintillation index for a point Rx ($D \approx 0$) (i.e without the use of an OC) and $\sigma_I^2(D)$ is the variance of the intensity fluctuations for an OC of diameter *D*.

5.3 Experimental Investigation of the Turbulence Effects with Aperture Averaging

5.3.1 Experimental testbed

Experimental investigation on turbulence with aperture averaging is carried out. Figure 5.1 depicts the schematic block diagram of the proposed vehicular VLC system with the camera- and PD-based Rxs with aperture averaging. The Rx1 and Rx2 are composed of a camera (Thorlabs DCC1645C-HQ) with a lens (MLH-10X), and a PD (PDA100A2) with a convex lens, respectively. An indoor laboratory atmospheric chamber is used to simulate the outdoor atmospheric turbulence as proposed in [86, 200]. At the Tx side, the data packets of length 90 bits in the NRZ-OOK format are generated using an arbitrary waveform generator, the output of which is used for intensity modulation of the TL (Truck-trailer DACA08712AM) through the driver module. The intensity-modulated optical beam transmitted over a dedicated atmospheric chamber is captured at the Rxs. Turbulence is generated within the chamber by varying the temperature along the transmission path using hot/cold fans. A temperature sensor array was used within the chamber to measure the temperature distribution, which consisted of seventeen active temperature sensors, and was more than sufficient in this work.

However, higher number of them could be adopted for improved accuracy. The key experimental parameters adopted in the proposed system are listed in Table 5.1.

Table 5.1: Key parameters of the experiment

Description		**Value**
Tx	Truck-trailer DACA08712AM	
	Peak wavelength	630 nm
	Bias current	98 mA
	Transmit power	32.4 mW
	Bandwidth	539 kHz
PD Rx	Thorlabs PDA100A2	
	Responsivity	0.43 A/W at 630 nm
	PD area	0.75×10^{-4} m^2
	Bandwidth @ 0 dB gain	11 MHz
	Noise equivalent power @ 960 nm	7.17×10^{-11} W$\sqrt{\text{Hz}}$
	Lens focal length f	25 mm
	Lens diameter D	25 mm
Camera Rx	Thorlabs DCC1645C-HQ	
	Camera shutter speed	600 μs
	Camera gain factors	1.07×, 3.96×
	Lens focal length f	130 mm
	Lens aperture	f/5.6
	Samples per frame	2588
	Pixel clock	10 MHz
	Camera frame rate	6.25 fps
	Camera resolution	1280 ×1024
Packet Generator	Data format	NRZ-OOK
	Packet generator sample rate	11.125 kHz
	Number of samples per bit n_{sam}	10
Channel	Link distance	7.2 m

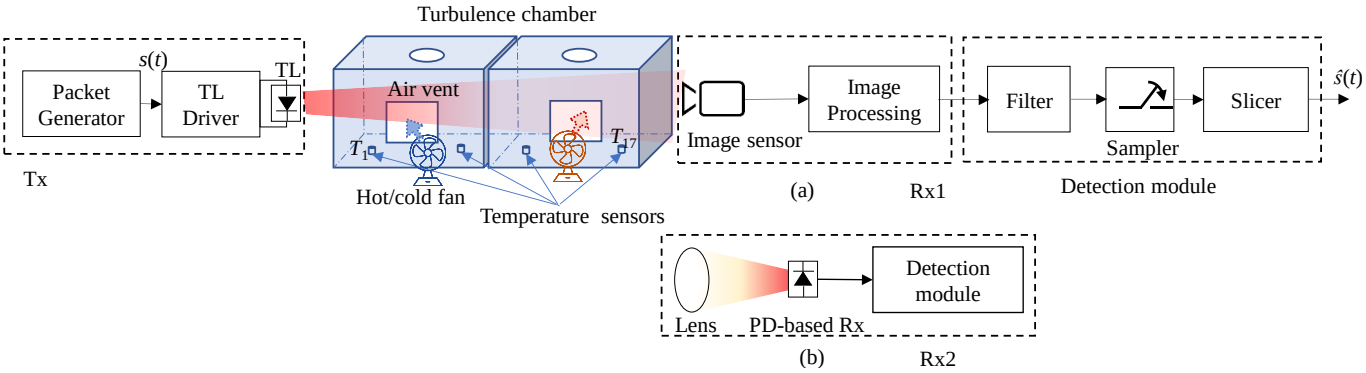

Figure 5.1. Experimental setup of the investigation on turbulence effects on the vehicular VLC link with: (a) camera, and (b) PD Rx

Also, the normalised illuminance as function of the bias current is shown in Figure 5.2 (i.e., demonstrating the current to optical power output characteristics of the LED used). Note that, the bias current of 98 mA was determined based on the required operating voltage (i.e., 12 V) for this specific vehicle TL in use. However, its important when modulating LEDs to use the linear region for the optimum performance.

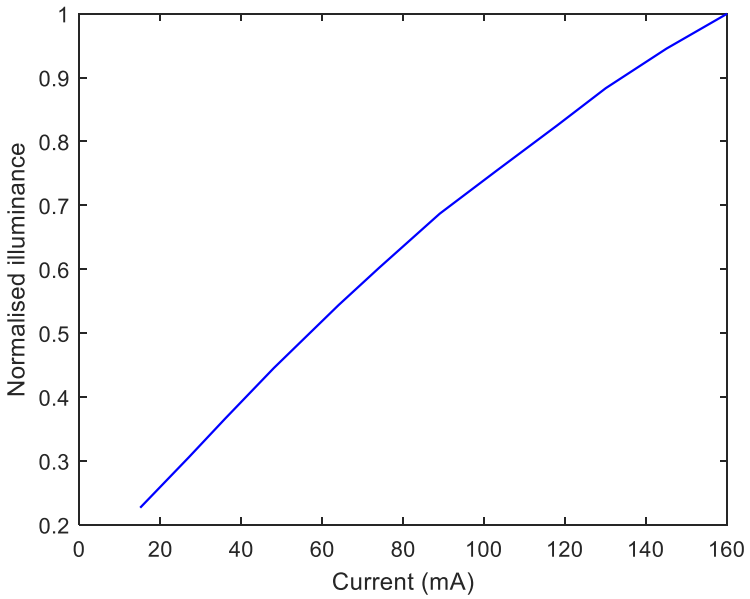

Figure 5.2: Illuminance-current characteristics of Truck-trailer DACA08712AM

5.3.2 Signal extraction

At the Rx side, the captured regenerated electrical signals from the camera- and PD-based Rxs are processed off-line in MATLAB®. The image processing algorithm for signal extraction for the RS camera-based Rx is shown in Algorithm 1, where the captured frames' red, green, and blue (RGB) components are converted to the grayscale for both calibration and data image frames following pixelation (i.e., digitizing the image to obtain the pixel value). Note, the calibration and data image frames are the captured template shape of the Tx (i.e., the DC gain) and the transmitted data, respectively. The former is used for the intensity compensation (i.e., normalization) of the data image frames. Thereafter, the captured data frames are then normalized over the rows to obtain the received signal waveform, as shown in Figure 5.3 (a) and (b), which is an example of a captured frame before and after normalization, respectively. Note that, in RS-based cameras, the camera sequentially integrates incoming light illuminating the camera pixels, thus offering flicker-free transmission with increased data rates higher than the camera's frame rate.

For the Rx2 i.e., the PD-based Rx, the signal is captured using a digital oscilloscope (Agilent Technologies DSO9254A) for offline processing in MATLAB®. For both Rxs, the detection process is composed of (*i*) a low pass Butterworth filter (3rd order, which gave the best output, with a normalized cut off frequency w_n of 0.25π rad/sample for the camera received signals and a 1st order with $w_n = 0.1\pi$ rad/sample for the PD received signals are used); (*ii*) a sampler (sampling at the middle of the samples received for each bit and at an interval of n_{sam}); and (*iii*) slicer with the threshold level set to the mean value of the signal, which is done per frame.

Algorithm 1 Image Processing Algorithm for Signal Extraction

Input: Captured data frames $\mathbf{F}_{U \times V \times 3}$ and the DC signal only frames $\mathbf{G}_{U \times V \times 3}$

Output: $\boldsymbol{s}_{\text{cal}}$

For each $\mathbf{F}_{U \times V \times 3}$ **do**

Read $U \times V \times 3$ sized frame $\mathbf{F}_{U \times V \times 3} = [[F(i,j,c)]$. The RGB components of $\mathbf{F}_{U \times V \times 3}$ denoted as $\mathbf{RF}_{U \times V} = RF(i,j)$, $\mathbf{GF}_{U \times V} = GF(i,j)$, $\mathbf{BF}_{U \times V} = BF(i,j)$, respectively, i = 1, 2, …, U and j = 1, 2, …, V represents the pixels indices of captured frame, and c = 1, 2, 3.

Apply grayscale conversion by calibrating the RGB components $\mathbf{RF}_{U \times V}$, $\mathbf{GF}_{U \times V}$, and $\mathbf{BF}_{U \times V}$ together over c, resulting $\mathbf{FS}_{U \times V}$.

Accumulate intensities for all pixels at each row $s = (s_i)_{i=1}^{V}$ where $s_i = \sum_{j=1}^{V} \mathbf{FS}_{U \times V}$.

Compute the averaged DC value $\bar{s}_{\text{DC}}$ by repeating previous steps on $\mathbf{G}_{U \times V \times 3}$.

Calibrate s with respect to the averaged DC value $s_{\text{cal}} = s/\bar{s}_{\text{DC}}$

Resample $\boldsymbol{s}_{\text{cal}}$ with respect to the packet length

End.

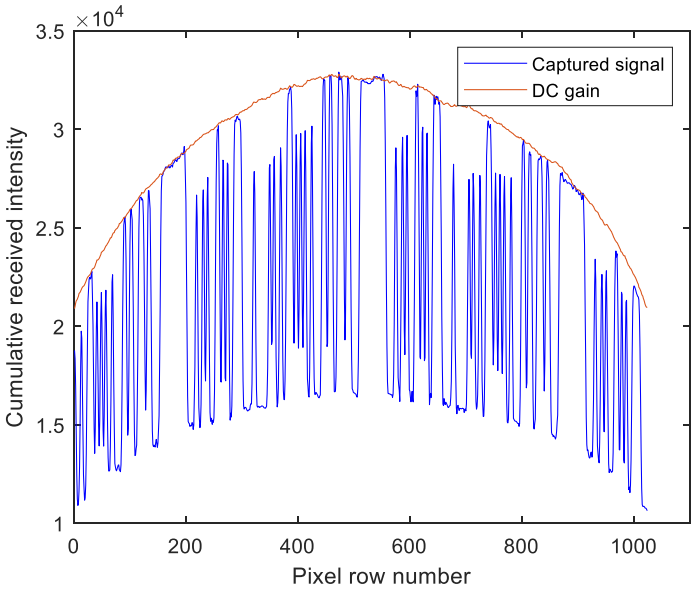

(a)

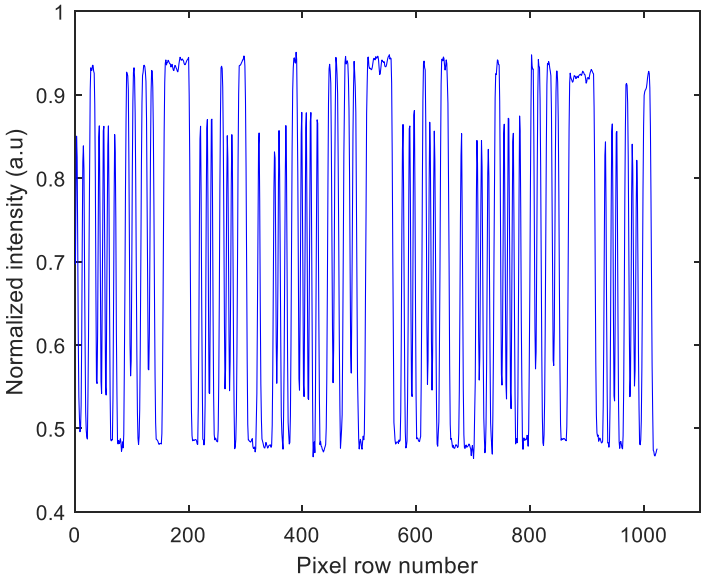

(b)

Figure 5.3: An example of a captured image frame for the camera-based Rx: (a) before, and (b) after intensity normalization

5.3.3 Results and discussions

5.3.3.1 Camera-based Rx

Measurements were carried out for the link with and without atmospheric turbulence for the camera shutter speed of 600 µs and the low and high gain factors of 1.07 times (×) and 3.96×, respectively. Note, the camera-based Rx used has a gain factor in the range of 1× to 4.27×; where 4.27× and 1× imply the maximum gain and no gain, respectively. Therefore, to evaluate the link quality, we have used the PSNR as given in (4.10) and (4.11) (where I_{Tx} is the pixel values for the transmitted symbols (i.e., 1 and 0), and is computed from captured images at approximately a zero distance from the Tx, while I_{Rx} is the average pixel value for the received symbols). Figure 5.4 shows the PSNR versus C_n^2 with aperture averaging for the high and low gain factors. From Figure 5.4, the following can be observed with aperture averaging (*i*) the PSNR is almost independent of turbulence with a marginal drop for the link with a gain factor of 3.96×; and (*ii*) there is a PSNR gain of ~7 dB for the captured frames at the higher gain factor. This is because the camera's analogue gain can optimize the SNR by reducing the quantization noise [201] and increase the image brightness/contrast, hence the higher PSNR value at higher gain factor. The use of the camera's analogue gain feature to overcome attenuation due to fog and sandstorm in an OCC link has been recently proposed in [202-203] to improve the signal quality (i.e., to obtain sharper images) without increasing the exposure time, and therefore maintaining the bandwidth of the system. Notably, both the image brightness and its contrast increase with the camera's gain factor since the signal is amplified prior to the digitizing process [204]. The choice of the two gain factors (i.e., high and low) is used to demonstrate the image brightness/contrast effects under turbulence.

Note, the corresponding σ_R^2 for the experimentally measured C_n^2 for different atmospheric turbulence strengths are calculated using (2.8) for L_s equal to the length of the turbulence chamber (i.e., 7.2 m), which are given in Table 5.2.

Table 5.2. σ_R^2 for corresponding C_n^2 values measured in the experiments

	C_n^2 ($\mathrm{m}^{-2/3}$)	σ_R^2
PD	3.9×10^{-11}	0.2619
	7.9×10^{-11}	0.5304
	1.0×10^{-10}	0.6714
Camera	3.6×10^{-11}	0.2417
	3.9×10^{-11}	0.2619
	7.9×10^{-11}	0.5304
	8.0×10^{-11}	0.5371
	8.3×10^{-11}	0.5573
	1.1×10^{-10}	0.7386

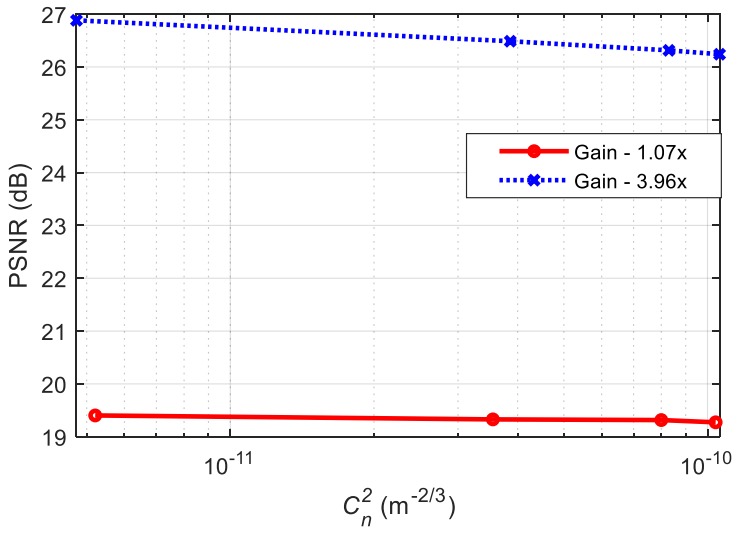

Figure 5.4. The PNSR as a function of C_n^2 for the two gain factors

Figure 5.5 shows the captured received signal waveforms prior to being applied to the detection module for different turbulence strengths with aperture averaging following

normalization. As noticed, the received signal utilizing a higher camera gain factor displays improved the PSNR performance and higher received signal intensity with lower intensity fluctuations. The BER measured was less than the target BER of 10^{-4} for all the link scenarios considered.

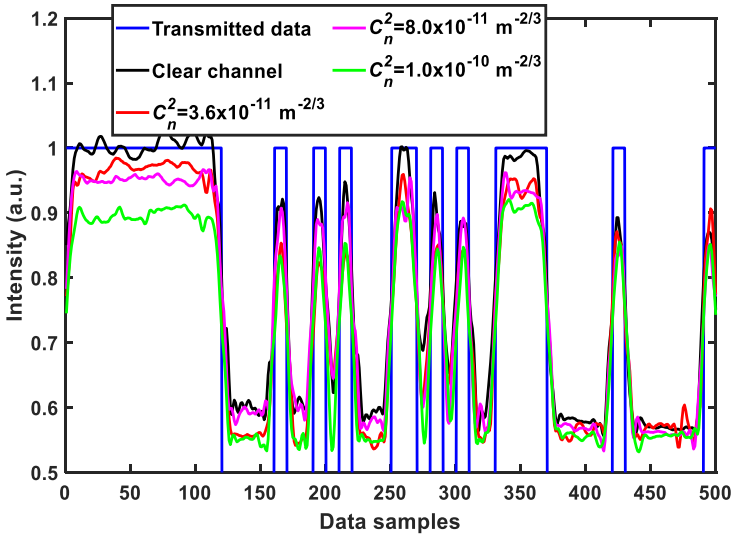

(a)

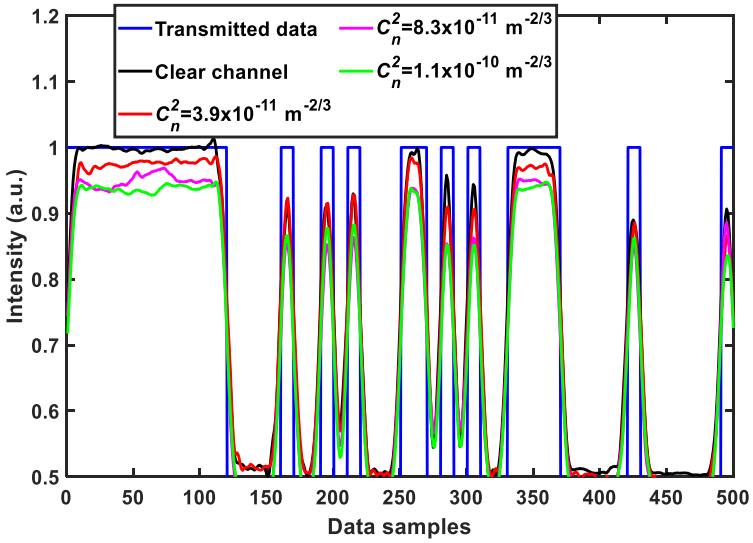

(b)

Figure 5.5: Waveforms of Rx data at varying turbulence strengths for gain factors of: (a) 1.07x, and (b) 3.96x

Furthermore, the histogram plots prior to the detection are depicted in Figure 5.6 (a)-(d), which illustrates the distributions of the discrete intensity levels of the captured images within the range of 0 to 1 for each link scenario investigated. While Figure 5.6 (e) shows the histogram for the sampled received intensity levels of Figure 5.6 (a) at the output of the sampler (i.e., within the detection module). Notably, there is a slight merge between the received intensities for the bits 1 and 0 in Figure 5.6 (a)-(d), which is due to the slow rise-time of the captured off and on states of the Tx [164]. This is due to the transition between different illumination levels brought about by the sampling process in the RS-based camera [164]. Thus, this happens at the transition edges, however for the proposed detection module, the sampling takes place at the centre of the received samples per bit; hence the system's performance is not degraded and bits 1 and 0 are clearly distinguishable as in Figure 5.6 (e). Moreover, it can be seen that the link with a lower gain factor (i.e., Figure 5.6 (a) and (b)) has lower peak counts than Figure 5.6 (c) and (d) with the higher gain factor.

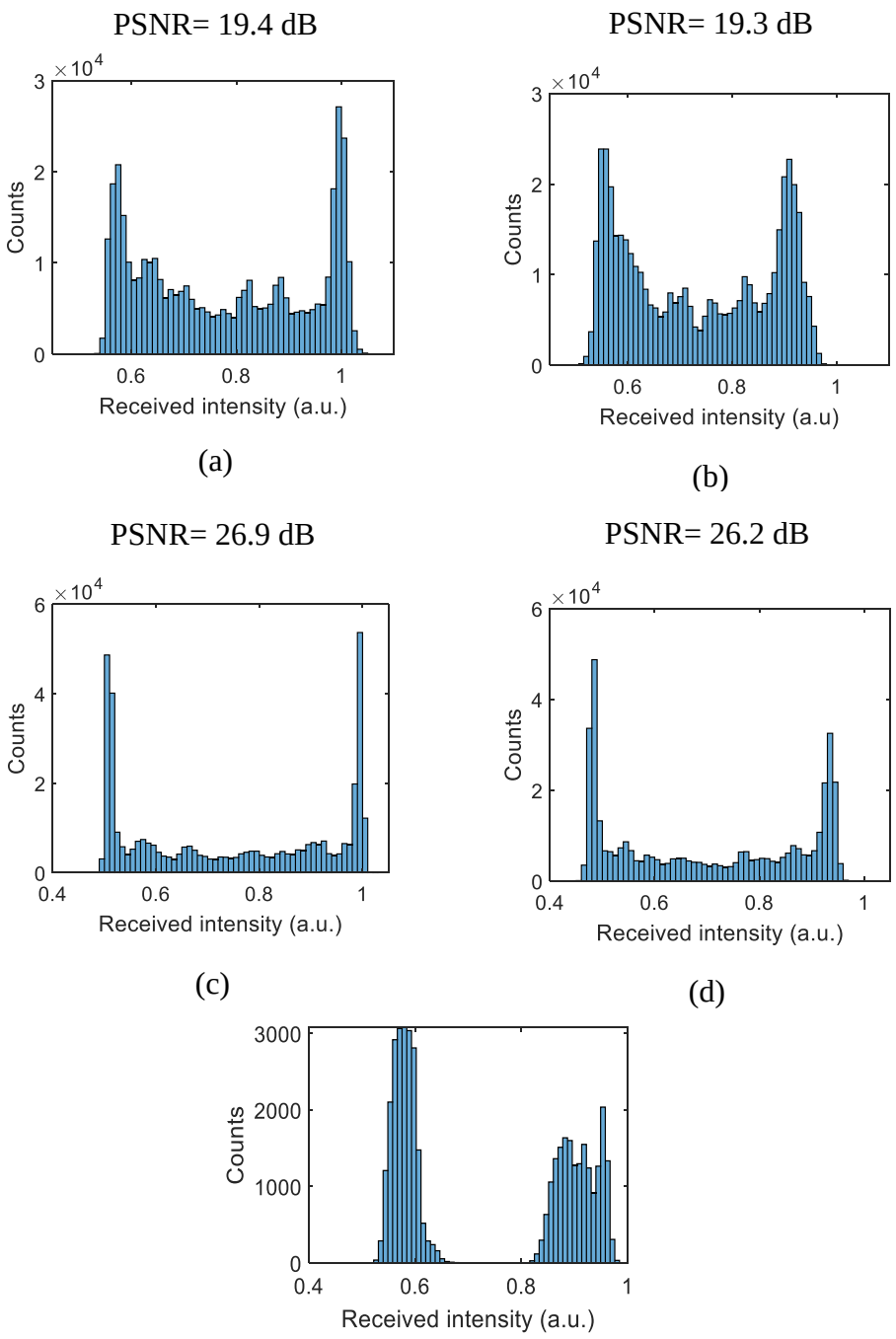

Figure 5.6. Camera Rx histogram plot: prior detection module for: (a) gain 1.07× with no turbulence, (b) gain 1.07× with the highest turbulence scenario, $C_n^2 = 1.0 \times 10^{-10}$ m$^{-2/3}$, (c) gain 3.96× with no turbulence, and (d) gain 3.96×, with the highest turbulence scenario $C_n^2 = 1.1 \times 10^{-10}$ m$^{-2/3}$, and (e) output of sampler for (a)

5.3.3.2 PD-based Rx

For the link with aperture averaging and the PD-based Rx, the SNR of the captured signals is measured and the histogram plots for bits 1 and 0, i.e., the signal distribution profile for the channel without and with turbulence prior the detection is shown in

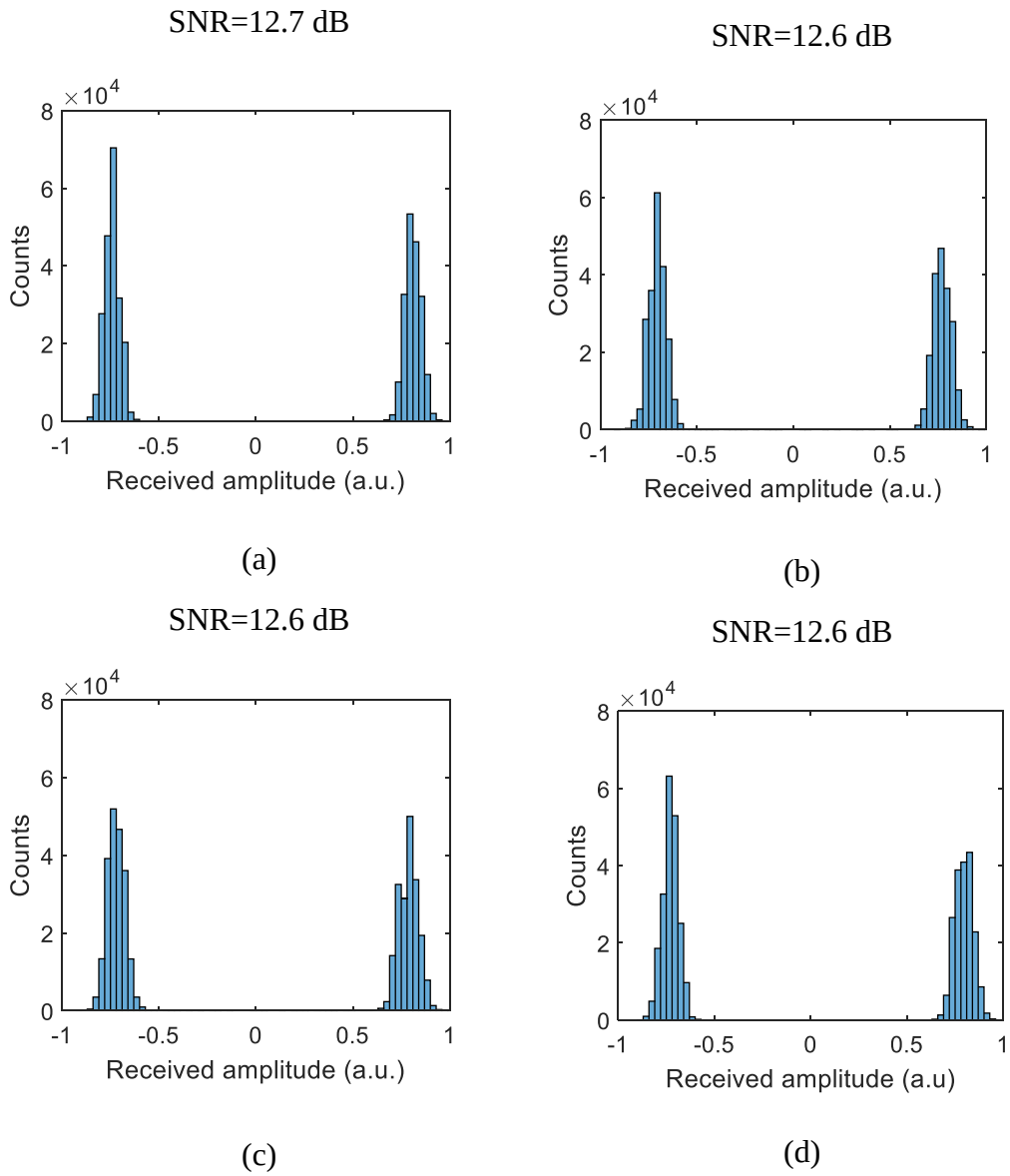

Figure 5.7: PD Rx histogram plot for: (a) clear channel, and with turbulence conditions of (b) $C_n^2 = 3.9 \times 10^{-11}$ m$^{-2/3}$, (c) $C_n^2 = 7.9 \times 10^{-11}$ m$^{-2/3}$, and (d) $C_n^2 = 1.0 \times 10^{-10}$ m$^{-2/3}$

Figure 5.7. From the results obtained, (*i*) the histogram plot indicates a clear distinction between the received signal for bits 1 and 0; and (*ii*) the average SNR is independent of the weak to moderate turbulence (with only ~0.1 dB of SNR penalty compared with the clear channel with OC). Hence, this demonstrates that aperture averaging can effectively mitigate the induced signal fading due to turbulence for the vehicular VLC systems under weak to moderate turbulence regimes. Note, strong turbulence regimes would not normally be experienced in vehicular communications due to the relatively short link spans (tens to few hundreds of metres) compared with free space optical links (> several kilometres).

5.4 Fog Effects

The effect of fog on a vehicular VLC link using a camera-based Rx is carried out and discussed in the following subsections. All previous works based on vehicular VLC links under fog conditions as outlined earlier in Chapters 1 and 2 have reported results based on the use of only a PD-based Rx and not a camera Rx at the time of carrying out this investigation. Consequently, experimental investigations on the effects of fog on a camera-based vehicular VLC link by considering a range of visibility levels and inter-vehicle distances were carried out. Note, a global shutter-based camera capturing mode is employed where at least a frame is used to represent a bit. Therefore, it is necessary during communications to be able to track the light source to maintain the communications link for global shutter-based camera links. This is very important particularly when a '0' symbol is transmitted, in which the TL is off if a modulation index (MI) of 1 is used and it is therefore difficult to track the light source in the camera image. A reduction in the MI of the signal from 1 to 0.75, and 0.5 were considered and the transmission success rates for a range of visibilities are presented.

5.5 Investigation on Fog Effects

5.5.1 Experimental setup

The schematic block diagram of the proposed vehicular VLC link for the investigation of fog effects is depicted in Figure 5.8. It comprises a real vehicle LED-based TL (i.e., Nissan 26550 4EA0A model) as the Tx and a camera (Canon Rebel SL1 EOS 100D) as the Rx. A laboratory chamber is used to simulate the outdoor foggy channel, the same as for the turbulence investigation in the proceeding subsections as proposed in [205,206]. NRZ-OOK data stream $s(t)$ is used at the Tx for intensity modulation of the TL. The data stream is a short traffic message with a payload and a header of 175 and 21 bits, respectively. The intensity modulated light $x(t)$ is transmitted through the clear channel (i.e., no fog). The signal is captured using a camera at the Rx side and the captured image frames are processed off-line in MATLAB®. The image processing steps include the conversion from RGB to grayscale, region of interest selection. Next, the sampler and slicer are applied, and the received bits are compared with the transmitted bits to determine the BER (i.e., the transmission success rate).

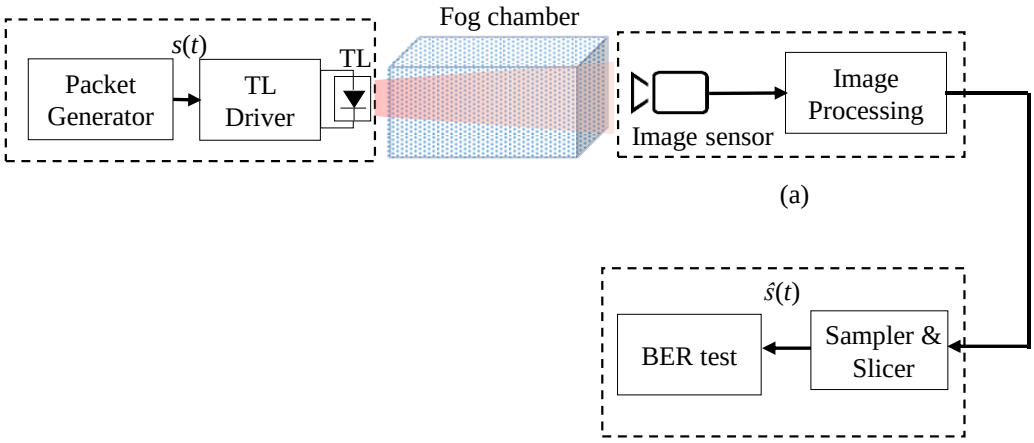

Figure 5.8: The schematic block diagram of a vehicular VLC based camera link

5.5.2 Inter-vehicle distance

It is important to know the allowable inter-vehicle distances on the roads for safe driving so as to correctly investigate practical scenarios for vehicular VLC communications. Typically, a two-second rule is recommended whereby a driver maintains a minimum of two seconds behind the vehicle in front for perfect weather conditions, which is doubled to four seconds in bad weather. Moreover, some other driving rules recommend three, six, and nine-second rules for good, average, and bad weather conditions, respectively [207]. Figure 5.9 shows the inter-vehicle distance for the 2 and 3 s rules for good to bad weather conditions. Besides, there are different speed limits in adverse weather conditions; however, the European Commission regarding mobility and transport gives a speed limit of 50 km/h in fog conditions for a meteorological visibility of < 50 m [208]. Therefore, for the worst-case scenario i.e., using the 3 s rule for bad weather and 50 km/h speed limit, the inter vehicle distance is at least 125 m as can be deduced from Figure 5.9.

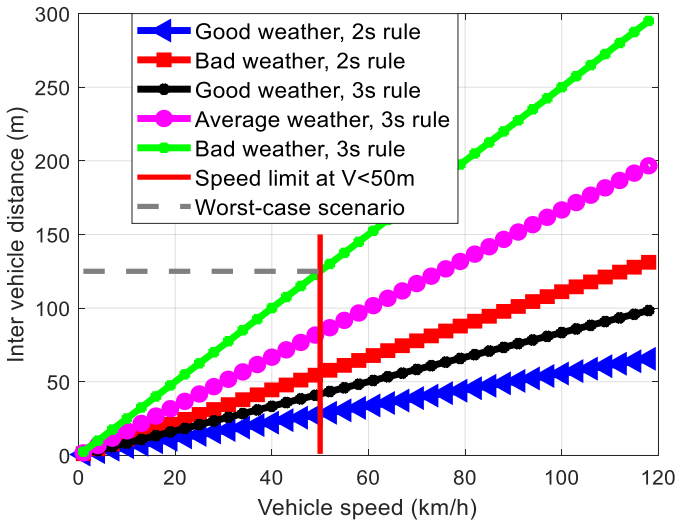

Figure 5.9: Driving distances between vehicles at different speeds using the 2- and 3-seconds rules

5.6 Results and Discussions on the Fog Experiment

The link visibility was measured concurrently at the 550 nm wavelength (using the A_{FOG} parameter from (2.2)) as data was transmitted over the channel. The BER of the link was measured for the fog and clear channel conditions. Moreover, for each meteorological visibility condition, measurements for three MIs (0.5, 0.75 and 1) were carried out. The choice of a MI lower than 1 is because in vehicular communications the position of the Tx/Rx constantly changes with respect to each other due to moving vehicles. The key parameters of the experiment are shown in Table 5.3.

Table 5.3: Key parameters of the fog experiment

Parameter	**Value**
Shutter speed	1/800 s
International Standard Organisation (ISO) of camera	6400
Camera focal length *f*	18 mm
Camera aperture	*f*3.5
Meteorological visibility *V*	5-120 m
Camera frame rate	60 fps
Camera resolution	1280 ×720
Transmission bit rate	30 bps
Number of start bits	21 bits
Number of data bits	175 bits
Link distance	7.5 m
TL transmit power	9.4 mW
TL peak wavelength	624 nm

The percentage success of received bits as a function of the meteorological visibility is displayed in Figure 5.10. The data transmission over the fog channel is

error-free for the MIs of 1 and 0.75 up to a meteorological visibility of 10 m, while for the MI of 0.5 the success rate is reduced to 98.5%. The data transmission success rate decreases considerably with the MI below the meteorological visibility of 10 m with the lowest transmission success rate of 63.3% achieved at a MI of 0.5. Consequently, the results obtained show that the proposed camera-based vehicular VLC link demonstrates high reliability even under the fog condition up to a meteorological visibility of 20 m for all the 3 MIs adopted.

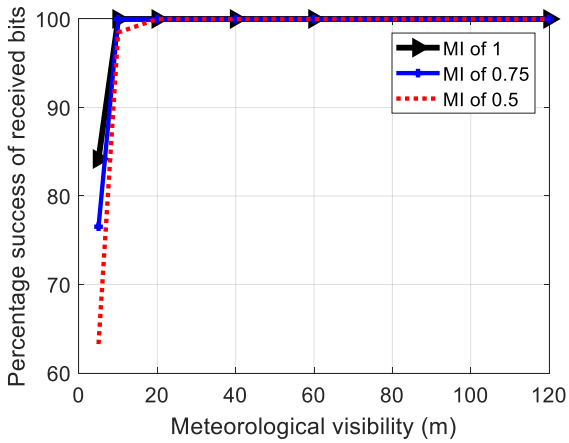

Figure 5.10: The success rate of data transmission with fog for a range of MIs

In addition, insights are provided into the light attenuation due to fog, as shown in Figure 5.11, where the normalized received light intensities of the TL captured by the camera for MIs of 0.5 and 1 for transmission under fog are presented. Note, the received light intensities under fog were normalised with reference to the clear weather condition for each MI. It is apparent from the results that, there is a continuous decrease in the light intensities received as the visibility decreased, as shown by captured images of the car TL as in Figure 5.12. It is noteworthy that, Figure 5.11 shows a non-linear graph because of the type of camera used, which uses a gamma correction factor like the human eye's response to the brightness, which follows a logarithmic law, known as the Weber-Fechner law [209]. At the meteorological visibilities of 10 and 5 m, for both

MIs of 1 and 0.5, the percentage of received light intensities is decreased to about 30 and < 0.5 %, respectively (Figure 5.11), with the latter being the worst-case scenario and the TL is not visible in the captured image as shown in Figure 5.12.

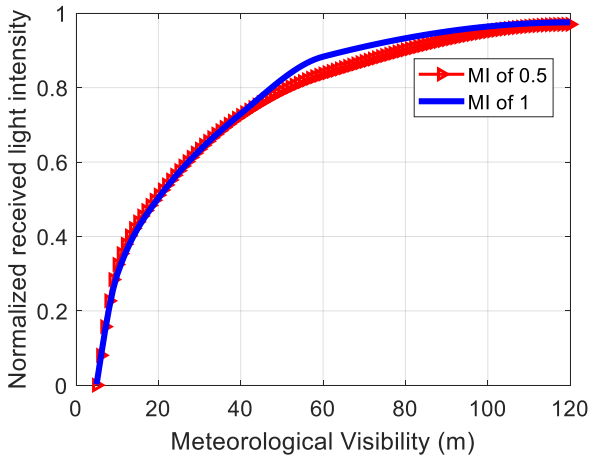

Figure 5.11: Meteorological visibilities versus normalized received light intensity of the vehicle TL by the camera at MI of 1 and 0.5

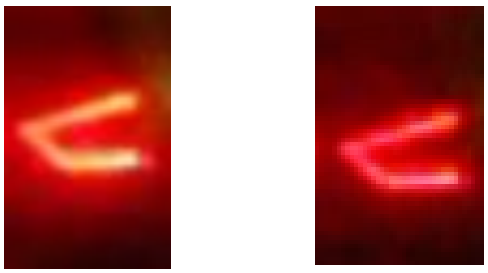

P_{RLI}= 27.0 %

(a)

P_{RLI}= 49.7 %

(b)

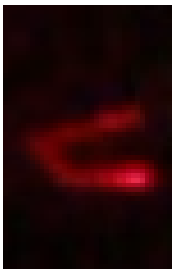

P_{RLI}= 70.2 %

(c)

P_{RLI}= 99.7 %

(d)

Figure 5.12. Captured images of the vehicle TL by the Rx camera for a MI of 1 for: (a) clear channel, and meteorological visibilities of (b) 40 m, (c) 10 m, and (d) 5 m

The percentage loss in the received light intensities P_{RLI} of the TL at the respective meteorological visibilities with reference to the clear weather is provided in Table 5.4. Relating this (Table 5.4) to Figure 5.10 indicates that, the BER is maintained as the received light intensity decreased up to ~ 70 % and then declines sharply.

Table 5.4: Percentage loss in received light intensity over meteorological visibility

Experiment	**Meteorological visibility *V* (m)**	$\boldsymbol{P_{RLI}}$ **(%)** **MI=1**	$\boldsymbol{P_{RLI}}$ **(%)** **MI=0.5**
1	Clear weather	0.0	0.0
2	120	2.5	3.0
3	60	11.7	16.3
4	40	27.0	27.5
5	20	49.7	48.9
6	10	70.2	67.6
7	5	99.7	99.9

5.7 Summary

Experimental investigation on the effects of aperture averaging for the vehicular VLC link under turbulence using an LED-based vehicle TL was carried out. Results obtained showed that, with the aperture averaging, there was no significant system performance degradation under atmospheric turbulence, whereas both SNR and PSNR dropped by 0.1 and 0.7 dB for the PD- and camera-based Rxs, respectively compared with the clear channel. Finally, it was demonstrated that in vehicular VLC systems employing incoherent non-collimated LED light sources as the Tx; the aperture averaging method proved to be very potent to mitigate weak to moderate turbulence

conditions and in fact also increases the optical power density of the received signal at the Rx.

In addition, the effect of varying visibility levels due to fog on the proposed camera based vehicular VLC link was investigated using a vehicle TL as the Tx. Results obtained revealed that the link was reliable (error-free) up to meteorological visibility of 20 m for a MI of 0.5 and even up to 10 m meteorological visibility for MIs of 0.75 and 1. Subsequently, for all three values of MIs, the link degraded considerably below 10 m meteorological visibility.

CHAPTER 6
RELAY-ASSISTED VEHICULAR VLC

6.1 Introduction

Connectivity is a key component for the practical implementation of vehicular VLC. Consequently, relay-assisted links have been proposed to extend the communication span in OWC links as in [97-103] and discussed in Chapter 2. Also, in [107], the use of relay-assisted links was proposed to address the vehicular VLC mobility issue where a LOS link to the desired vehicle is not possible but could be achieved through a relay vehicle. Thus, this chapter presents the investigation of a vehicular VLC relay-assisted link under realistic sunlight noise, where the utilization of AF and DF relaying schemes with the same system parameters are analysed. Also, the effect of the relay vehicle's orientation in relation to the source vehicle is examined. Note, in VLC systems using a combination of an imaging lens and PDs to increase the received optical power density, the link will experience beam spot offset (BSO) (i.e., an offset in the projected beam spot from the centre of the focal plane away from the PD, similar to the pointing errors in free space optics), when there is a misalignment between the Tx and the Rx. This can occur due to non-stationary vehicles positions and the different design positioning of TLs (Txs) and Rxs on different vehicles depending on the vehicle's size, brand and model resulting in considerable power losses or a complete shutdown of the communication link. The contributions of the work carried out in this

Chapter are summarized as follows: (*i*) investigation of relay-assisted vehicular VLC links with AF and DF relay schemes; (*ii*) investigation and providing insights on the effect of misalignment between vehicle's Txs and Rxs in real road conditions, which is carried out for the first time; (*iii*) mitigation of the misalignment issue considering typical vehicular geometry parameters; and (*iv*) providing insights to the impact of various parameters such as the PD size, incidence angle and L_s, on the performance of relay-assisted vehicular VLC. This chapter is organized as follows, first relay-assisted vehicular VLC is discussed, next the system model and setup are presented. Subsequently, the results of the performance analysis of the AF and DF vehicular VLC links are presented under varying system parameters and geometry. An experimental demonstration of a relay-assisted link is also described and finally the summary is given.

6.2 Relay-Assisted Vehicular VLC

As highlighted in Chapter 2, there are only few reports on relay-assisted vehicular VLC links. In [100], the viability of VLC using multiple TLs Txs and PD-based Rxs for direct transmission (DT) and multi-hop transmission was reported. It was demonstrated that, spatial multiplexing multi-hop transmission offered reduced average signal power of -59 dBm for a single hop (i.e., L_s of 16 m) compared with -27 dBm for DT (i.e., L_s of 12 m). In [100], it was proposed that vehicles act as relay nodes to forward information to other desired vehicles, but with no investigations on relaying schemes being reported. Thus, in this Chapter, practical scenarios are considered, such as (*i*) a realistic outdoor ambient condition, which is obtained from empirical measurements; (*ii*) different angular communication geometries considering the road lane width, vehicle width and the positions of the Txs and Rxs on the vehicle; and (*iii*) realistic inter-vehicle distance and system parameters.

Notably, communications in a vehicular environment using light communications technology include V2V, V2I, V2D, and V2R. Note that, the DF scheme is most appropriate for vehicular communications as the information received by a vehicle will need to be decoded first prior to being forwarded to the next or other vehicles. Depending on the scenario, using the DF scheme communications can be established between two or more vehicles. Whereas in the AF scheme, where road/traffic infrastructures e.g., traffic lights, advertising boards, etc. are used as static relay nodes for forwarding information to vehicles/other road infrastructures within the coverage area.

6.3 System Model

For the LOS transmission mode, the received signal can be expressed as [84]:

$$y(t) = \mathcal{R}x(t) \otimes h(t) + n(t), \tag{6.1}$$

where $h(t)$ is the channel impulse response, $x(t)$ is the transmit signal, and $n(t)$ is the additive white Gaussian noise including the sunlight induced shot noise source, thermal noise, signal dependent and dark current noises with noise variances denoted as σ^2_{amb}, $\sigma^2_{\text{thermal}}$, $\sigma^2_{\text{shot-rs}}$, and σ^2_{dk}, respectively.

The channel DC gain when an imaging OC (IOC) is used at the Rx can be expressed as:

$$H_{\text{LOS}} = \begin{cases} T_{\text{lens}}(\varphi) T_{\text{filt}}(\varphi) \frac{A_{\text{img}}}{A_{\text{TL}}}, & 0 \le \varphi \le \emptyset_{\text{S-AFOV}} \\ 0, & \varphi > \emptyset_{\text{S-AFOV}} \end{cases}, \tag{6.2}$$

where $T_{\text{filt}}(\varphi)$, and $T_{\text{lens}}(\varphi)$ are transmittance of the OF and OC, respectively. A_{img} represents the area of the projected focused image of the light source by the imaging lens, which is dependent on the focal length f of the lens, the actual area of the light

source A_{TL} within the AFOV of the Rx, and the link span L_s, which can simply be expressed as:

$$A_{\mathrm{img}} = A_{\mathrm{TL}} f^2 / L_s^2. \tag{6.3}$$

Note that, *D* of the lens is taken to be equal to *f* (for (6.2)), i.e., the largest possible lens diameter is considered, as it is well known that, *D* of a glass lens cannot be larger that the *f* [210]. Note that, as *D* gets smaller the light collected by the lens decreases, and hence the received intensity of the projected Tx footprint decreases. Consequently, in such cases the received intensity is proportional to the collecting area of the lens.

When a non-imaging OC (NIOC) is used at the Rx, the LOS channel DC gain with a symmetrical LED radiation pattern (e.g., some LED-based TLs have symmetrical light patterns as measured in Chapter 3) can be expressed as [84]:

$$H_{\mathrm{LOS}} = \begin{cases} \frac{(m+1)A_{\mathrm{PD}}}{2\pi L_s^2} \cos^m(\theta) T_s(\varphi) g(\varphi) \cos(\varphi), & 0 \le \varphi \le \emptyset_{\mathrm{S-AFOV}} \\ 0, & \varphi > \emptyset_{\mathrm{S-AFOV}} \end{cases}, \tag{6.4}$$

where θ denotes the irradiance angle, $\emptyset_{\mathrm{S-AFOV}}$ is the semi- AFOV of the Rx, and L_s is the distance between the Tx and the Rx.

The gain of a non-imaging OC g is $A_{\mathrm{coll}}/A_{\mathrm{PD}}$ [114], where $A_{\mathrm{coll}} = \pi D^2/4$, is the collection area of the non-imaging OC, and *m* represents Lambertian order of the Tx, which is given by [84]:

$$m = -\frac{\ln(2)}{\ln\left(\cos(\theta_{1/2})\right)} \tag{6.5}$$

where $\theta_{1/2}$ is the half power angle. Lambertian radiant intensity is expressed as [84]:

$$R(\theta) = \frac{(m+1)}{2\pi} \cos^m(\theta) \tag{6.6}$$

Note that, the dominant noise source in vehicular VLC, which is the sunlight induced shot noise and other noises such as the thermal noise, signal-dependent shot noise and the PD's dark current noise are all considered in the simulation investigations carried out as given by (3.14)-(3.19), see Chapter 3.

6.4 System Setup

The system schematic block diagrams of the DF and AF relay-assisted vehicular VLC systems are depicted in Figure 6.1(a) and (b), respectively. The proposed schemes are simulated using Monte Carlo model, where different communication geometries and system parameters are considered for the evaluation of the performance of the vehicular VLC link in terms of the BER. A 3×10^5 random bit stream is generated in the NRZ-OOK data format, which is up-sampled (number of samples/bit n_{sam} = 10) prior to transmission over the first channel to the relay node. Note, the emulated sunlight induced noise obtained from empirical measurements is the dominant source in vehicular VLC systems during the daytime, and all other noise sources outlined in Section 3.2.1 are added to the received signal. Note, here we consider non-imaging-based Rx (i.e., a NIOC with a PD) and imaging-based Rx (i.e., an IOC with a PD) systems. The impact of various system parameters on the multi-hop vehicular VLC system is investigated.

At the relay nodes and Rxs, for the non-imaging and imaging-based links NIOCs and IOCs with *D* and *f* of 15 mm are used, respectively (where the transmittance of the IOC is 0.92) while OFs (a wavelength band of 405-690 nm and a transmittance of 0.92) are utilised to improve the SNR. The inter-hop distance is 25 m. For the AF relay link, following transmission over the first channel, the received signal at the relay node is amplified to its original power level prior to retransmission to the next relay node, see Figure 6.1(a). For the DF relay link, the received signal is applied to the matched filter (MF) and decoder prior to packet regeneration. The process of detection is the same as the DF relay nodes and the end user as illustrated in Figure 6.1, where the MF is comprised of an integrator, sampler (with a sampling interval $t_s = n_{\text{sam}}$), and slicer (the threshold level set to the mean value of sampled filtered signal). Next, the signals from

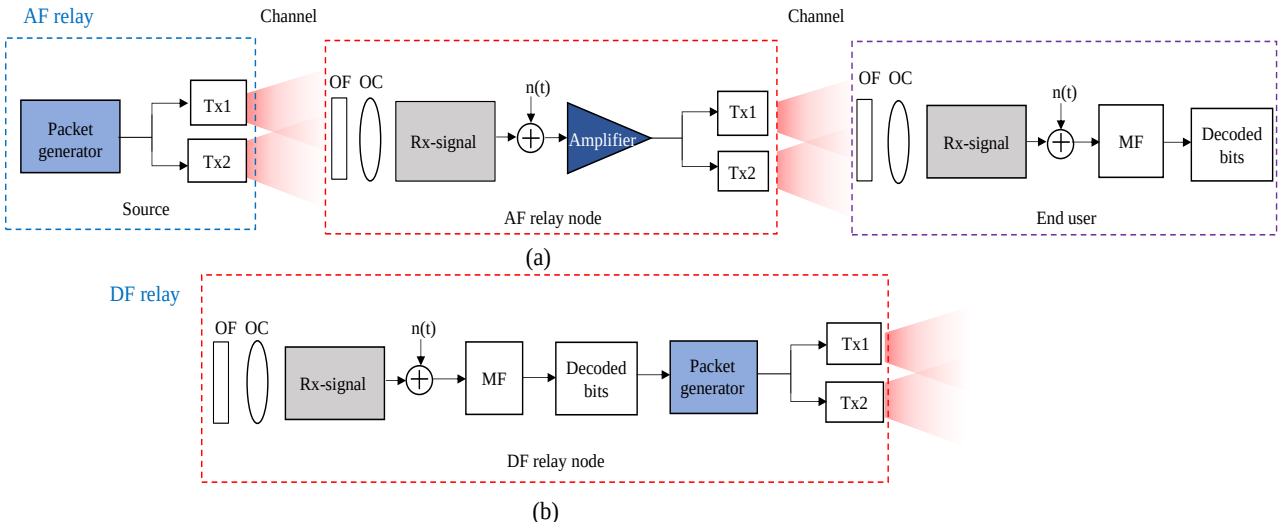

Figure 6.1: System block diagram for the vehicular VLC relay-assisted links with: (a) AF, and (b) DF relay schemes (just relay node shown)

the output of the slicer, that are below the threshold level, are set by the decoder to 0 and otherwise to 1. Note, the target BER in relation to the confidence level (CL) can be calculated from [211]: $\text{Nbits (total bits)} = \frac{-\ln(1-\text{CL})}{\text{BER}}$. At a standard 95 % confidence level (CL=0.95) and a target BER of 10^{-5}, the total bits to be transmitted is obtained as

3×10^5. Hence, 3×10^5 bits were transmitted and the BER floor level was set to 10^{-5} (i.e., BER less or equal to 10^{-5} was set to 10^{-5}).

The key simulation parameters are listed in Table 6.1 and other specific system parameters used are stated for each result presented.

Table 6.1: Key system parameters

Parameter	**Value**
Diagonal of PD (Rx) d_{PD}	1 mm
Cumulative link span	125 m
Absolute temperature T_K	298 K
System bandwidth B	5 MHz
Responsivity of PD $\mathcal{R}$	0.43 A/W
Solar irradiance $P_{\mathrm{solar}}(\lambda)$	413.77 W/m^2
Load resistance R_L	50 Ohms
Maximum PD dark current I_{dc}	5 nA
Transmission coefficient of OF T_{filt}	0.92
Transmission coefficient of IOC T_{lens}	0.92
Focal length of IOCs f	15- 50 mm
Half power angle of Tx $\theta_{1/2}$	30-70$^{\mathrm{o}}$
Transmit power P_T	1.25 W
NIOC's diameter D	15 mm
Distance between Tx1 & Tx2 w_{Tx}	1.2 m

6.5 Performance Analysis of the Relay-Assisted Vehicular VLC Link

Firstly, Figure 6.2 illustrates the BER performance of a vehicular VLC link as a function of the communications span: (*i*) without the use of intermediate relay nodes (i.e., DT); (*ii*) with the use of relay links employing DF and AF relaying schemes; and (*iii*) with and without the use of a MF at the Rx for (*i*) and (*ii*). The Tx1 and the NIOC Rx1 are aligned with D = 15 mm and $\theta_{1/2}$= 45$^{\mathrm{o}}$.

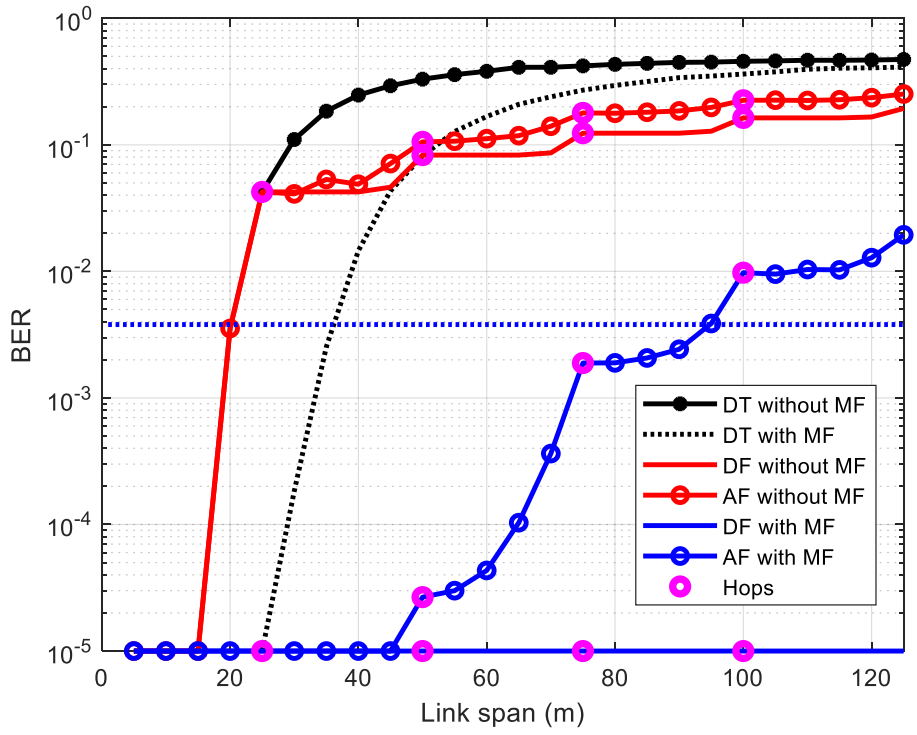

Figure 6.2: BER performance of a vehicular VLC link as a function of link span with and without relays and MF

It can be observed that, with MF, there is significant BER performance improvement. E.g., for the DT, AF, and DF links, at the FEC BER limit of 3.8×10^{-3} the achieved link span without MF is 20 m for each link, which significantly improves to 36, 95, and >125 m for DT, AF, and DF links, respectively using the MF. It is noteworthy that, immediately after each relay node, the BER performance trend improves i.e., lower BER degradation with the increasing link span since the signal is amplified to its original power level at the relay node.

6.5.1 Non-imaging based vehicular VLC links

For the vehicular VLC link with the non-imaging- based Rx, the image of the Tx is not formed at the Rx as in imaging links and the radiation pattern of the Tx determines the achievable link span and the coverage area. Hence, Figures. 6.3 and 6.4 illustrates the impact of the radiation pattern (in terms of $\theta_{1/2}$) on the multi-hop vehicular VLC link. As shown in Figures 6.3 and 6.4 (for alignment conditions), the BER performance improves with decreasing $\theta_{1/2}$ for the DF and AF relay schemes. Besides, the BER performance of the DF link shows a better trend than the AF for the same system parameters used i.e., a slower rate of BER degradation than the AF. For instance, for $\theta_{1/2}$ of 30, 40, 50, and 60^{o} at the FEC BER limit, the achieved link spans for the AF and DF are >125, 98, 49, 40; and >125, >125, >125, and 49 m, respectively. Note that, the BER degradation trend of both the AF and DF links changes (improves) immediately after each relay node (hop) since the signal is amplified/reset to its original power level at each hop before retransmission to the next hop.

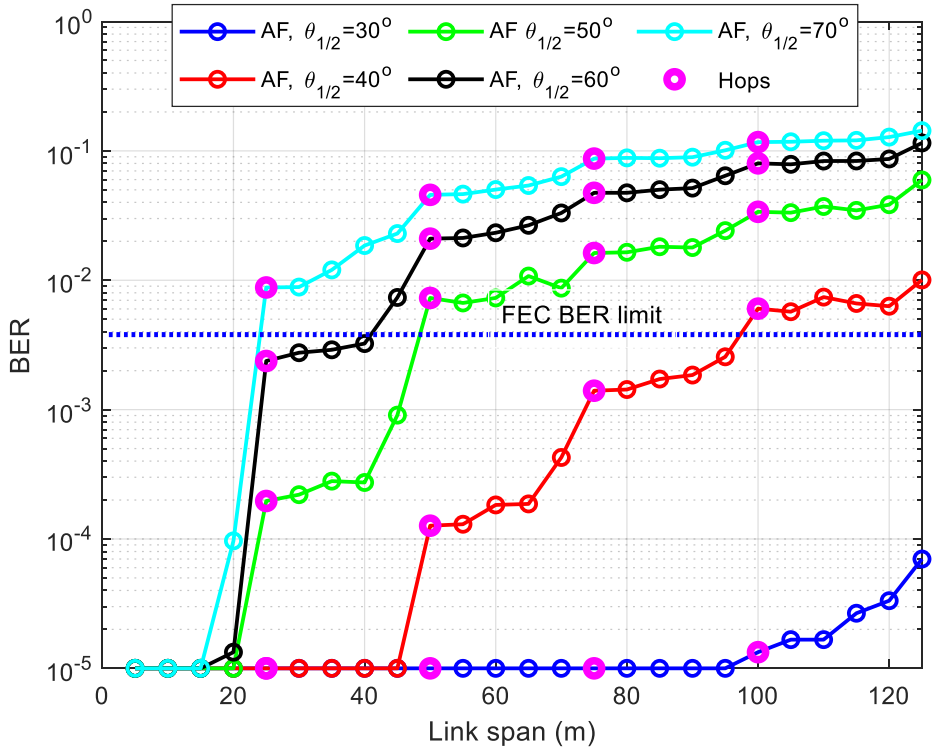

Figure 6.3: The BER performance of the AF relay-assisted as a function of link span

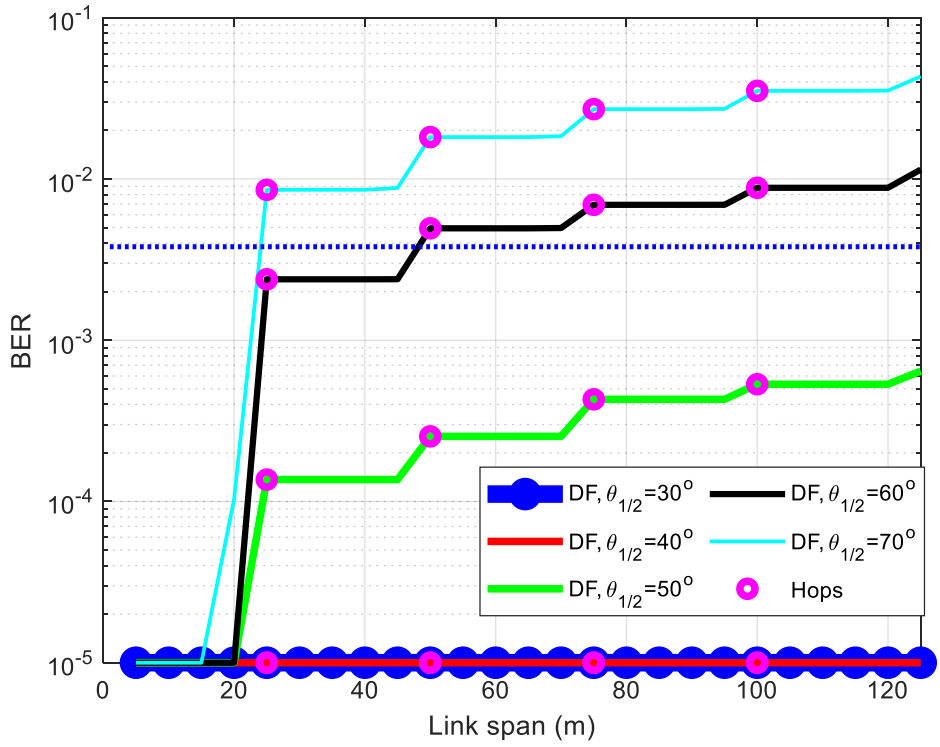

Figure 6.4: The BER performance of the DF relay-assisted vehicular VLC link

6.5.2 The imaging-based vehicular VLC link

Notably, in vehicular VLC links with and without relay nodes, maintaining the exact alignment between the Rx and the Tx may not possible due to the movement of vehicles, which results in changes in the incidence angles at the Rx, see Figure 6.5. Therefore, the link utilising an imaging lens at Rx will experience BSOs in the horizontal, vertical or both directions on the focal plane as shown in Figure 6.6.

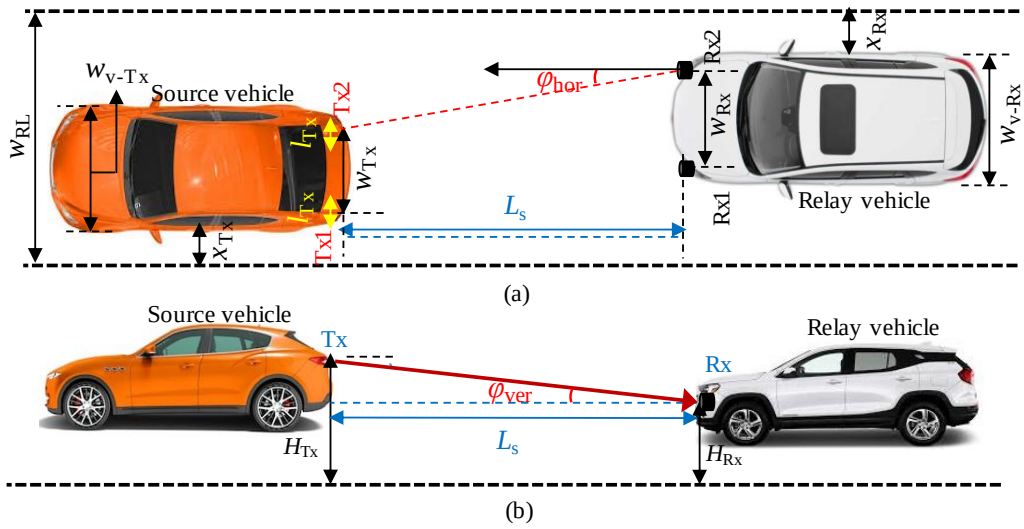

Figure 6.5: vehicular VLC configuration: (a) top view showing Tx-Rx horizontal incidence angle, and (b) side view showing Tx-Rx vertical incidence angle

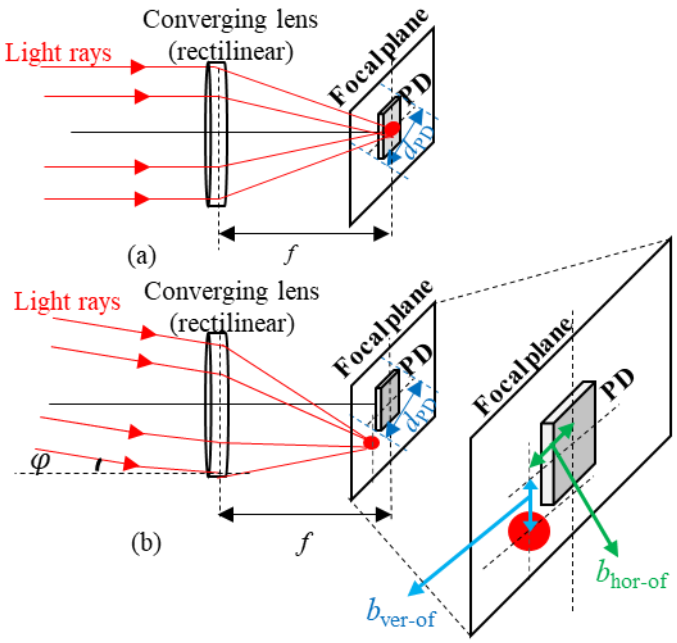

Figure 6.6: (a) Parallel, and (b) non-parallel light beams through a converging lens

The horizontal incidence angle for at least a Tx to be captured for a road lane width w_{RL} is given by:

$$\varphi_{\text{hor}} = \arctan\left(\left(w_{\text{RL}} - \left(\frac{w_{\text{v-Tx}} - w_{\text{Tx}}}{2}\right) - \left(\frac{w_{\text{v-Rx}} - w_{\text{Rx}}}{2}\right) - \left(w_{\text{Tx}} - \frac{l_{\text{Tx}}}{2}\right) - x_{\text{Rx}} - x_{\text{Tx}}\right)/L_s\right), \tag{6.7}$$

where w_{Rx}, w_{Tx}, $w_{\text{v-Rx}}$, $w_{\text{v-Tx}}$, l_{Tx}, x_{Rx}, x_{Tx} are the distance between the centres of Rxs 1 and 2 and Txs 1 and 2, widths of the Rx and the Tx vehicles, length of the Tx, and distance of the Rx and the Tx vehicles from the edge of road lane, respectively. The maximum BSOs in terms of φ and f of the lens on the focal plane at the PD's surface using a converging rectilinear lens at the Rx side is given as:

$$b_{\text{of}} = f\tan(\varphi), \tag{6.8}$$

$$b_{\text{of}} = \begin{cases} b_{\text{hor-of}} & \varphi = \varphi_{\text{hor}} \\ b_{\text{ver-of}} & \varphi = \varphi_{\text{ver}} = \arctan((\Delta H)/L_s), \end{cases} \tag{6.9}$$

where φ_{ver} is the vertical incidence angle, $b_{\text{ver}-\text{of}}$ and $b_{\text{hor}-\text{of}}$ are the vertical and horizontal BSOs on the focal plane, respectively and the offset between the Rx's and the Tx's vertical heights $\Delta H = |H_{\text{Tx}} - H_{\text{Rx}}|$. Using (6.8)-(6.9) and with $w_{\text{Rx}} = w_{\text{Tx}}$= 1.2 m, $w_{\text{v}-\text{Rx}} = w_{\text{v}-\text{Tx}}$ = 1.7 m, and $L_s \geq 2$ m the maximum φ_{hor} (i.e., the worst case scenario for inter-vehicle communications at the opposite edge of the road lane) for $w_{\text{RL}}$of 2.5 and 3.75 m (which are the minimum and maximum w_{RL} for a lane) are 21.8 and 45.7°, respectively, and the maximum φ_{ver} for ΔH = 0.5 m for $L_s \geq 2$ m is 14°. Thus, Figure 6.7(a) displays the plots of BSO as a function of the incidence angle for a range of *f*, showing that BSO exponentially increases with the incidence angle for all values of *f*. For example, for *f* = 50 mm, BSO increases from 4.37 to 18.2 mm, i.e., about 4 times for φ increasing from 5 to 20°. Note, this BSO values highlighted in the latter are orders of magnitude larger than the diagonal width d_{PD} of a high-speed PD (e.g., 0.1 mm). It is note worthy that, the AFOV of VLC depends on *f* of the lens and the size of the PD as also described in Chapter 3 and depicted in Figure 6.7(b). The width of the projected focused Tx's image on the focal plane (i.e., the beam spot size (BSZ)) in terms of the Tx's diagonal widths d_{Tx} is given as:

$$d_{\text{BSZ}} = d_{\text{Tx}} f / L_s. \tag{6.10}$$

Consequently, the size of Tx's beam spot is a critical factor in considering BSZ- and BSO-induced power losses at the PD, see Figure 6.8, which shows BSZ as a function of the link span for a range of *f* and d_{Tx} . As illustrated, BSZ plots exponentially drop with L_s for all values of d_{Tx} and increases with *f*, reaching < 2 mm at L_s > 10 m and converging to < 1 mm for L_s of 25 m. Note, for shorter L_s, BSZ is orders of magnitudes larger than at longer L_s and thus, the performance of the link is not degraded due to BSO provided the PD size is larger than BSO and it captures the entire BSZ.

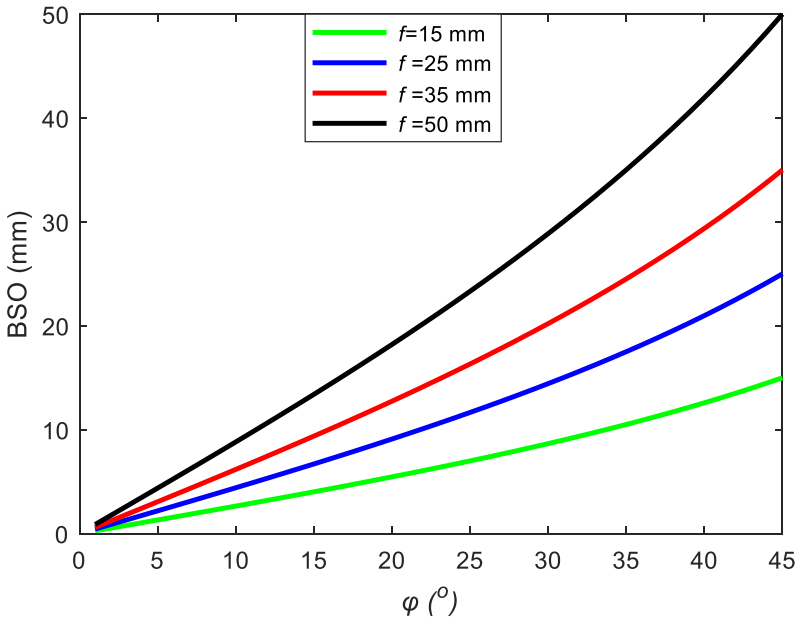

(a)

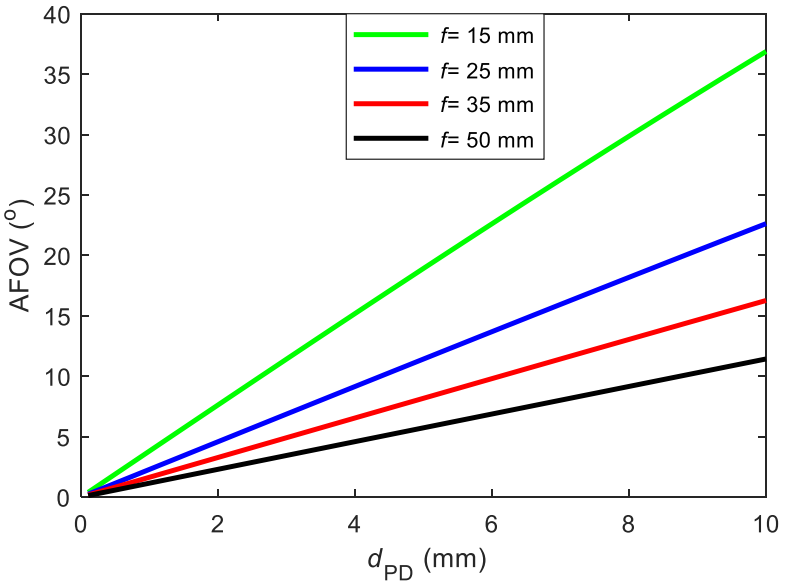

(b)

Figure 6.7: (a) BSO as a function of φ, and (b) AFOV as a function of d_{PD} for a range of f

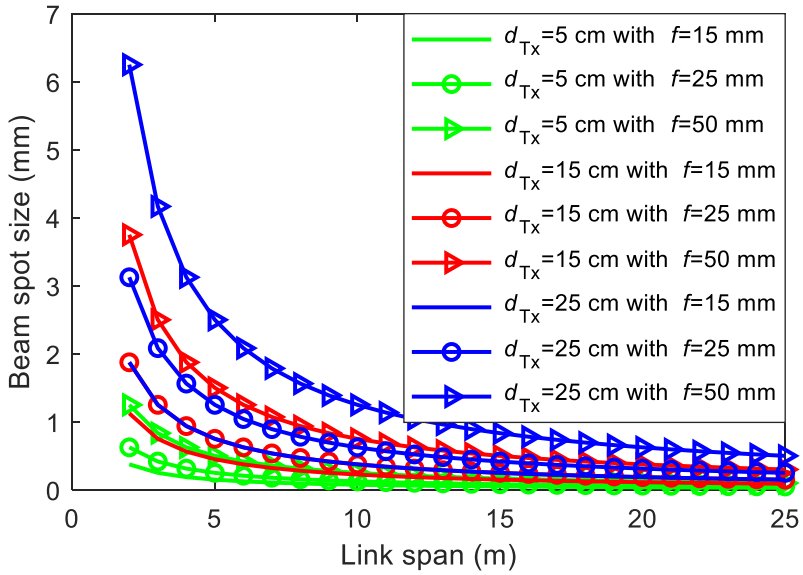

Figure 6.8: Beam spot size at the focal plane as a function of link span for a range of d_{Tx} and f

For instance, at f of 50 mm, d_{Tx}= 15 cm, and at L_s of 5 and 20 m BSZs are 1.5 and 0.38 mm, respectively. Note, larger size PDs can be used, since the data transmission rate is relatively lower in vehicular VLC [212] compared with indoor short range links. Notably, when an imaging lens is used in front of a PD, the image of the Tx is formed at the Rx just as in a camera. However, the size of f is an important parameter that determines AFOV and the size of the Tx image projected onto the PD. Consequently, the impact of f on the BER performance of the imaging-based Rx for alignment conditions is shown in Figure 6.9 for a multi-hop link with AF and DF schemes.

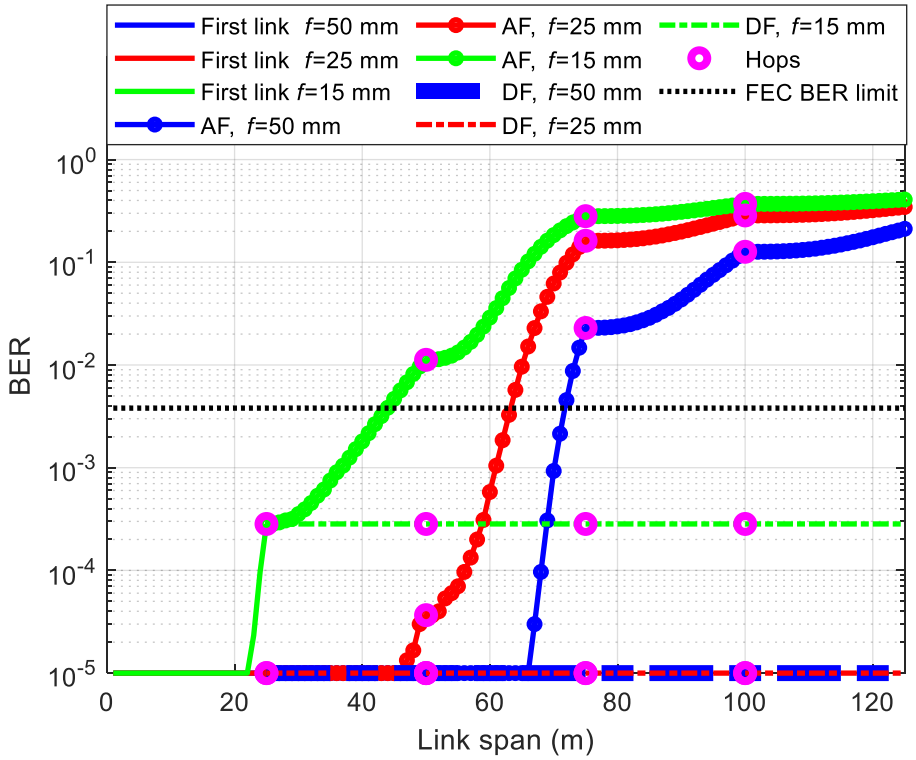

Figure 6.9: The BER performance as a function of the link span for AF and DF relay imaging Rx- based link and for a range of *f* (alignment condition)

As shown in Figure 6.9, for AF relay links, the BER performance degrades with the increasing link span, however, the degradation trend improves following each relay over a given distance. Also, the BER performance improves with higher values of *f* due to the larger BSZ (i.e., larger projected footprint of the light source onto the PD), thus translating to larger optical power densities at the Rx. For the DF relay, links with *f* of 25 and 50 mm maintain error free communications up till the end of the transmission link. Thus, demonstrating that the BER performance of the DF relay-assisted multi-hop links can be maintained over several hops provided the signal quality does not degrade beyond a certain level on reaching the relay node prior to retransmission.

The BER versus L_s for a range of P_T is shown in Figure 6.10, where f = 15 mm, and Txs and Rxs are in alignment with the diagonal widths d_{Tx} and d_{PD} of 5 cm and 1 mm, respectively. As presented in Figure 6.10, the BER performance improves with increasing P_T dropping by up to 68 and 89 % for a 0.25 W increase in P_T (i.e., 0.75 to 1 W and 1 to 1.25 W) for the AF and DF links, respectively at the end of the 2nd channel. For comparison, at the FEC BER limit, P_{solar} of 413.77 W/m^2 (as described in Chapter 3) and P_T of 0.75 W, link spans of up to 66 and 21 m are achieved for the cases without and with the sunlight noise (i.e., no σ^2_{amb}), respectively. Besides, at the end of the 2nd

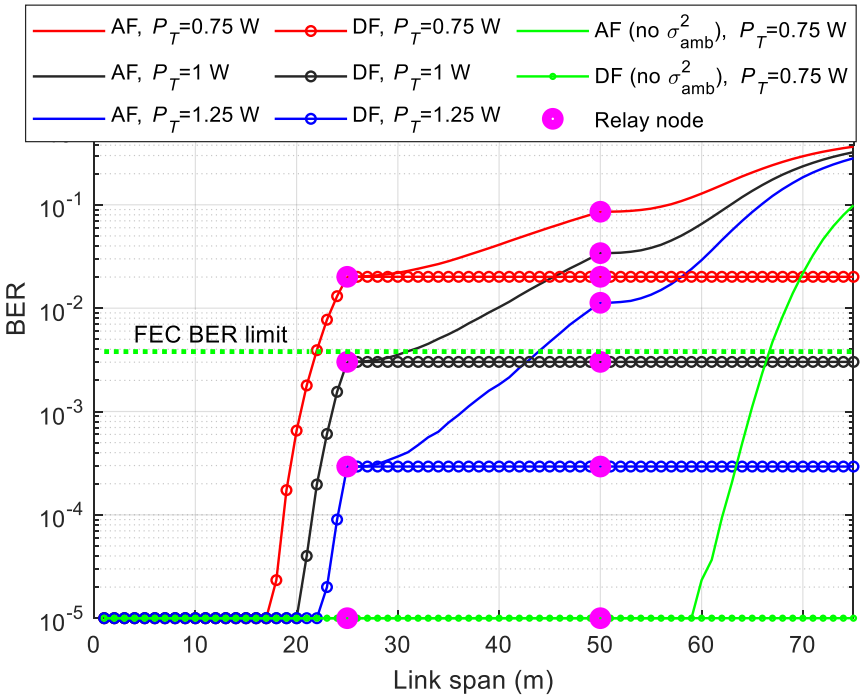

Figure 6.10: BER performances for a range of P_T as a function of the link span

hop and at the FEC BER limit (for P_T = 1 W) the achieved L_s is 150 % higher for DF compared with AF under the emulated sunlight noise. The reason for this is that, in an AF relay-based link the system performance is affected more by the noise accumulation over the transmission span since the signal received at the relay node is simply amplified with no regeneration or reshaping in contrast to the DF. Figure 6.11 shows examples of the eye diagrams of the received signal (for the first 10^3 bits received) for the link with

aligned Txs and Rxs with f =25 mm, P_T = 1.25 W, and inter-hop distance of 25 m. It is noticeable that, the heights and widths of the eye opening for the AF link decrease continuously from one hop to the next with the worst-case scenario being at the end of the 4th hop, where the eye opening is almost closed. However, for the DF link the heights and widths of the eyes are well open and this is maintained even up to the end of the 4th hop.

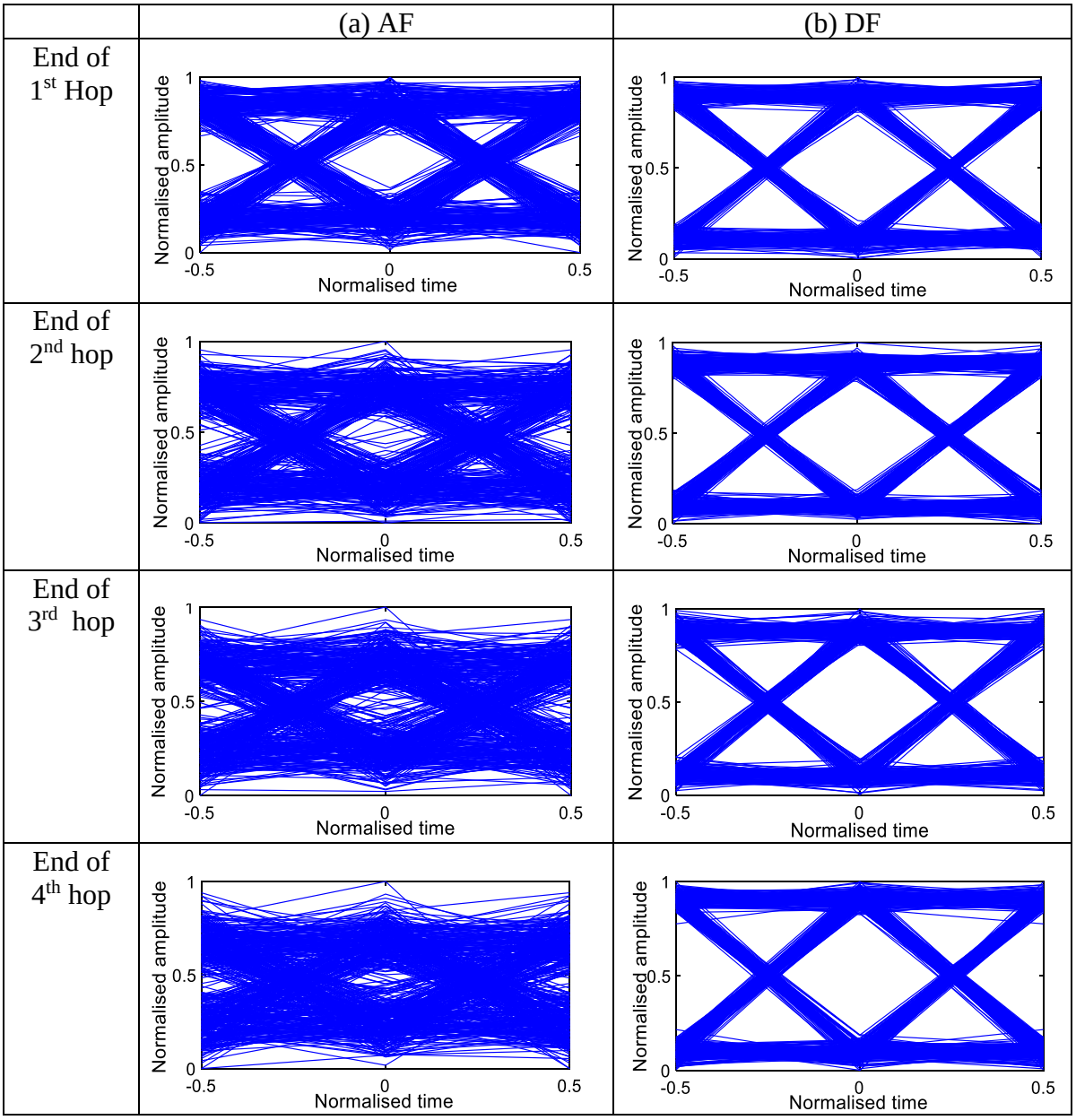

Figure 6.11: Examples of eye diagrams of received signals for the vehicular VLC link at the end of the 1st hop to 4th hop for: (a) AF, and (b) DF schemes

Additionally, for the first time the effect of the orientation of the relay vehicle with respect to the source vehicle considering BSO due to φ on the BER performance at the relay node is investigated. The system parameters used are d_{Tx} =5 cm, and P_T = 1.25 W. Notably, for same vertical/horizontal misalignment offset distance on the road between the Rx and the Tx, φ will be higher for shorter L_s. Figures 6.12 (a) and (b) depicts the BER as a function of φ_1 (i.e., the angle of incidence with respect to the Tx1

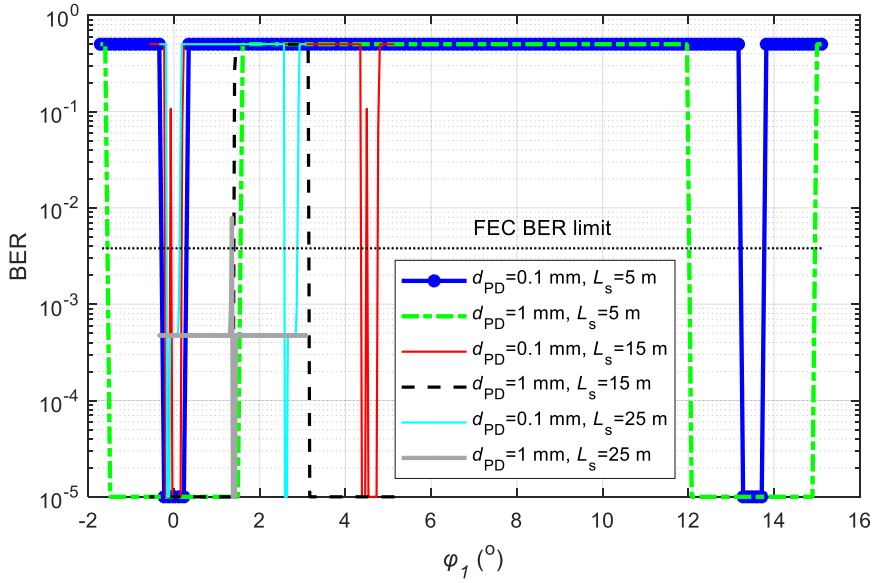

(a)

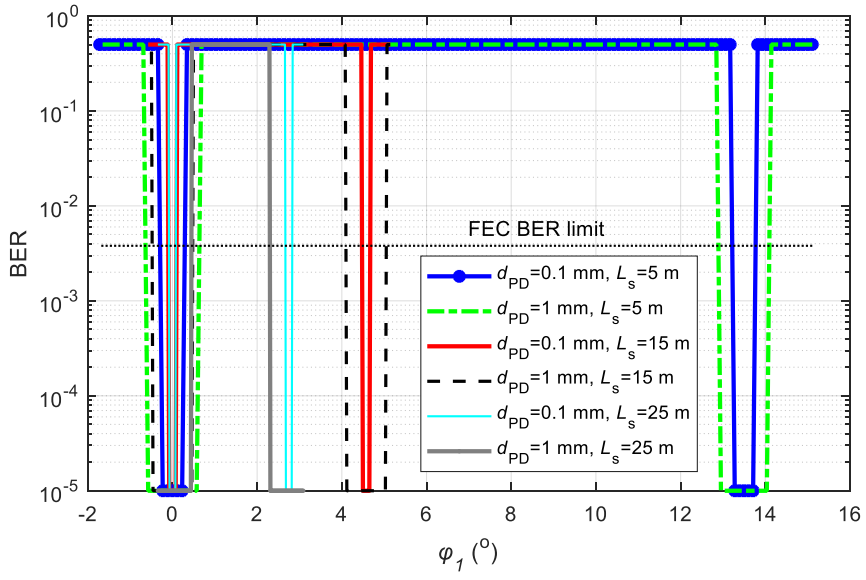

(b)

Figure 6.12: BER degradation as a function of φ_1 for a range of d_{PD} and L_s: (a) f = 15 mm, and (b) f = 50 mm

and the Rx1 (using the configuration in Figure 6.5), which will be the same for the Tx2 with respect to the Rx2) with *f* of 15 and 50 mm, respectively for a range of L_s and d_{PD}. The key geometry and simulation parameters are given in Table 6.2.

Table 6.2: Key geometry parameters and simulation values

Parameter	**Value**
Distance between Tx1 & Tx2 w_{Tx}	1.2 m
Distance between Rx1 & Rx2 w_{Rx}	1.2 m
Width of Rx vehicle $w_{\mathrm{v-Rx}}$	1.7 m
Width of Tx vehicle $w_{\mathrm{v-Tx}}$	1.7 m
Diagonal width of Txs d_{Tx}	5 cm
Distance between source and relay vehicle	5-25 m
Horizontal misalignment distance between Tx and Rx	0-0.75 m
Focal lengths of IOC f	15 &50 mm
PD's diagonal width d_{PD}	0.1 &1 mm

The centre of the road lane is considered as the origin of the Cartesian and spherical coordinate systems for calculating the positions of the Tx and the Rx, and incidence angles, where φ_1 values to the left and right of the road lane are positive and negative, respectively. Besides, the system performance is highly dependent on the geometry of the Rx and the Tx. Also, it can be noticed that the Rx with a larger d_{PD} and lower *f* of lens value allows higher degrees of misalignment i.e., larger φ_1. At certain values of φ_1 the BER tends to 0.5 as the Tx's footprint or the beam spot from the lens is not captured by the PD. At certain values of φ_1 and L_s the following capture scenarios are possible (*i*) both Txs; (*ii*) one Tx only; (*iii*) part of the Tx(s); and (*iv*) none of the Txs's beam spot are captured by the PD.

It is worth noting that, the BER plot showing step responses i.e., rapid degradation due to φ_1 resulting from BSO. This is because of the projected beam spot not being incident on the PD and therefore the link is lost and hence a higher BER. With an imaging lens employed at the Rx side an image of the Tx is formed, which is projected to the Rx plane (just as in a camera). Importantly, the size of the projected image (i.e., BSZ represented by d_{BSZ}) is dependent on *f*, the original size of the Tx d_{Tx}, and L_s as given in (6.10). For example, considering a Tx with a diagonal width d_{Tx} = 5 cm, *f*=15 mm, and L_s= 25 m the size of the beam spot i.e., BSZ at the Rx plane is 0.03 mm. Using a high-speed small area PD with d_{PD} of 0.1 mm (for example), depending on the degree of misalignment (i.e., depicted by φ_1), with a very small BSZ the BER performance is degraded sharply when the projected beam spot is not illuminating the small area PD due to slight misalignments between the Tx and the Rx.

Consequently, to minimize/overcome this effect, a spherical PD array Rx is proposed to provide a range of varying angular PD orientations with respect to the Tx with an azimuth and elevation curvature deflection angles of 91.4 $^{\mathrm{o}}$ (i.e. to cover φ_{hor} value of 45.7$^{\mathrm{o}}$ to the right or left) and 28$^{\mathrm{o}}$ (for coverage of φ_{ver} value of 14$^{\mathrm{o}}$ to the top or bottom) considering a minimum L_s of 2 m, ΔH= 0.5 m, and w_{RL}= 3.75 m, which is the largest width for the single road lanes. Note, with this method lower values of φ can be achieved using a spherical PD array, as lower φ results in reduced BSO, see Figure 6.7(a), and consequently a minimum BER degradation.

6.5.3 Multi-hop routing

Usually, to send a message from a source to a target/end user, the best path of propagation is always the highly sort for, hence a number of schemes have been proposed for selecting the best path for routing messages in vehicular ad hoc networks (VANETs). In [213], a new dynamic routing protocol (DYRP) was developed to

generate alternative routes for vehicular VLC networks without the requirement of prior knowledge of the topology. With the proposed DYRP, vehicular VLC systems are able to construct wireless ad-hoc networks and adapt to dynamic changes in the communications network, such as shadowing and obstacles. Results obtained showed that a multi-hop vehicular VLC link with obstacles can still achieve up to ~39 % of its original data rate when a LOS link is available between the communicating vehicles. However, the scenarios investigated did not show that a vehicular environment topography or the road lane parameters were considered, which is the key to achieving a realistic routing protocol for vehicular VLC networks. In [214], a tree-based network architecture for vehicular VLC providing a rapid connection and allowing an extended network coverage beyond the area covered by lighting gateways was investigated. Particularly, a quality of service (QoS) oriented VANET architecture, which works based on a distributed and real time computation of QoS metrics for multimedia services, was proposed. Also, in [215] a cross layer optimized routing protocol (VL-ROUTE) was proposed that cooperated with the medium access control layer, which considered the reliability of the routes to maximize the throughput of the network. To achieve this, a route reliability score metric was formulated that can be computed by each network node using information obtained from its immediate neighbours. Results obtained for VL-ROUTE showed a 124 % improvement in the network throughput compared with a network using carrier sense multiple access/collision avoidance along with shortest path routing.

Importantly, it is worthy of note, that the topology of the vehicular network is characterized by an uneven distribution of vehicles and high node mobility (i.e., vehicles) [216]. Moreover, there are limited communication links between the nodes due to the constraints imposed by the topology of the vehicular environment (i.e., road lanes)

[217]. Furthermore, to develop appropriate routing protocols for the vehicular VLC technology, the transmission modes (i.e., LOS, NLOS or both), practical road lane widths, and topography should be considered and investigated. Hence, to provide more insights, multi-hop vehicular links considering three routes (i.e., three road lanes) for the propagation of a broadcast message are investigated. Notably, the position of vehicles on the road is simulated, with vehicles randomly positioned within a 100 m link span. Also considered are practical road lane, vehicle widths, misalignment, and the positions of the Tx and the Rx on the forwarding and receiving vehicles. Figure 6.13 shows the simulated vehicular VLC link topology, where the first vehicle on the centre lane is designated as the source vehicle attempting to send a broadcast message to other vehicles in its vicinity. Results are shown in Figure 6.14 (a) and (b) for the BER performance for the three routes investigated using the DF scheme. As can be noticed, with a PD diagonal width of 1 mm and *f* of 15 mm, the source vehicle is able to communicate only with the vehicle on the same lane (i.e., route 3), while the nearest vehicle on the other two lanes

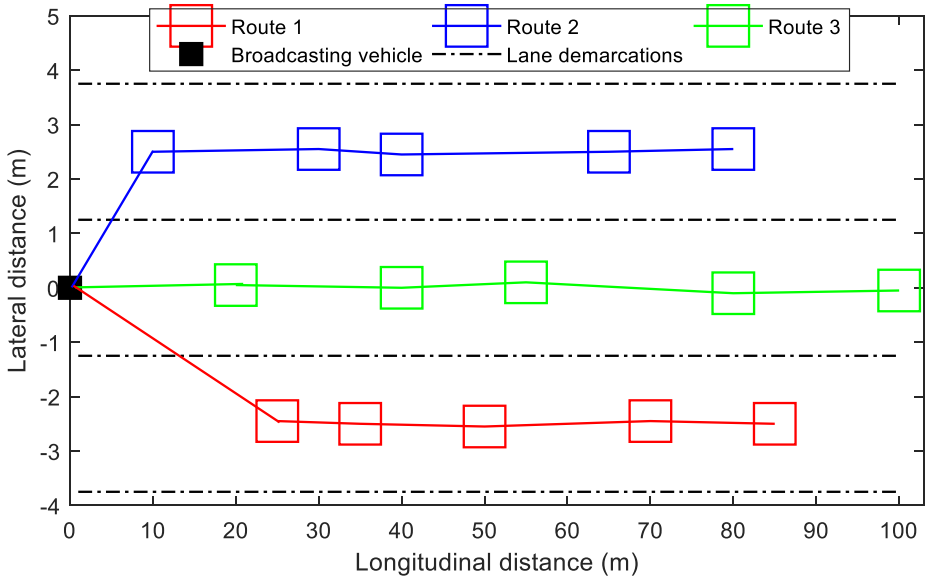

Figure 6.13: The simulated vehicular VLC topology illustrating possible packet transmission routes

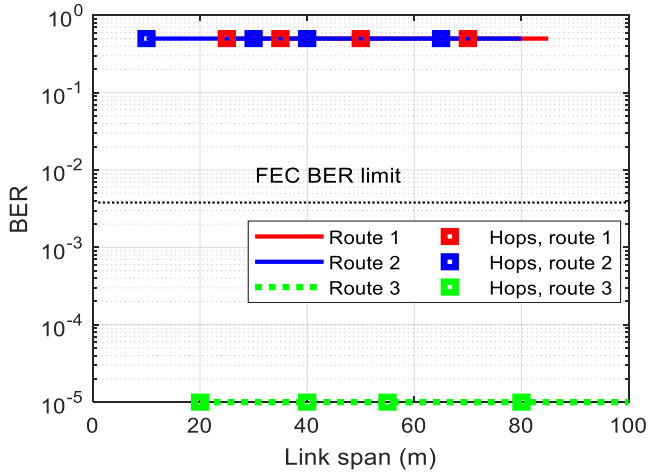

(a)

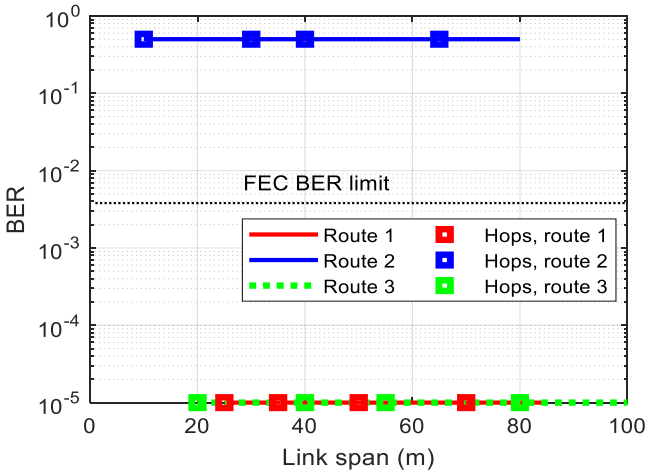

(b)

Figure 6.14: The BER performance for the scenarios in Figure 6.13 for d_{PD} of: (a) 1 mm, and (b) 5 mm

are not able to receive the message because the incidence angle is outside their AFOV. With d_{PD} increasined from 1 to 5 mm one more route becomes active in receiving forwarded messages from the source vehicle. Notably, there is a sharper incidence angle at the first hop (with respect to the broadcasting vehicle) for route 2 than route 1, due to the shorter link span. Importantly, the results have also revealed that, the shortest propagation path may not be the best path of choice as the shortest route would be route

1, hence vehicular VLC routing algorithms should also adequately take into consideration the system's AFOV in determining the best route path.

6.6 Experimental Demonstration of a Relay-Assisted Vehicular VLC Link in a Laboratory Environment

An experimental demonstration of a relay-assisted link with AF and DF schemes is also carried out and described as follows:

6.6.1 Experimental setup

The schematic block diagrams of the proposed AF and DF relay-assisted VLC system are shown in Figure 6.15 (a) and (b), respectively. At the Tx, a NRZ-OOK data stream of 10^4 bits is generated using an arbitrary waveform generator (AWG) (Teledyne T3AWG3252), the output of which is used for intensity modulation of the Tx1 via the

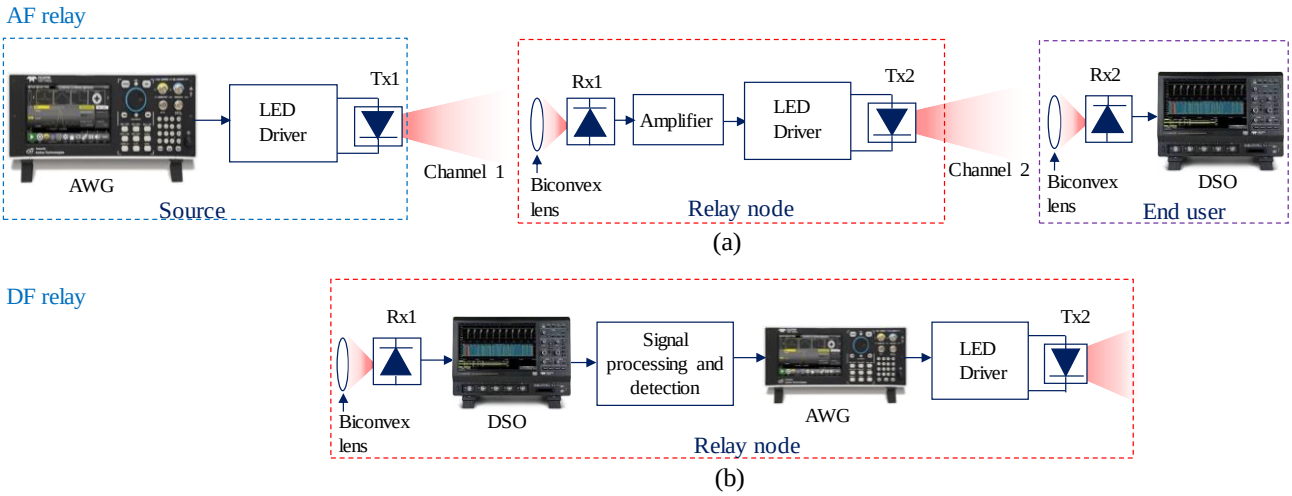

Figure 6.15: Experimental setup for the vehicular VLC relay-assisted links with: (a) AF, and (b) DF relay schemes (just relay node shown)

LED drivers with the drive current of 0.96 A. Following transmission over the free space and optical-to-electrical and electrical-to-optical conversion in the AF-based relay node and decoding in the DF-based relay node the signals are transmitted over the 2nd free space channel to the Rx2. The output of the Rx2 is captured using a real-time digital signal oscilloscope (DSO) (LeCroy WaveRunner Z640i) for offline processing in MATLAB. Note, a vehicle TL (Truck-trailer DACA08712AM), Thorlabs APD430A2/M (silicon-based avalanche PD), Thorlabs PDA10A2 and Texas Instrument THS3202 are used as the Txs, Rx1, Rx2, and amplifier, respectively. Note, the relaying schemes are applied following the first channel, i.e., after the Rx1, and the PD type used at the Rx2 for both AF and DF schemes are the same. Biconvex lenses with the focal length of 35 mm are used at the Rxs to improve the SNR. Key experimental system parameters are listed in Table 6.3.

Table 6.3: Key experimental system parameters

Parameter	**Value**
Tx bias current at TL 1	0.96 A
Tx peak wavelength	630 nm
Transmit power	32.4 mW
Tx data	10^4 bits
Inter link distance	8 m
Biconvex lenses focal length at Rxs	35 mm
Detector's active area diameter of PD 1 (APD430A2)	0.2 mm
Minimum noise equivalent power (DC-100 MHz)	0.15×10^{-12} W$\sqrt{\text{Hz}}$
Operating wavelength of PD 1	200 – 1000 nm
Detector's active area diameter of PD 2 (PDA10A2)	1.0 mm
Operating wavelength of PD 2	200 – 1100 nm
Noise equivalent power @ 730 nm	2.92×10^{-11} W$\sqrt{\text{Hz}}$

6.6.2 Experimental results

The eye diagrams following processing and detection of the captured signals at the Rx2, for L_s of 12 and 16 m for the AF and DF relay-based links at data rates R_b of 250 kb/s are shown in Figure 6.16. Note that, L_s are 8, and 8 to 16 m for the Tx1-Rx1 and Tx2-Rx2, respectively. For the link with the AF relay, see Figure 6.16 (c), and L_s of 16 m the eye diagram is completely closed with the BER of 1.31×10^{-2}, which is above the FEC BER limit of 3.8×10^{-3}. For DF, see Figure 6.16 (d), for the same L_s and R_b as in AF, the BER is below the target value. This is because, in an AF relay-based link the system performance is affected more by noise accumulation over the transmission span since the received signal at the relay node is simply amplified with no regeneration or reshaping in contrast to the DF relay. Note, the modulating signal amplitude was lower at the AF relay node than at the Tx1 due to the limited gain of the amplifier. Thus, even lower BER could be demonstrated using amplifiers with higher gains at the relay node. For the DF relay node-based link, see Figure 6.16 (b), (d), and (f) the eye openings are wide with the BER values below the FEC BER limit. For both relay schemes, the eye-opening decreases with the increasing data rate.

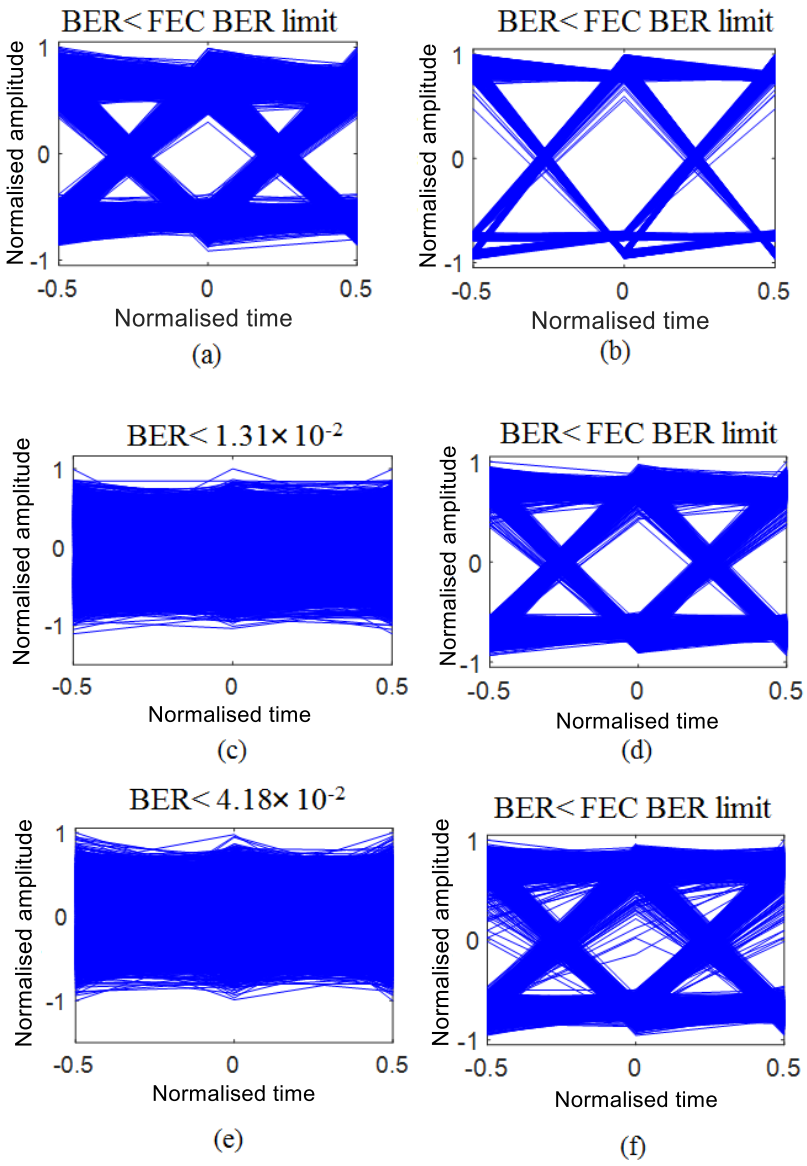

Figure 6.16: Measured eye diagrams for R_b of 250 kb/s for: (a) AF and (b) DF for L_s of 12 m, and (c) AF and (d) DF for L_s of 16 m; and R_b of 500 kb/s for: (e) AF and (f) DF with L_s of 16 m

6.7 Summary

Vehicular VLC links with DF and AF relaying schemes were investigated and results presented, which showed that the DF is a potential option for vehicular VLC providing up to 150 % increment in the achievable link distance than AF at the FEC BER limit by the end of the 2nd hop under emulated sunlight noise. Furthermore, the effect of misalignment between vehicles in real road conditions resulting to beam spot offset for imaging-based Rx links was investigated for the first time. Results showed sharp BER degradation at certain incidence angles, but with the improved by increasing the PD's size. Consequently, to mitigate this effect, the use of a spherical multi-PD array Rx was proposed with the following merits (*i*) provision of a range of varying PD angular orientations that can minimise the misalignment offset angle; and (*ii*) a multi-PD array providing a larger surface area (like a camera-based Rx with several PDs) compared to a single PD-based Rx. Also, insights were provided into the impact of various system parameters on the relay-assisted links. A realistic vehicular VLC link topology with three possible packet transmission routes was simulated, with results showing that the shortest path may not necessarily be the best path and other key factors such as AFOV of the vehicular VLC system needs to be considered to determine the best routes for signal propagation. Finally, experimental demonstration of a relay-assisted link was carried out where the measured BER values for the DF links were all below the FEC BER limit showing that the DF scheme is a suitable candidate for vehicular VLC connectivity as part of ITS.

CHAPTER 7
CONCLUSIONS AND FUTURE WORKS

7.1 Conclusions

This thesis, focused on the topic of vehicular IR/VLC connectivity with single/ multi-hop capabilities by addressing the key challenges and proposing novel technical analytical and experimental solutions. Hence, this work provided insights and a step forward into possible solutions to the major challenges of vehicular VLC links, which are necessary for its implementation in ITS. Firstly, detailed review of vehicular VLC connectivity with respect to the major current challenges in this system, such as increasing the robustness to noise during daytime and under turbulence and fog conditions were given in Chapter 2. Moreover, other major challenges that were also highlighted and discussed were increasing the communication distance and mobility of the vehicular VLC system, which would enable multi-hop links. The relevance of the research work carried out in this thesis were also pointed out in this Chapter in relation to the highlighted major challenges. Furthermore, possible solutions that were proposed from past research works were also discussed. Chapter 3 presented fundamental analysis of vehicular VLC, which included optical characterisation of four different vehicle TLs from popular brands namely, Audi, BMW, Nissan, and a universal truck/trailer/van TL. A link power budget analysis was carried out to ascertain the feasibility of using these TLs as Txs for vehicular VLC for a range of TL irradiance

angles with respect to the vehicle's speeds. Notably, most past works on vehicular VLC were based on the use of a single light module, which may narrow down the conclusions drawn from the results.

Also, most previous works focused more on the use of HL's high or low beam, which have higher transmit powers than TLs and are usually on only at night or when the visibility is low. Note that, the 'always on lights' for HLs, which are always on for some cars during daytime have relatively lower transmit powers than the HL's high or low beam. Notably, only very low link spans (i.e., translating to the driving speeds) of < 10 m were achievable with the TLs investigated. Solar irradiance measurements to obtain realistic values of sunlight induced shot noise was carried out, which is the major source of noise in vehicular VLC systems during the daytime. Other noises degrading the vehicular VLC system were also outlined and considered while investigating the performance of vehicular VLC under different deployment scenarios. Consequently, the inclusion of IR LEDs in HLs and TLs (for PD-based systems) were proposed and for the following reasons (*i*) to meet required transmit power levels (within eye safety limits) needed for longer distance communications; (*ii*) solar irradiance in the IR band is much lower compared with the visible band, leading to improved SNR performance; and (*iii*) it deals with the link asymmetry issue highlighted in Section 2.4.2 since both the HL and TL will have the same Tx characteristics. It was demonstrated that the proposed vehicular IR light link achieved transmission distances of 63, 72, and >89 m at the target FEC BER limit of 3.8×10^{-3}, compared to 4.5, 5.4, and 6.3 m for the BMW vehicle-based TL (which had the highest transmit power) at data rates of 10, 6 and 2 Mbps, respectively under realistic ambient light conditions. Furthermore, insights into the required AFOV for vehicular IR/VLC were also provided and mathematical expressions to calculate this in relation to key parameters such as the positions of the

Tx and Rx on vehicles, lane widths, size of the Tx and the vehicle widths, etc were also given in Chapter 3.

Next, Chapter 4 focused on extending the transmission span of RS-based camera systems. An overview of the merits/applications of OCC and experimental reports on long distance OCC links were outlined where details of the link spans and data rates achieved for the long-distance OCC links so far reported in literature were highlighted. The longest link span achieved for OCC in previous works reported was 328 m at a very low data rate of 15 bps and success transmission rate of 96 %. Importantly, in RS-OCC, it is most desirable for the received signal area on the IS (i.e., the projected image of the Tx on the IS) to be as large as possible, since it determines the number of data rows visible (i.e., the ON and OFF states of the Tx, translating to the achievable data rate). However, the captured Tx's focused image size drops with the increase in link span, which poses a huge limitation because of the decrease in obtainable received signal area on the IS of the camera. Hence, to reduce this limitation, a novel technique was proposed in this thesis, which is to reduce the spatial bandwidth of the camera in its out of focus regions (i.e., defocusing) to enable a larger footprint of the Tx on the IS and facilitate longer transmission spans. Consequently, the proposed scheme was investigated via numeric simulations and also experimentally validated, where up to a 400 m link span was achieved experimentally with 100 % transmission success rate at a data rate of 800 bps with 25 fps (and with a 60 fps camera this will be 1920 bps). This technique relaxes the use of large surface area Txs to create large footprints where a small size Tx of 2.5 x 2.5 cm^2 surface area was used in this research work, which was 19 times smaller than the Tx adopted in the previous work earlier highlighted as the longest link distance reported (prior to the work in this thesis) of 328

m at 15 bps. Also, the developed image processing and detection scheme employed for this work was also presented.

In Chapter 5 the effects of turbulence and fog on a vehicular VLC link (employing an incoherent and non-collimated light source i.e., LEDs) were investigated, which have been sparely reported in literature. This is contrast to OWC links employing a coherent and collimated light source i.e., lasers and PD-based Rxs where the effects of turbulence and fog have been well reported. Different turbulence mitigation techniques have been proposed for free space optics (i.e., laser based outdoor OWC applications), which cannot be directly applied to vehicular VLC as discussed in Chapter 5, however the aperture averaging method, which is the simplest and can easily be implemented for vehicular VLC was experimentally investigated. The performance of a PD and camera based vehicular VLC link in terms of the average SNR and PSNR, respectively, under turbulence with aperture averaging were evaluated. Results obtained showed the potency of aperture averaging in combating the turbulence effects, as there was no significant system performance degradation under turbulence (compared with the clear channel), with only a penalty of 0.1 and 0.7 dB in the SNR and PSNR, for the PD and camera Rx based links, respectively, at the highest turbulence strength considered of refractive index structure parameter C_n^2 of ~1.0 $\times 10^{-10}$ $m^{-2/3}$. Moreover, the effect of different visibility levels under fog on an OCC based vehicular link was investigated. Results obtained showed that the link was error free up to a meteorological visibility or 20 m for a MI of 0.5 and up to 10 m meteorological visibility for MIs of 0.75 and 1. However, for all the MIs the link performance degraded considerably below 10 m meteorological visibility.

Chapter 6 presented investigations carried out on relay-assisted vehicular VLC for up to 4 hops (i.e., up to 5 consecutive transmission channels) with AF and DF

relaying schemes under realistic emulated sunlight noise obtained from empirical measurements. Results obtained under emulated sunlight noise showed that the DF scheme was a potential option for vehicular VLC connectivity providing up to 150 % increase in the achieved link distance than AF at FEC BER limit of 3.8×10^{-3} by the end of the 2nd hop. Also, the effect of the relay vehicle's orientation in relation to the source vehicle was examined. For the first time, the effect of BSO at the PD on the performance of the vehicular VLC link was investigated (which is similar to pointing errors in free space optics) when there is a misalignment between the Tx and Rx. A method to mitigate the BSO effect was also proposed. Furthermore, insights into the impact of various system parameters on relay-assisted vehicular VLC were provided. Finally, experimental demonstration of a relay-assisted link within a laboratory environment was carried out, where the BER values for the DF link were all below the FEC BER limit of 3.8×10^{-3} illustrating that the DF scheme was a suitable candidate for vehicular VLC connectivity.

This thesis focused on the key challenges of vehicular VLC connectivity that will facilitate multi-hop networks and provided original contributions and insights such as (*i*) increasing the robustness to noise under sunlight noise and mitigating the effects of atmospheric turbulence; (*ii*) increasing the communication range for both PD and camera-based links and relay-assisted multi-hop links; and (*iii*) enhancing the mobility.

7.2 Future works

The research work in this thesis uncovers more opportunities and areas that needs investigations. The following are recommended for future works:

1. For OCC based vehicular links, there is the need to track the light source in the captured image due to mobility of vehicles. Furthermore, an automatic recognition process of TLs, HLs in an image where there are multiple light sources including streetlights, advertising boards, etc is essential and should be investigated. This is needed in order to determine the required ROI and extract the required information under the dynamic environment and applications of artificial intelligence for this purpose can also be examined.
2. The effects of fog on PD based vehicular VLC links under different visibility levels should be investigated, as only the effects of fog on OCC vehicular links were carried out in this thesis.
3. Higher order modulation formats for OCC based vehicular links should be investigated to further enhance the data rate. For PD based vehicular VLC links, other modulation formats aside OOK should also be investigated.
4. The utilisation of artificial intelligence for equalisation in vehicular VLC links to enhance the system performance under various deployment scenarios, such as under degrading weather conditions should also be explored.
5. Development of a comprehensive analytical model for vehicular networks.

REFERENCES

[1] M.W. Akhtar, S.A. Hassan, R. Ghaffar, H. Jung, S. Garg, and M. S. Hossain, "The shift to 6G communications: vision and requirements," *Hum. Cent. Comput. Inf. Sci.* vol. 10, no. 1, 2020.

[2] M. H. Alsharif, A. H. Kelechi, M. A. Albreem, S. A. Chaudhry, M. S. Zia, and S. Kim, "Sixth generation (6G) wireless networks: vision, research activities, challenges and potential solutions, " *Symmetry*, vol. 12, no. 4, p. 676, Apr. 2020.

[3] Statista Research Development, *Internet of things-number of connected devices worldwide 2015-2025*, Nov. 2016. [Online]. Available: https://www.statista.com/statistics/471264/iot-number-of-connected-devices-worldwide/

[4] Y. Zhou *et al*, "Service-aware 6G: An intelligent and open network based on the convergence of communication, computing and caching, " *Digital Communications and Networks*, vol. 6, no. 3, pp. 253-260, 2020.

[5] Y. Zhou, L. Tian, L. Liu, and Y. Qi, "Fog computing enabled future mobile communication networks: a convergence of communication and computing," *IEEE Communications Magazine*, vol. 57, no. 5, pp. 20-27, May 2019.

[6] M. Katz, and I. Ahmed, "Opportunities and challenges for visible light communications in 6G," *2020 2nd 6G Wireless Summit (6G SUMMIT)*, Levi, Finland, 2020, pp. 1-5.

[7] M. Z. Chowdhury, M. Shahjalal, M. K. Hasan, and Y. M. Jang, "The role of optical wireless communication technologies in 5G/6G and IoT solutions: prospects, directions, and challenges," *Applied Sciences*, vol. 9, no. 20, p. 4367, Oct. 2019.

[8] O. K. Tonguz, *How Vehicle-to-Vehicle Communication Could Replace Traffic Lights and Shorten Commutes*, 2018. [Online]. Available: https://spectrum.ieee.org/how-vehicletovehicle-communication-could-replace-traffic-lights-and-shorten-commutes.

[9] T. Liu, A. A. Abouzeid, and A. A. Julius, "Traffic flow control in vehicular communication networks," *American Control Conference (ACC)*, 2017, pp. 5513-5518.

[10] E. Eso *et al*., "Experimental demonstration of vehicle to roadside infrastructure visible light communications," *2019 2nd West Asian Colloquium on Optical Wireless Communications (WACOWC)*, Tehran, Iran, 2019, pp. 85-89.

[11] S. Khandelwal, A. Abhale, and U. Nagaraj, "Accident prevention and air pollution control using vanet under cloud environment," *Proceedings of 3rd International Conference on Recent Trends in Engineering & Technology (ICRTET'2014)*, 2014, pp. 900-904.

[12] S. Gao, A. Lim, and D. Bevly, "An empirical study of DSRC V2V performance in truck platooning scenarios," *Digital Communications and Networks*, vol. 2, no.4, pp. 233-244, 2016.

[13] H. B. Eldeeb *et al*., "Vehicular VLC: A ray tracing study based on measured radiation patterns of commercial taillights," *IEEE Photonics Technology Letters*, vol. 33, no. 16, pp. 904-907, Aug. 2021.

[14] A. Memedi, C. Tebruegge, J. Jahneke, and F. Dressler, "Impact of Vehicle Type and Headlight Characteristics on Vehicular VLC Performance," *2018 IEEE Vehicular Networking Conference (VNC)*, 2018, pp. 1-8.

[15] A. Memedi, H. Tsai, and F. Dressler, "Impact of Realistic Light Radiation Pattern on Vehicular Visible Light Communication," *IEEE Global Communications Conference*, 2017, pp. 1-6.

[16] M. Uysal, Z. Ghassemlooy, A. Bekkali, A. Kadri, and H. Menouar, "Visible light communication for vehicular networking: Performance study of a V2V system using a measured headlamp beam pattern model," *IEEE Vehicular Technology Magazine*, vol. 10, no. 4, pp. 45-53, Dec. 2015.

[17] W. Shen, and H. Tsai, "Testing vehicle-to-vehicle visible light communications in real-world driving scenarios," *IEEE Vehicular Networking Conference (VNC)*, 2017, pp. 187-194.

[18] X. Ma, X. Chen, and H.H Refai, "Performance and reliability of DSRC vehicular safety communication: A formal analysis, " *J Wireless Com Network*, 2009.

[19] E. Torres-Zapata, V. Guerra, J. Rabadan, R. Perez-Jimenez, and J. M. Luna-Rivera, "Vehicular communications in tunnels using VLC," *2019 15th International Conference on Telecommunications (ConTEL)*, 2019, pp. 1-6.

[20] H. Viittala, S. Soderi, J. Saloranta, M. Hamalainen, and J. Iinatti, "An experimental evaluation of wifi-based vehicle-to-vehicle (V2V) communication in a tunnel," *2013 IEEE 77th Vehicular Technology Conference (VTC Spring)*, 2013, pp. 1-5.

[21] M. Bozanic, and S. Sinha, "*Mobile Communication Networks: 5G and a Vision of 6G*, " Springer International Publishing, 2021.

[22] Y. Du, Y. Xu, L. Xue, L. Wang, and F. Zhang, "an energy-efficient cross-layer routing protocol for cognitive radio networks using apprenticeship deep reinforcement learning," *Energies*, vol. 12, no. 14, p. 2829, Jul. 2019.

[23] R. K. Saha, "Realization of licensed/unlicensed spectrum sharing using eICIC in indoor small cells for high spectral and energy efficiencies of 5G networks," *Energies*, vol. 12, no. 14, p. 2828, Jul. 2019.

[24] L. You, W. Wang, and X. Gao, "energy-efficient multicast precoding for massive MIMO transmission with statistical CSI," *Energies*, vol. 11, no. 11, p. 3175, Nov. 2018.

[25] I.-H. Lee, and H. Jung, "Energy-efficient path selection using SNR correlation for wireless multi-hop cooperative communications," *Energies*, vol. 11, no. 11, p. 3004, Nov. 2018.

[26] G. Kim, J.-G. Kang, and M. Rim, "Dynamic duty-cycle MAC protocol for IoT environments and wireless sensor networks," *Energies*, vol. 12, no. 21, p. 4069, Oct. 2019.

[27] R. K. Saha, "Countrywide mobile spectrum sharing with small indoor cells for massive spectral and energy efficiencies in 5G and beyond mobile networks," *Energies*, vol. 12, no. 20, p. 3825, Oct. 2019.

[28] E. Eso, Z. Ghassemlooy, S. Zvanovec, J. Sathian, M. Mansour Abadi, and O.I. Younus. Performance of vehicular visible light communications under the effects of atmospheric turbulence with aperture averaging. *Sensors*, vol. 21, no. 8, p.2751, 2021.

[29] Z. Ghassemlooy, S. Arnon, M. Uysal, Z. Xu, and J. Cheng, "Emerging optical wireless communications-advances and challenges," *IEEE JSAC*, vol. 33, no. 9, pp. 1738–1749, 2015.

[30] M. Z. Chowdhury, M. T. Hossan, A. Islam, and Y. M. Jang, "A comparative survey of optical wireless technologies: Architectures and applications," *IEEE Access*, vol. 6, pp. 9819–9840, 2018.

[31] S.-H. Yu, O. Shih, H.-M. Tsai, N. Wisitpongphan, and R. Roberts, “Smart automotive lighting for vehicle safety,” *IEEE Communications Magazine*, vol. 51, no. 12, pp. 50–59, Dec. 2013.

[32] B. Aly, M. Elamassie, B. Kebapci, and M. Uysal, "Experimental evaluation of a software defined visible light communication system," *2020 IEEE International Conference on Communications Workshops (ICC Workshops)*, 2020, pp. 1-6.

[33] A. Cailean, B. Cagneau, L. Chassagne, V. Popa, and M. Dimian, "A survey on the usage of DSRC and VLC in communication-based vehicle safety applications," *2014 IEEE 21st Symposium on Communications and Vehicular Technology* in the Benelux (SCVT), 2014, pp. 69-74.

[34] H. B. Eldeeb, E. Yanmaz, and M. Uysal, "MAC layer performance of multi-hop vehicular VLC networks with CSMA/CA," 2020 *12th International Symposium on Communication Systems, Networks and Digital Signal Processing (CSNDSP)*, 2020, pp. 1-6.

[35] H. B. Eldeeb, E. Eso, M. Uysal, Z. Ghassemlooy, S. Zvanovec, and J. Sathian, "Vehicular visible light communications: The impact of taillight radiation pattern," 2020 *IEEE Photonics Conference (IPC)*, 2020, pp. 1-2.

[36] J. H. Yoo, J. S. Jang, J. K. Kwon, H. C. Kim, D. W. Song, and S.Y. Jung, "Demonstration of vehicular visible light communication based on LED headlamp, " *International Journal of Automotive Technology*, vol. 17, no. 2, pp. 347–352, 2016.

[37] Car Lighting District, *Halogen vs HID vs LED- Which is Best?*, 2018. [Online]. Available: https://www.carlightingdistrict.com/blogs/news/halogen-vs-hid-vs-led-which-is-best.

[38] R. D. Dupuis, and M. R. Krames, "History, development, and applications of high-brightness visible light-emitting diodes," *Journal of Lightwave Technology*, vol. 26, no. 9, pp. 1154-1171, 2008.

[39] P. H. Pathak, X. Feng, P. Hu, and P. Mohapatra, “Visible light communication, networking, and sensing: A survey, potential and challenges”, *IEEE Communications Surveys Tutorials*, vol. 17, no. 4, pp. 2047-2077, 2015.

[40] L. E. M. Matheus, A. B. Vieira, L. F. Vieira, M. A. Vieira, and O. Gnawali, “Visible light communication: Concepts, applications and challenges,” *IEEE Communications Surveys & Tutorials*, vol. 21, no. 4, pp. 3204-3237, Fourthquarter 2019.

[41] I. Amirul, Md Tanvir Hossan, and Y. M. Jang. "Convolutional neural network scheme–based optical camera communication system for intelligent internet of vehicles." *International Journal of Distributed Sensor Networks*, vol. 14, no.4, 2018.

[42] S.R. Teli, S. Zvanovec, and Z. Ghassemlooy. "Performance evaluation of neural network assisted motion detection schemes implemented within indoor optical camera-based communications, " *Optics Express*, vol. 27, no. 17, pp. 24082-24092, 2019.

[43] W.A. Cahyadi, Y.H. Chung, Z. Ghassemlooy, and N.B. Hassan, "Optical camera communications: Principles, modulations, potential and challenges, " *Electronics*, vol. 9, no.9, p.1339, 2020.

[44] T. Yamazato *et al*, "Image-sensor-based visible light communication for automotive applications," *IEEE Communications Magazine*, vol. 52, no. 7, pp. 88-97, July 2014.

[45] L. Liu, R. Deng, and L. Chen, "47-kbit/s RGB-LED-based optical camera communication based on 2D-CNN and XOR-based data loss compensation," *Optics Express* vol. 27, no.23, pp. 33840-33846, 2019.

[46] D. Karunatilaka, F. Zafar, V. Kalavally, and R. Parthiban, “LED based indoor visible light communications: state of the art”, *IEEE Communications, Surveys and Tutorials*, vol. 17, no. 3, pp. 1649-1678, 2015.

[47] F. Miramirkhani, and M. Uysal, “Channel modeling and characterization for visible light communications,” *IEEE Photonics Journal*, vol. 7, no. 6, pp. 1–16, Dec. 2015.

[48] M. Karbalayghareh, F. Miramirkhani, H. B. Eldeeb, R. C. Kizilirmak, S. M. Sait, and M. Uysal, "Channel modelling and performance limits of vehicular visible light communication systems," *IEEE Transactions on Vehicular Technology*, vol. 69, no. 7, pp. 6891-6901, July 2020.

[49] A. M. Cailean, and M. Dimian, “Impact of IEEE 802.15.7 standard on visible light communications usage in automotive applications," *IEEE Communications Magazine*, vol. 55, no. 4, pp. 169-175, April 2017.

[50] A. M. Cailean, and M. Dimian, “Current challenges for visible light communications usage in vehicle applications: A survey”, *IEEE Communications Surveys and Tutorials*, vol. 19, no. 4, pp. 2681-2703, 2017.

[51] E. Eso, A. Burton, N. B. Hassan, M. M. Abadi, Z. Ghassemlooy, and S. Zvanovec, "Experimental investigation of the effects of fog on optical camera-based VLC for a vehicular environment," *2019 15th International Conference on Telecommunications (ConTEL), Graz, Austria*, 2019, pp. 1-5.

[52] L. Cheng, W. Viriyasitavat, M. Boban, and H. Tsai, "Comparison of radio frequency and visible light propagation channels for vehicular communications," *IEEE Access*, vol. 6, pp. 2634-2644, 2018.

[53] M. Elamassie, M. Karbalayghareh, F. Miramirkhani, R. C. Kizilirmak, and M. Uysal, "Effect of fog and rain on the performance of vehicular visible light communications*," 2018 IEEE 87th Vehicular Technology Conference (VTC Spring), Porto, 2018, pp. 1-6.*

[54] Z. Ghassemlooy, W. Popoola, and S. Rajbhandari, *Optical Wireless Communications: System and Channel Modelling with Matlab®*, CRC press, 2019.

[55] E. T. Eso, "Turbulence effects on free space optical communication systems: A review, "*International Journal of Information Technology and Electrical Engineering*. vol. 4, no. 5, pp 22-27, 2015.

[56] I. Lee, Z. Ghassemlooy, W. Ng, M. Khalighi, and S. Liaw, "Effects of aperture averaging and beam width on a partially coherent gaussian beam over free-space optical links with turbulence and pointing errors," *Appl. Opt.* vol. 55, no. 1, pp. 1-9, 2016.

[57] M. Safari, and M. Uysal, “Relay-assisted free-space optical communication,” *IEEE Transactions on Wireless Communications*, vol. 7, no. 12, pp. 5441–5449, Dec. 2008.

[58] O. Narmanlioglu, B. Turan, S. C. Ergen, and M. Uysal, "Cooperative MIMO-OFDM based inter-vehicular visible light communication using brake lights, " *Computer Communications,* vol. 120, pp.138-146, 2018.

[59] H. Chowdhury, and M. Katz, "Cooperative multihop connectivity performance in visible light communications," *Proceedings of the IFIP Wireless Day (WD),* Nov. 2013, pp. 1–4.

[60] R. C. Kizilirmak, O. Narmanlioglu, and M. Uysal, "Relay-assisted OFDM-based visible light communications," *IEEE Transactions on Wireless Communications*, vol. 63, no. 10, pp. 3765–3778, Oct. 2015.

[61] Road Safety Authority (Government of Ireland), *The two-second rule*, 2007. [Online]. Available: *//web.archive.org/web/20120309213451/http://www.rotr.ie/rules-for-driving/speed-limits/speed-limits_2-second-rule.html*

[62] World Health Organization, *Global Status Report on Road Safety 2018*, 2018. [Online]. Available: https://www.who.int/violence_injury_prevention/road_safety_status/2018/GSRRS2018_Summary_EN.pdf

[63] Infocomm Media Development Authority (IMDA), *Dedicated Short Range Communications in Intelligent Transport Systems (Technical Specification),* 2017. Accessed on: Apr. 26, 2021. [Online]. Available: https://www.imda.gov.sg/-/media/imda/files/regulation-licensing-and-consultations/ict-standards/telecommunication-standards/radio-comms/imda-ts-dsrc.pdf?la=en

[64] IEEE Standard for Information technology-- Local and metropolitan area networks-- Specific requirements-- Part 11: Wireless LAN Medium Access Control (MAC) and Physical Layer (PHY) Specifications Amendment 6: Wireless Access in Vehicular Environments," *IEEE Std 802.11p-2010 (Amendment to IEEE Std 802.11-2007 as amended by IEEE Std 802.11k-2008, IEEE Std 802.11r-2008, IEEE Std 802.11y-2008, IEEE Std 802.11n-2009, and IEEE Std 802.11w-2009),* pp.1-51, July 2010

[65] R. Atallah, M. Khabbaz, and C. Assi, "Multihop V2I communications: A feasibility study, modeling, and performance analysis," *IEEE Transactions on Vehicular Technology* vol. 66, no. 3, pp. 2801–2810, 2017.

[66] K. Bilstrup, E. Uhlemann, E. Ström, and U. Bilstrup, “On the ability of the 802.11p MAC method and STDMA to support real-time vehicle-to-vehicle communication,” *EURASIP Journal on Wireless Communications and Networking*, vol. 1, pp. 1-13, 2009.

[67] Y. Yao, L. Rao, and X. Liu, “Performance and reliability analysis of IEEE 802.11p safety communication in a highway environment,” *IEEE Transactions on Vehicular Technology* vol. 62, no. 9, pp. 4198–4212, Nov. 2013.

[68] S. Eichler, “Performance evaluation of the IEEE 802.11p WAVE communication standard,” *IEEE Vehicular Technology Conference*, 2007, pp. 2199–2203.

[69] A.-M. Cailean, B. Cagneau, L. Chassagne, V. Popa, and M. Dimian, “A survey on the usage of DSRC and VLC in communication-based vehicle safety applications,” *IEEE 21st Symposium on Commununications and Vehicular Technology, Benelux (SCVT)*, Nov. 2014, pp. 69–74.

[70] K. Karlsson, C. Bergenhem, and E. Hedin, “Field measurements of IEEE 802.11p communication in NLOS environments for a platooning application,” *IEEE Vehicular Technology Conference (VTC Fall)*, Sep. 2012, pp. 1–5.

[71] A.-M. Cailean, B. Cagneau, L. Chassagne, M. Dimian, and V. Popa, “Novel receiver sensor for visible light communications in automotive applications,” *IEEE Sensors Journal*, vol. 15, no. 8, pp. 4632–4639, Aug. 2015.

[72] M. Atta, and A. Bermak, "A 160 m visible light communication link using hybrid undersampled phase-frequency shift on-off keying and CMOS image sensor," *Optics Express*, vol. 27, no. 3, pp. 2478-2487, 2019.

[73] A. Memedi, and F. Dressler, "vehicular visible light communications: a survey," *IEEE Communications Surveys & Tutorials*, vol. 23, no. 1, pp. 161-181, Firstquarter 2021.

[74] Fraunhofer HHI, *LiFi-Technology enables driverless platooning of trucks for the first time on Japanese highway*, 2021. [Online]. Available: https://www.hhi.fraunhofer.de/en/news/nachrichten/2021/lifi-technology-

enables-driverless-platooning-of-trucks-for-the-first-time-on-japanese-highway.html

[75] M. S. Islim et al., "The impact of solar irradiance on visible light communications," *Journal of Lightwave Technology*, vol. 36, no. 12, pp. 2376-2386, June 2018.

[76] H. Farahneh, S. M. Kamruzzaman, and X. Fernando, "Differential receiver as a denoising scheme to improve the performance of V2V-VLC systems," *2018 IEEE International Conference on Communications Workshops (ICC Workshops)*, 2018, pp. 1-6.

[77] H. Farahneh, F. Hussain, and X. Fernando, "Performance analysis of adaptive OFDM modulation scheme in VLC vehicular communication network in realistic noise environment," *Journal on Wireless Communications Network*, vol. 2018, pp. 1-15, 2018.

[78] N. A. M. Nor 'Study of all-optical FSO relay-based systems under the influence of the atmospheric turbulence channel'. PhD thesis, Faculty of Engineering and Environment, Northumbria University, 2018.

[79] D. Schulz *et al*., "Long-term outdoor measurements using a rate-adaptive hybrid optical wireless/60 GHz link over 100 m", *IEEE 19th International Conference on Transparent Optical Networks (ICTON)*, 2017, pp. 1-4.

[80] Y. H. Kim, W. A. Cahyadi, and Y. H. Chung, "Experimental demonstration of VLC-based vehicle-to-vehicle communications under fog conditions", *IEEE Photonics Journal*, vol. 7, no. 6, pp. 1-9, 2015.

[81] H. Weichel, '*Laser beam propagation in the atmosphere*' SPIE, Bellingham, 1990.

[82] H. Henniger, and O. Wilfert, 'An introduction to free-space optical communications', *Radio Engineering*, vol. 19, no. 2, pp. 203–212, 2010.

[83] I. I. Kim, B. McArthur, and E. Korevaar, 'Comparison of laser beam propagation at 785 nm and 1550 nm in fog and haze for optical wireless communications', *SPIE Proceedings on Optical Wireless Communications III*, 2001, vol. 4214, pp. 26–37.

[84] J. M. Kahn and J. R. Barry, "Wireless infrared communications," *Proceedings of the IEEE*, vol. 85, 1997, pp. 265-298.

[85] M. M. Abadi, "A hybrid free space optics/radio frequency antenna – design and evaluation, " PhD thesis, Faculty of Engineering and Environment Northumbria University, 2017.

[86] N. A. M. Nor, E. Fabiyi, M. M. Abadi, X. Tang, Z. Ghassemlooy, and A. Burton, "Investigation of moderate-to-strong turbulence effects on free space optics — A laboratory demonstration," *2015 13th International Conference on Telecommunications (ConTEL)*, 2015, pp. 1-5.

[87] L. C. Andrews and R. L. Phillips, *Laser beam propagation through random media*, 2nd Ed. Washington, USA: SPIE Press, 2005.

[88] Z. Ghassemlooy, H. Le Minh, S. Rajbhandari, J. Perez and M. Ijaz, "Performance analysis of ethernet/fast-ethernet free space optical communications in a controlled weak turbulence condition," *Journal of Lightwave Technology*, vol. 30, no. 13, pp. 2188-2194, July 2012.

[89] L. Guo, M. Cheng, and L.Guo, "Visible light propagation characteristics under turbulent atmosphere and its impact on communication performance of traffic system," *Proceedings of the SPIE 11170, 14th National Conference on Laser Technology and Optoelectronics (LTO)*, 2019.

[90] R. Martinek, L. Danys, and R. Jaros, "Visible light communication system based on software defined radio: Performance study of intelligent transportation and indoor applications, " *Electronics*, vol. 8, no. 4, p. 433, Apr. 2019.

[91] L. Andrews, R. Phillips, and C. Hopen, "*Theory of optical scintillation with applications*, " 1st ed. Bellingham, Wash.: SPIE Optical Engineering Press, 2001.

[92] M. Al-Habash, R. Phillips, and L. Andrews, "Mathematical model for the irradiance probability density function of a laser beam propagating through turbulent media, " *Optical Engineering*, vol 40, no. 8, pp. 1554-1562, 2001.

[93] H.G. Sandalidis, N.D. Chatzidiamantis, and G.K. Karagiannidis, "A tractable model for turbulence- and misalignment-induced fading in optical wireless systems," *IEEE Communications Letters*, vol. 20, no. 9, pp. 1904-1907, Sept. 2016.

[94] A. Jurado-Navas, J. M. Garrido-Balsells, J. F. Paris, M. Castillo-Vázquez, and A. Puerta-Notario, "Further insights on Málaga distribution for atmospheric optical communications," *2012 International Workshop on Optical Wireless Communications (IWOW)*, 2012, pp. 1-3.

[95] P. Luo, Z. Ghassemlooy, H. Le Minh, E. Bentley, A. Burton, and X. Tang, "Performance analysis of a car-to-car visible light communication system," *Applied Optics*, vol. 54, no. 7, pp. 1696–1706, 2015.

[96] H. Y. Tseng, Y. L. Wei, A. L. Chen, H. P. Wu, H. Hsu, and H. M. Tsai, "Characterizing link asymmetry in vehicle-to-vehicle Visible Light Communications," *2015 IEEE Vehicular Networking Conference (VNC)*, 2015, pp. 88-95.

[97] A. R. Ndjiongue, T. M. N. Ngatched, and H. C. Ferreira, "AF cooperative VLC communication systems: cascaded channel analysis." *IEEE International Conference on Communications (ICC)*, 2019, pp. 1-6.

[98] M. Safari, and M. Uysal, "Relay-assisted free-space optical communication," *IEEE Transactions on Wireless Communications*, vol. 7, no. 12, pp. 5441–5449, Dec. 2008.

[99] Z. Wu, "Free space optical networking with visible light: A multi-hop multi-access solution," PhD thesis, College of Engineering, Boston University, 2012.

[100] C. B. Liu, B. Sadeghi, and E. W. Knightly, "Enabling vehicular visible light communication (V2LC) networks, " *Proceedings of the 8th ACM International Workshop on Vehicular Inter-Networking*, 2011, pp. 41–50.

[101] H.-J. Kim, S. V. Tiwari, and Y.-H. Chung, "Multi-hop relay-based maritime visible light communication, " *Chinese Optics Letters*, vol. 14, no. 5, pp. 1–5, May 2016.

[102] R. C. Kizilirmak, O. Narmanlioglu, and M. Uysal, "Relay-assisted OFDM-based visible light communications," *IEEE Transactions on Communications*, vol. 63, no. 10, pp. 3765–3778, Oct. 2015.

[103] H. Chowdhury, and M. Katz, "Cooperative multihop connectivity performance in visible light communications, " *Proceedings of the IFIP Wireless Day (WD)*, Nov. 2013, pp. 1–4.

[104] T. Saito, S. Haruyama, and M. Nakagawa, "A new tracking method using image sensor and photo diode for visible light road-to vehicle communication," *10th International Conference on Advance Communication Technologies (ICACT)*, Feb. 2008, pp. 673–678.

[105] S. Okada *et al.*, "On-vehicle receiver for distant visible light road-to-vehicle communication, " *IEEE Intelligent Vehicle Symposium (IV)*, Jun. 2009, pp. 1033–1038.

[106] J. Jeong *et al.*, "Receiver angle control in an infrastructure-to-car visible light communication link, " *IEEE Region 10 Conference (TENCON)*, 2016, pp. 1957–1960.

[107] M. M. Rahman, L. Bobadilla, and B. Rapp, "Establishing line-of-sight communication via autonomous relay vehicles, " *IEEE Military Communications Conference* (*MILCOM*), 2016, pp. 642–647.

[108] H. B. Eldeeb, and M. Uysal, "Vehicle-to-vehicle visible light communication: How to select receiver locations for optimal performance?," *11th International Conference on Electrical and Electronics Engineering (ELECO)*, 2019, pp. 402-405.

[109] Z. Chen, N. Serafimovski, and H. Haas, "Angle diversity for an indoor cellular visible light communication system," *IEEE 79th Vehicular Technology Conference (VTC Spring)*, pp. 1–5, May 2014.

[110] H. B. Eldeeb, M. Hosney, H. M. Elsayed, R. I. Badr, M. Uysal, and H. A. I. Selmy, "Optimal resource allocation and interference management for multi-user uplink light communication systems with angular diversity technology," *IEEE Access*, vol. 8, pp. 203224-203236, 2020.

[111] H. B. Eldeeb, H. A. I. Selmy, H. M. Elsayed, and R. I. Badr, ''Co-channel interference cancellation using constraint field of view ADR in VLC channel,'' *IEEE Photonics Conference (IPC)* Part II, Oct. 2017, pp. 1–2.

[112] C. Chen, W.-D. Zhong, H. Yang, S. Zhang, and P. Du, ''Reduction of SINR fluctuation in indoor multi-cell VLC systems using optimized angle diversity receiver,'' *Journal of Lightwave Technology*, vol. 36, no. 17, pp. 3603–3610, Sep. 2018.

[113] Transcend, *8 steps to the best dash cam*, 2021. [Online]. Available: https://www.transcend-info.com/Article/Dashcam#:~:text=The%20most%20common%20field%20of,view%20isn't%20necessarily%20better.

[114] D. C. O'Brien, *et al*., "Gigabit optical wireless for a Home Access Network," *IEEE 20th International Symposium on Personal, Indoor and Mobile Radio Communications*, 2009, pp. 1-5.

[115] Nationwide Vehicle Contracts, *Understanding Car Size and Dimensions*, 2020. [Online]. Available: www.nationwidevehiclecontracts.co.uk/blog/understanding-car-size-and-dimensions

[116] V.A. Jacobs *et al*, "Analysis of errors associated with photometric distance in goniophotometry," *Proceedings of the 28th Session of the CIE*, 2015, pp. 1-11.

[117] R. Hui, and M. O'Sullivan, '*Fiber Optic Measurement Techniques*' Academic Press, pp. 1-128, 2009.

[118] "*Speed limits*", United Kingdom government. Available: https://www.gov.uk/speed-limits.

[119] T. Komine, and M. Nakagawa, "Fundamental analysis for visible-light communication system using LED lights," *IEEE Transactions on Consumer Electronics*, vol. 50, no. 1, pp. 100-107, Feb. 2004.

[120] R. Hui '*Introduction to Fiber-Optic Communication*' Academic Press, pp. 125-154, 2020

[121] O. Haddad, M. A. Khalighi, and S. Zvanovec. Channel characterization for optical extra-WBAN links considering local and global user mobility, *SPIE OPTO*, Feb 2020.

[122] R. Paudel 'Modelling and analysis of free space optical link for ground-to-train communications' PhD thesis, Faculty of Engineering and Environment Northumbria University, 2014.

[123] J. Dang, L. Wu, and Z. Zhang, "OFDM systems for optical communication with intensity modulation and direct detection," in *Optical fiber and*

wireless communications, Ed., R Roka, Rijeka, Croatia: IntechOpen vol. 5, pp. 85–103, 2017.

[124] International Electrotechnical Commission. IEC-62471: Photobiological safety of lamps and lamp systems. s.l.: IEC, 2006. Table 6.1. CIE/IEC-62471:2006.

[125] Lasp Interactive Solar Irradiance Datacentre (LISIRD), *CSIM Solar Spectral Irradiance, Time series*, [Online]. Available: https://lasp.colorado.edu/lisird/data/csim_ssi_l3/

[126] S. M. Mana, P. Hellwig, J. Hilt, P. W. Berenguer, and V. Jungnickel, "Experiments in non-line-of-sight li-fi channels," *2019 Global LIFI Congress (GLC)*, 2019, pp. 1-6.

[127] M. J. Jang, IEEE 802.15 WPAN 15.7 Amendment Study Group, 2019.

[128] Z. Ghassemlooy, L. N. Alves, S. Zvanovec, and M.-A. Khalighi, *Visible light communications: Theory and Applications*, CRC Press, 2017.

[129] W. A. Cahyadi, Y. H. Chung, Z. Ghassemlooy, and N. B. Hassan, "Optical camera communications: principles, modulations, potential and challenges," *Electronics*, vol. 9, no. 9, p. 1339, Aug. 2020.

[130] C. Jurado-Verdu, V. Matus, J. Rabadan, V. Guerra, and R. Perez-Jimenez, "Correlation-based receiver for optical camera communications," *Optics Express*, vol. 27, no. 14, pp.19150-19155, 2019.

[131] T. Fujihashi, T. Koike-Akino, P. V. Orlik, and T. Watanabe, "Experimental throughput analysis in screen-camera visual MIMO communications," *IEEE Global Communications Conference (GLOBECOM)*, 2016, pp. 1-6.

[132] N. Manh Tuan, T. Viet Phuong, T. H. Do, and N. Tan Vu Khanh, "An highly realistic optical camera communication simulation framework for Internet of Things applications," *21st ACIS International Winter Conference on Software Engineering, Artificial Intelligence, Networking and Parallel/Distributed Computing (SNPD-Winter)*, 2021, pp. 240-242.

[133] N. Van Hoa, H. Nguyen, C. H. Nguyen, and Y. Min Jang, "OCC technology based developing IoT network," *International Conference on Information and Communication Technology Convergence (ICTC)*, 2020, pp. 670-673.

[134] A. Krohn, P. A. Hoeher, and S. Pachnicke, "Visible light tricolor LED-to-camera data transmission suitable for internet-of-things and sensor

applications," *2018 European Conference on Optical Communication (ECOC)*, 2018, pp. 1-3.

[135] T. Tripp, A. S. Hamza, B. Underwood, and R. Tashakkori, "Low-cost UFSOOK based optical camera communication link for IoT applications," *2020 IEEE 6th World Forum on Internet of Things (WF-IoT)*, 2020, pp. 1-6.

[136] T. Nguyen, A. Islam, T. Hossan, and Y. M. Jang, "Current status and performance analysis of optical camera communication technologies for 5G networks," *IEEE Access*, vol. 5, pp. 4574-4594, 2017.

[137] A. Duquel, R. Stanica, H. Rivano, and A. Desportes, "Decoding methods in LED-to smartphone bidirectional communication for the IoT," *Global LIFI Congress (GLC)*, 2018, pp. 1-6.

[138] S. R. Teli, S. Zvanovec, and Z. Ghassemlooy, "Optical internet of things within 5G: Applications and challenges," *IEEE International Conference on Internet of Things and Intelligence System (IOTAIS)*, 2018, pp. 40-45.

[139] C. H. Nguyen, V. H. Nguyen, and Y. M. Jang, "Optical camera communication (OCC) applications for internet of vehicle (IoV)," *International Conference on Information and Communication Technology Convergence (ICTC)*, 2019, pp. 512-514.

[140] I. Takai, T. Harada, M. Andoh, K. Yasutomi, K. Kagawa, and S. Kawahito, "Optical vehicle-to-vehicle communication system using LED transmitter and camera receiver," *IEEE Photonics Journal*, vol. 6, no. 5, pp. 1-14, Oct. 2014.

[141] R. Boubezari, L. H. Minh, Z. Ghassemlooy, and A. Bouridane, "Smartphone camera based visible light communication", *Journal of Lightwave Technology*, vol. 34, no. 17, pp. 4121-4127, 2016.

[142] A. Islam, M. T. Hossan, and Y. M. Jang, "Introduction of optical camera communication for internet of vehicles (IoV)," *Ninth International Conference on Ubiquitous and Future Networks (ICUFN)*, 2017, pp. 122-125.

[143] M. D. Thieu, T. L. Pham, T. Nguyen, and Y. M. Jang, "Optical-RoI-signaling for vehicular communications," *IEEE Access*, vol. 7, pp. 69873-69891, 2019.

[144] S. Rane, A. Dubey, and T. Parida, "Design of IoT based intelligent parking system using image processing algorithms," *International Conference on Computing Methodologies and Communication (ICCMC)*, 2017, pp. 1049-1053.

[145] T. Nguyen, A. Islam, and Y. M. Jang, "Region-of-interest signaling vehicular system using optical camera communications," *IEEE Photonics Journal*, vol. 9, no. 1, pp. 1-20, Feb. 2017.

[146] T. L. Pham, M. Shahjalal, V. Bui, and Y. M. Jang, "Deep learning for optical vehicular communication," *IEEE Access*, vol. 8, pp. 102691-102708, 2020.

[147] M. K. Hasan, M. Shahjalal, M. Z. Chowdhury, N. Tuan Le, and Y. M. Jang, "Simultaneous traffic sign recognition and real-time communication using dual camera in ITS," *International Conference on Artificial Intelligence in Information and Communication (ICAIIC)*, 2019, pp. 517-520.

[148] M. Shahjalal, M. K. Hasan, M. Z. Chowdhury, and Y. M. Jang, "Smartphone camera based optical wireless communication system: requirements and implementation challenges," *Electronics*, vol. 8, no. 8, p. 913, Aug. 2019.

[149] M. T. Hossan, M. Z. Chowdhury, M. K. Hasan, M. Shahjalal, T. Nguyen, N. T. Le, and Y. M. Jang, "A new vehicle localization scheme based on combined optical camera communication and photogrammetry", *Mobile Information Systems*, vol. 2018, pp. 1-14, Apr. 2018.

[150] M. T. Hossan, M. Z. Chowdhury, A. Islam, and Y. M. Jang, "A novel indoor mobile localization system based on optical camera communication," *Wireless Communications and Mobile Computing*, vol. 2018, pp. 1-17, 2018.

[151] P. Chavez-Burbano, V. Guerra, J. Rabadan, C. Jurado-Verdu, and R. Perez Jimenez, "Novel indoor localization system using optical camera communication," *11th International Symposium on Communication Systems, Networks & Digital Signal Processing (CSNDSP)*, 2018, pp. 1-5.

[152] S. C. Mondal, S. Prabhu, V. K. Pandey, and A. Kumar, "Bidirectional communication system with screen based transmission and camera based reception of QR encoded information," *4th International Conference for Convergence in Technology (I2CT)*, 2018, pp. 1-5.

[153] V. Matus, V. Guerra, C. Jurado-Verdu, S. Zvanovec, and R. Perez-Jimenez, "Wireless sensor networks using sub-pixel optical camera communications: advances in experimental channel evaluation, " *Sensors*, vol. 21, no. 8, p. 2739, Apr. 2021.

[154] S.R. Teli, S. Zvanovec, and Z. Ghassemlooy, Performance evaluation of neural

network assisted motion detection schemes implemented within indoor optical camera-based communications. *Optics Express*, vol. 27, no. 17, pp. 24082–24092, 2019.

[155] S. R. Teli, S. Zvanovec, and Z. Ghassemlooy, "Experimental investigation of neuron based motion detection in internet of things using optical camera communications," *26th International Conference on Telecommunications (ICT)*, 2019, pp. 202-205.

[156] S. Teli, A. W. Anugrah, and H. Y. Chung, "Optical camera communication: motion over camera", *IEEE Communications Magazine*, vol. 55, no. 8, pp. 156-162, 2017.

[157] W. J. Ryu, and S. Y. Shin, "RGB MIMO optical camera communication with histogram equalization," *International Conference on Signals and Systems (ICSigSys)*, 2017, pp. 303-307,

[158] P. Luo et al., "Experimental demonstration of RGB LED-based optical camera communications," *IEEE Photonics Journal*, vol. 7, no. 5, pp. 1-12, Oct. 2015.

[159] H. Chen et al., "Color-shift keying for optical camera communication using a rolling shutter mode," *in IEEE Photonics Journal*, vol. 11, no. 2, pp. 1-8, April 2019.

[160] D. Han, and K. Lee, "High speed parallel transmission visible light communication method with multiple LED matrix image processing technique," *Eleventh International Conference on Ubiquitous and Future Networks (ICUFN)*, 2019, pp. 576-580.

[161] T. Fujihashi, T. Koike-Akino, P. V. Orlik, and T. Watanabe, "High-throughput visual MIMO systems for screen-camera communications," *IEEE Transactions on Mobile Computing*, vol. 20, no. 6, pp. 2200-2211, 2021.

[162] S. R. Teli, V. Matus, S. Zvanovec, R. Perez-Jimenez, S. Vitek, and Z. Ghassemlooy, “Optical camera communications for IoT–rolling-shutter based MIMO scheme with grouped LED array transmitter,” *Sensors*, vol. 20, no. 12, p. 3361, Jun. 2020.

[163] O. Isam Younus et al., "An artificial neural network equalizer for constant power4-PAM in optical camera communications," *12th International Symposium on Communication Systems, Networks and Digital Signal Processing (CSNDSP)*, 2020, pp. 1-6.

[164] O. I. Younus et al., "Data rate enhancement in optical camera communications using an artificial neural network equaliser," *IEEE Access*, vol. 8, pp. 42656-42665, 2020.

[165] O. I. Younus, N. B. Hassan, Z. Ghassemlooy, S. Zvanovec, L. N. Alves, and H. Le Minh, “The utilization of artificial neural network equalizer in optical camera communications,” *Sensors*, vol. 21, no. 8, p. 2826, Apr. 2021.

[166] H. Y. Lee, H. M. Lin, Y. L. Wei, H. I. Wu, H. M. Tsai, and K. C. J. Lin, "RollingLight: Enabling line-of-sight light-to-camera communications", *Proceedings of the 13th Annual International Conference on Mobile Systems, Applications, and Services*, May 2015, pp. 167-180.

[167] T. Nguyen, A. Islam, T. Hossan, and Y.M. Jang, "Current Status and Performance analysis of optical camera communication technologies for 5G networks", *IEEE Access*, vol. 5, pp. 4574-4594, 2017

[168] S. R. Teli, S. Zvanovec, R. Perez-Jimenez, and Z. Ghassemlooy, "Spatial frequency based angular behavior of a short-range flicker-free MIMO–OCC link," *Applied Optics*, vol. 59, no. 33, pp. 10357-10368, 2020.

[169] F. Yang, S. Li, Z. Yang, C. Qian, and T. Gu, "Spatial multiplexing for non-line of sight light-to-camera communications," *IEEE Transactions on Mobile Computing*, vol. 18, no. 11, pp. 2660-2671, Nov. 2019.

[170] J. Lain, F. Jhan, and Z. Yang, "Non-line-of-sight optical camera communication in a heterogeneous reflective background," *IEEE Photonics Journal*, vol. 11, no. 1, pp. 1-8, Feb. 2019.

[171] T. Nguyen, C. H. Hong, N. T. Le, and Y. M. Jang, “High-speed asynchronous optical camera communication using LED and rolling shutter camera,” *Seventh International Conference on Ubiquitous and Future Networks*, July 2015, pp. 214–219.

[172] C.W Chow, R. J Shiu, Y. C Liu, Y. Liu, and C. H. Yeh, "Non-flickering 100 m RGB visible light communication transmission based on a CMOS image sensor," *Optics Express*, vol. 26, no. 6, pp. 7079-7084, 2018.

[173] P. Chavez-Burbano, S. Vitek, S. R. Teli, V. Guerra, J. Rabadan, R.Perez Jimenez, and S. Zvanovec, "Optical camera communication system for internet of things based on organic light emitting diodes", *Electronics Letters*, vol. 55, no. 6, pp. 334-336, 2019.

[174] M. A. Atta, and A. Bermak, "A 160 m visible light communication link using

hybrid undersampled phase-frequency shift on-off keying and CMOS image sensor", *Optics Express*, vol. 27, no.3, pp. 2478-2487, 2019.

[175] P. Chavez-Burbano, V. Guerra, J. Rabadan, and R. Perez-Jimenez, "Optical camera communication for smart cities," *IEEE/CIC International Conference on Communications in China (ICCC Workshops)*, 2017, pp. 1-4.

[176] N. B. Hassan, Z. Ghassemlooy, S. Zvanovec, M. Biagi, A.M. Vegni, M. Zhang, and P. Luo, 'Non-line-of-sight MIMO space-time division multiplexing visible light optical camera communications', *Journal of Lightwave Technology*, vol. 37, no. 10, pp. 2409-2417, 2019.

[177] N. B. Hassan, "MIMO visible light communications with camera-based receiver for intelligent transport systems," PhD thesis, Faculty of Engineering and Environment Northumbria University, 2019.

[178] J. C. Chau, and T. D. C. Little, "Analysis of CMOS active pixel sensors as linear shift invariant receivers," *IEEE International Conference on Communication Workshop (ICCW)*, 2015, pp. 1398–1403.

[179] X. Li, N. B. Hassan, A. Burton, Z. Ghassemlooy, S. Zvanovec, and R. Perez Jimenez, "A Simplified Model for the Rolling Shutter Based Camera in Optical Camera Communications," *15th International Conference on Telecommunications (ConTEL)*, 2019, pp. 1-5.

[180] N. B. Hassan, Y. Huang, Z. Shou, Z. Ghassemlooy, A. Sturniolo, S. Zvanovec, P. Luo, and H. Le-Minh, "Impact of camera lens aperture and the light source size on optical camera communications," *11th International Symposium on Communication systems, Networks and Digital Signal Processing (CSNDSP)*, July 2018, pp. 1–5.

[181] S. Verma, "Analysing the performance and stability of LED-to-camera links," Master's thesis, Faculty of Electrical Engineering, Mathematics and Computer Science, Delft University of Technology, 2017.

[182] J. Nakamura, *Image sensors and signal processing for digital still cameras*: CRC press, 2016.

[183] Q. Huynh-Thu, and M. Ghanbari, "Scope of validity of PSNR in image/video quality assessment", *Electronics Letters*, vol. 44, no. 13, pp. 800-801, 2008.

[184] G. Yang, M.-A. Khalighi, Z. Ghassemlooy, and S. Bourennane, "Performance

evaluation of receive-diversity free-space optical communications over correlated gamma-gamma fading channels.," *Applied Optics*, vol. 52, no. 24, pp. 5903–5911, Aug. 2013.

[185] M. Abaza, R. Mesleh, A. Mansour, and E. M. Aggoune, "Spatial diversity for FSO communication systems over correlated atmospheric turbulence channels," *IEEE Wireless Communications and Networking Conference (WCNC)*, 2014, pp. 382–387.

[186] S. Navidpour, M. Uysal, and M. Kavehrad, "BER performance of free-space optical transmission with spatial diversity," *IEEE Transactions Wireless Communications*, vol. 6, no. 8, pp. 2813–2819, Aug. 2007

[187] M. Abaza, R. Mesleh, A. Mansour, and E. M. Aggoune, "Spatial diversity for FSO communication systems over atmospheric turbulence channels," *IEEE Wireless Communications and Networking Conference (WCNC)*, 2014, pp. 382-387.

[188] E. Lee, Z. Ghassemlooy, W. P. Ng, and M.-A. Khalighi, "Joint optimization of a partially coherent gaussian beam for free-space optical communication over turbulent channels with pointing errors," *Optics Letters*, vol. 38, no. 3, pp. 350-352, 2013.

[189] K. Prabu, D. Sriram Kumar, and T. Srinivas, "Performance analysis of FSO links under strong atmospheric turbulence conditions using various modulation schemes, " *Optik*, vol. 125, no. 19, pp. 5573-5581, 2014.

[190] O.O. Adedayo, O.B. Ilesanmi, O.M. Adegoke, and A. Adedayo, "Mitigating turbulence-induced fading in coherent FSO links: An adaptive space-time code approach, telecommunication systems, " *in Principles and Applications of Wireless-Optical Technologies*, London, IntechOpen, 2019. [Online]. Available: https://www.intechopen.com/books/telecommunication-systems-principles-and-applications-of-wireless-optical-technologies/mitigating-turbulence-induced-fading-in-coherent-fso-links-an-adaptive-space-time-code-approach

[191] S. P. Joseph, and M. Mathew, "A review on performance improvement techniques in wireless optical communication, " *International Journal of Science and Research*, " vol. 4, no. 8, 2015.

[192] Sonali, N. Gupta, A. Dixit, and V. K. Jain, "Performance analysis of BCH and

repetition codes in gamma-gamma faded FSO Link," *National Conference on Communications (NCC)*, 2019, pp. 1-5.

[193] Sonali, N. Gupta, A. Dixit, and V. K. Jain, "Capacity and BER analysis of BCH and LDPC coded FSO communication system for different channel conditions, " *Optical and Quantum Electronics*, vol. 53, pp. 1-25, 2021.

[194] T. Ohtsuki, "Turbo-coded atmospheric optical communication systems," *IEEE International Conference on Communications. Conference (ICC)*, 2002, pp. 2938–2942.

[195] I. B. Djordjevic, "LDPC-coded optical communication over the atmospheric turbulence channel," *Conference Record of the Forty-First Asilomar Conference on Signals, Systems and Computers*, 2007, pp. 1903-1909.

[196] M. Khalighi, N. Schwartz, N. Aitamer, and S. Bourennane, S. "Fading reduction by aperture averaging and spatial diversity in optical wireless systems," *IEEE/OSA Journal of Optical Communications and Networking*, vol. 1, no. 6, pp. 580-593, 2009.

[197] P. Kaur, V. K. Jain, and S. Kar, BER performance improvement of FSO links with aperture averaging and receiver diversity technique under various atmospheric conditions," *IEEE, 9th International Conference on Industrial and Information Systems* (ICIIS), pp. 1–6, Dec. 2014.

[198] F. S. Vetelino, C. Young, L. Andrews, and J. Recolons, 'Aperture averaging effects on the probability density of irradiance fluctuations in moderate-to-strong turbulence," *Applied Optics*, vol. 46, no. 11, pp. 2099-2108, 2007.

[199] H. Yuksel, S. Milner, and C. C. Davis, "Aperture averaging for optimizing receiver design and system performance on free-space optical communication links," *Journal of Optical Networking*, vol. 4, no. 8, p. 462-475, 2005.

[200] M. Ijaz, ''Experimental characterisation and modelling of atmospheric fog and turbulence in FSO,'' PhD thesis, Faculty of Engineering and Environment Northumbria University.

[201] V. Matus *et al*, "Experimental evaluation of an analog gain optimization algorithm in optical camera communications," *12th International Symposium on Communication Systems, Networks and Digital Signal Processing (CSNDSP)*, 2020, pp. 1-5.

[202] V. Matus, E. Eso, S. R. Teli, R. Perez-Jimenez, and S. Zvanovec,

"Experimentally derived feasibility of optical camera communications under turbulence and fog conditions," *Sensors*, vol. 20, no. 3, p. 757, Jan. 2020.

[203] V. Matus, V. Guerra, S. Zvanovec, J. Rabadan, and R. Perez-Jimenez, "Sandstorm effect on experimental optical camera communication," *Applied Optics*, vol. 60, no. 1, pp. 75-82, 2021

[204] IDS Imaging and Development Systems GmbH, *Brighter images thanks to gain-How to work with gain*, 2015. [Online]. Available: https://en.ids-imaging.com/tl_files/downloads/techtip/TechTip_Gain_EN.pdf

[205] M. Ijaz, Z. Ghassemlooy, J. Pesek, O. Fiser, H. Le Minh and E. Bentley, "Modeling of fog and smoke attenuation in free space optical communications link under controlled laboratory conditions," *Journal of Lightwave Technology*, vol. 31, no. 11, pp. 1720-1726, 2013

[206] J. Perez, Z. Ghassemlooy, S. Rajbhandari, M. Ijaz and H. L. Minh, "Ethernet FSO communications link performance study under a controlled fog environment," *IEEE Communications Letters*, vol. 16, no. 3, pp. 408-410, March 2012.

[207] In Control, *Safe driving tips, The Three Second Rule.* Feb. 2018. [Online]: Available: www.driveincontrol.org/drivingtips/the-three-second-rule

[208] European Commision, *Current speed limit policies*, Mobility and Transport. [Online]. Available: https://ec.europa.eu/transport/road_safety/specialist/knowledge/speed/speed_limits/current_speed_limit_policies_en, 2019.

[209] C. L. Joseph, E. Halkiadakis, S. Bernal, and D. Maiullo, *Modern Devices: The Simple Physics of Sophisticated Technology*: John Wiley & Sons, 2016.

[210] V. Jungnickel, A. Forck, T. Haustein, U. Kruger, V. Pohl, and C. von Helmolt, "Electronic tracking for wireless infrared communications," *IEEE transactions on wireless communications*, vol. 2, no. 5, pp. 989–999, 2003

[211] Keysight Technologies, *How Do I Measure the Bit Error Rate (BER) to a Given Confidence Level on the J-BERT M8020A and the M8040A High-Performance BERT?* [Online]. Available: https://edadocs.software.keysight.com/kkbopen/how-do-i-measure-the-bit-error-rate-ber-to-a-given-confidence-level-on-the-j-bert-m8020a-and-the-m8040a-high-performance-bert-588276182.html

[212] A. Mederos-Barrera, C. Jurado-Verdu, V. Guerra, J. Rabadan, and R. Perez-Jimenez, “Design and experimental characterization of a discovery and tracking system for optical camera communications,” *Sensors*, vol. 21, no. 9, p. 2925, Apr. 2021.

[213] L. M. Matheus, A. B. Vieira, M. A. M. Vieira, and L. F. M. Vieira, "DYRP-VLC: A dynamic routing protocol for Wireless Ad-Hoc Visible Light Communication Networks, " *Ad Hoc Networks*, vol. 94, pp. 1-13, 2019,

[214] M. Garai, M. Sliti, and N. Boudriga, "Access and resource reservation in vehicular Visible Light Communication networks," *18th International Conference on Transparent Optical Networks (ICTON)*, 2016, pp. 1-6.

[215] J. Jagannath, and T. Melodia, "VL-ROUTE: A cross-layer routing protocol for visible light ad hoc network," *IEEE 20th International Symposium on "A World of Wireless, Mobile and Multimedia Networks" (WoWMoM)*, 2019, pp. 1-9.

[216] C. Tripp-Barba, A. Zaldívar-Colado, L. Urquiza-Aguiar, and J. A. Aguilar-Calderón, “Survey on routing protocols for vehicular ad hoc networks based on multimetrics,” *Electronics*, vol. 8, no. 10, p. 1177, Oct. 2019.

[217] I. Broustis, M. Faloutsos, "Routing in vehicular networks: Feasibility, modeling, and security", *International Journal of Vehicular Technology*, vol. 2008, pp. 1-8 pages, 2008.